An Integrated System Evaluation Engine for Visible Light Communication Transceiver Design

by

Tianxin MIN

A Thesis Submitted to

The Hong Kong University of Science and Technology
in Partial Fulfillment of the Requirements for
the Degree of Master of Philosophy
in the Department of Electronic and Computer Engineering

May 2022, Hong Kong

Authorization

I hereby declare that I am the sole author of the thesis.

I authorize the Hong Kong University of Science and Technology to lend this thesis to other institutions or individuals for purpose of scholarly research.

I further authorize the Hong Kong University of Science and Technology to reproduce the thesis by photocopying or by other means, in total or in part, at the request of other institutions or individuals for the purpose of scholarly research.

Signature redacted
Tianxin MIN
May 2022

An Integrated System Evaluation Engine for Visible Light Communication Transceiver Design

by

Tianxin MIN

This is to certify that I have examined the above MPhil thesis and have found that it is complete and satisfactory in all respects, and that any and all revisions required by the thesis examination committee have been made.

Signature redacted

Prof. C. Patrick YUE, ECE Department (Thesis Supervisor)
Signature redacted

Prof. Andrew Wing On POON (Head of ECE Department)

Thesis Examination Committee

- 1. Prof. Howard LUONG (Chairperson)
 - Department of Electronic and Computer Engineering
- 2. Prof. C. Patrick YUE (Supervisor)
 - Department of Electronic and Computer Engineering
- 3. Prof. Kevin J. CHEN
 - Department of Electronic and Computer Engineering

Department of Electronic and Computer Engineering
The Hong Kong University of Science and Technology
May 2022

Dedicated to my family

Acknowledgments

Looking back to the 2-year journey spent at the Hong Kong University of Science and Technology, I have been surrounded by wonderful people who are generous to help others, diligent and rigorous about their work, and passionate about pursing big dreams. I am grateful for everything I have learned here, and for growing as a person with a broader perspective and a clearer life plan.

First and foremost, I want to express my sincere gratitude to my thesis supervisor Professor Patrick Yue. It was his insights into the world, his passion for life and work, his constant curiosity, and his thoughts on novel things that have had a profound impact on me and my research. In addition, I am very grateful to him for patiently helping me revise the article, pointing out the problems in my report and presentation, and guiding me to expand my thinking to make the whole project more complete and valuable. I still remember one day he encouraged us to select a female model in the world and aspire to be like them. This will continue to be my driving force for moving forward.

I would like to express my gratitude to Professor Howard LUONG and Professor Kevin J. CHEN for serving as my thesis examination committee members during such an unusual period.

Gratefulness also goes to my lab mates, Dr. Xianbo Li, Dr. Weimin Shi, Dr. Li, Dr. Babar HUSSAIN, Dr. Kuang Fang, Jian Kang, Xu Bo, Johar ABDEKHODA, Fuzhan Chen, Zilu Liu, Xinyi Liu, Chongyun Zhang, Yiru Wang, and others. Special thanks to Li, Xu Bo Jian Kang, and Johar ABDEKHODA for their constant guidance and suggestions when I encountered difficulties in my research. Thanks to my friend Yi Liu for all the warm discussions and generous support on the study. Besides, thanks to my friends Zilu Liu, Xu Bo, Xinyi Liu, Lin Chen, Zixi Jing, Bibi Cai for all the accompany during a 2-year life in Hong Kong. I will never forget all the generous help I received from you and all the happy time we spent together. I will cherish these memories in mind and keep going with what I have learned from you.

Finally, I want to thank my parents for their unconditional trust and support. They always tell me I can do everything I want and support every decisions I made.

Table of Contents

Title Pag	ge	1
Authoriz	zation Page	ii
Signatur	re Page	iii
Acknowl	ledgments	v
List of F	igures	viii
List of T	ables	xi
Abstract		xii
	ER 1. INTRODUCTION	
1.1	Research Background	
	· ·	
1.2	Typical VLC Implementation	4
1.3	Challenges	5
1.3.1	Device Constraints	5
1.3.2	Long and Expensive Verification	6
1.4	Thesis Organization	7
СНАРТЕ	CR 2. INTEGRATED SYSTEM EVALUATION ENGINE	8
2.1	Introduction to Integrated System Evaluation Engine	8
2.2	Motivation	10
2.2.1	Efficient Verification of System Performance	10
2.2.2	Joint Optimization for Baseband and Front-end Circuit Design	10
2.3	Prior Arts of Baseband Design in VLC	10
2.4	Baseband Modem Implemented in Matlab	12
2.4.1	Pulse Amplitude Modulation	12
2.4.2	Feed-Forward Equalizer in PAM	14
2.4.3	Pulse Amplitude Demodulation	16
2.4.4	DCO-OFDM Modulation	17
2.4.5	DCO-OFDM Demodulation	
2.4.6	DCO-OFDM Modulation with BEA	
2.4.7	Bit and Energy Allocation in DCO-OFDM Modulation	21
2.5	VLC Channel Model	25
2.5.1	Light-emitting Diode (LED) Model	25
2.5.2	Photodiode (PD) Model	26
2.5.3	Lighting Standards in Practical VLC	26

2.5.4	Line-of-sight Channel Model	26		
СНАРТЕ	CR 3. VLC RECEIVER SYSTEM-ON-CHIP DESIGN	32		
3.1	Introduction to VLC Receiver SoC	32		
3.2	Typical Receiver Architecture	33		
3.3	Proposed VLC Receiver Architecture			
3.4	Proposed Low Noise Cascode TIA			
3.4.1	Introduction to TIA			
3.4.2	Trade-offs of the Shunt TIA			
3.4.3	Proposed TIA Design			
3.4.4	Verification of the Proposed TIA			
3.4.5	Corner Variation Compensation of the Proposed TIA			
3.5	Continuous Time Linear Equalizer	46		
3.6	Other Blocks	47		
3.6.1	Ambient Light Rejection Unit	47		
3.6.2	DC Offset Cancellation Unit	49		
3.6.3	Variable Gain Amplifier	49		
3.6.4	Analog Buffer	50		
СНАРТЕ	CR 4. VLC TRANSCEIVER DESIGN AND EVALUATION	52		
4.1	VLC Transceiver with Pre- and Post- Equalization	52		
4.1.1	Pre- Equalizer at the Transmitter	53		
4.1.2	Post- Equalizer at the Receiver	54		
4.1.3	Simulation Results of the Equalizers	54		
4.2	System Simulation Results	56		
4.3	System Evaluation Results with ISEE	58		
4.4	VLC Transceiver Performance Comparison	61		
СНАРТЕ	CR 5. CONCLUSION AND FUTURE WORK	62		
5.1	Conclusion	62		
5.2	Future Work			
5.3	List of Publications			
$\mathbf{K}\mathbf{H},\mathbf{H}'\mathbf{H}',\mathbf{K}'\mathbf{H}'$	NCES	64		

List of Figures

Fig. 1 Visible light spectrum ranging from 380 nm to 780 nm.	1
Fig. 2 Visible light communication use-cases [1]	2
Fig. 3 VLC application: VLC as downlink and wireline as uplink in hybrid m	odel for
communication [3].	3
Fig. 4 LED lighting: projected size of the global markets: 2020–2026 [4]	4
Fig. 5 A typical VLC transceiver system.	5
Fig. 6 Block diagram of the Integrated System Elevation Engine	9
Fig. 7 Screenshot of co-simulation interface in Cadence.	9
Fig. 8 Screenshot of co-simulation interface in ADS.	9
Fig. 9 Modulated waveform using NRZ (1 bit per UI), and PAM-4 (2 bits per U	JI)12
Fig. 10 Block diagram for modulation and demodulation of PAM wi	th FFE
implemented in ISEE.	14
Fig. 11 Schematic of feed-forward equalizer and effects of FFE	15
Fig. 12 Calculation of tap numbers and coefficients of FFE.	15
Fig. 13 Modulated waveform using NRZ with FFE	16
Fig. 14 Signal constellation of PAM-M [32].	16
Fig. 15 Block diagram for modulation and demodulation of DCO-OFDM wi	th BEA
implemented in ISEE.	18
Fig. 16 OFDM data package in the time and frequency domain	19
Fig. 17 Modulation of DCO-OFDM on the transmitter baseband	20
Fig. 18 Demodulation of DCO-OFDM on the receiver baseband	20
Fig. 19 Graphical user interface of VLC system employing DCO-OFDM wi	th BEA
[12]	21
Fig. 20 Equivalent channels and constellation of the subcarrier QAM signal	23
Fig. 21 Equivalent LED model.	25
Fig. 22 Equivalent PD model.	26
Fig. 23 VLC channel link	27
Fig. 24 Frequency response of the equivalent LED model [11]	28
Fig. 25 Frequency response of the PD model used.	28

Fig. 26 Normalized spectrum distribution $S_t(\lambda)$ of equivalent LED model2	9
Fig. 27 Spectral luminous efficiency of typical LED model	9
Fig. 28 Responsivity of the PD model used from wavelength of 380 nm to 780 nm3	0
Fig. 29 Model for reflection coefficient calculation [31]	1
Fig. 30 Received photocurrent versus distance at the receiver side	1
Fig. 31 Architecture of the typical single-ended receiver SoC [10]	4
Fig. 32 Architecture of the typical fully-differential receiver SoC [36]3	4
Fig. 33 Proposed VLC receiver architecture	5
Fig. 34 Simplified front-end of the VLC receiver	7
Fig. 35 Schematic of the proposed TIA	9
Fig. 36 Layout of the proposed TIA.	9
Fig. 37 Equivalent small-signal model of the proposed TIA3	9
Fig. 38 Small-signal analysis of the cross-coupled pairs	0
Fig. 39 Small-signal analysis of the scaled dummy side of the proposed TIA4	1
Fig. 40 Bandwidth and noise comparison of the cascode TIA, the proposed TIA with	a
scaled dummy side. and the proposed TIA with a replica dummy side4	3
Fig. 41 Comparison of the pre- simulation and post- simulation on noise performance	Э.
4	3
Fig. 42 RC-extracted post-layout simulation at the proposed TIA output with noise or	1.
4	4
Fig. 43 Simulated negative impedance for corner variation compensation4	5
Fig. 44 Simulated bandwidth over corners of the fully-differential cascode TIA and the	e
proposed TIA4	5
Fig. 45 Schematic of continuous time linear equalizer4	6
Fig. 46 AC response of the CTLE with adjustable peaking4	7
Fig. 47 Schematic of the amplifier in ambient light rejection unit4	8
Fig. 48 Schematic of the amplifier in DC offset cancellation4	9
Fig. 49 Schematic of the variable gain amplifier5	0
Fig. 50 AC response of the variable gain amplifier5	0
Fig. 51 Schematic of the analog buffer5	1
Fig. 52 Transient PAM-4 eye simulation of the analog buffer5	1

Fig. 53 Diagram of the VLC transceiver design and evaluation through ISEE52
Fig. 54 Schematic of pre- passive LC equalizer53
Fig. 55 AC simulation result after compensation from the passive equalizer53
Fig. 56 AC response of the overall transceiver54
Fig. 57 Simulated eye diagram of the VLC transceiver with/without CTLE at 3 Gb/s
data rate & 1.5 m distance
Fig. 58 Simulated NRZ & PAM-4 eye diagram of the VLC transceiver with FFE at a
distance of 1.5 m
Fig. 59 AC simulation results of the whole transceiver56
Fig. 60 IRN current power spectral density of the VLC receiver57
Fig. 61 Simulated eye diagram of the VLC transceiver with/without ambient light at 3
Gb/s data rate & 1.5 m distance.
Fig. 62 Simulated eye diagram of the VLC transceiver with/without R _s added in ALR
at 3 Gb/s data rate & 1.5 m distance.
Fig. 63 VLC receiver power breakdown58
Fig. 64 SNR versus distance fitting curve of line-of-sight channel model59
Fig. 65 Simulated maximum data rate versus communication distances with a lens used
before the photodiode
Fig. 66 Simulated BER versus data rate at a fixed distance of 1.5 meters with a lens
used before the photodiode 60

List of Tables

Table 1.1. Comparison of VLC and RF technology [2]	3
Table 1.2. Comparison of light sources in optical communication	5
Table 1.3. Comparison of photo diodes in optical communication	6
Table 2.1. Review of VLC system performance with different baseband designs	11
Table 2.2. Calculation parameters of the proposed VLC link model	27
Table 3.1. Comparison of VLC SoC receivers with different photodiodes	33
Table 3.2. Comparison of the fully-differential and single-ended VLC receiver	34
Table 3.3. Comparison of the proposed TIA with state-of-the-art TIAs	44
Table 4.1. VLC transceiver performance comparison.	61

An Integrated System Evaluation Engine for Visible Light Communication Transceiver Design

by
Tianxin MIN
Department of Electronic and Computer Engineering
The Hong Kong University of Science and Technology

Abstract

With the evolution of computing, consumer electronics, and mobile communication, end-user data requirements have been increasing exponentially in recent years. Visible light communication (VLC) employing light-emitting diodes (LEDs) for simultaneous illumination and data transmission can utilize license-free operation over hundreds of THz to deal with radio spectrum congestion problems. This thesis focuses on the VLC transceiver design with equalizations to compensate for the limited modulation bandwidth of optoelectronic devices, and discusses the modulation schemes for maximum bit efficiency.

In the first part, a cross-domain integrated system evaluation engine (ISEE) based on Matlab, ADS, and Cadence is introduced. The baseband modulation schemes including non-return-to-zero (NRZ), 4-level pulse amplitude modulation (PAM-4), and direct-current offset OFDM (DCO-OFDM), and the performance measures including data rate, bit error rate, and transmission distance are designed in Matlab. The ISEE evaluates the transceiver circuits designed in ADS or Cadence, and compares the system performance of different modulation schemes under different signal-to-noise ratio and bandwidth constraints.

In the second part, an asymmetric differential cascode trans-impedance amplifier (TIA) employs a PMOS negative capacitor and NMOS negative gm for achieving a 2.8x bandwidth improvement. Using a photodiode with 1.8 pF parasitic capacitance, the proposed TIA achieves a trans-impedance gain of 75 dB Ω and a -3dB bandwidth of 2.3 GHz. It also attains a 0.21 uA_{rms} input-referred noise (IRN) current, which is 0.04 uA_{rms} lower than that of the symmetrical

design. A VLC transceiver based on the TIA is further verified using the ISEE to evaluate the performance of different signaling and modulation schemes including NRZ, PAM-4, and DCO-OFDM. The results show that PAM4 with feed-forward equalization (FFE) achieves the highest data rate at 5 Gb/s over a 1.5 m distance. In addition, the 1.67x bit efficiency improvement brought by the proposed design is verified at a distance of 1.5 m.

CHAPTER 1. INTRODUCTION

1.1 Research Background

With the rapid increase in data traffic in recent years due to various multimedia consumer applications, the popular radio spectrum occupying the lowest 300 GHz frequency band is facing a severe congestion problem. Shown in Fig. 1, optical communication utilizing the unregulated optical spectrum beyond 300 GHz has become a supplementary solution for more extensive and higher-speed data transmission in the future. Visible light communication (VLC), a subset of optical wireless communications, uses LEDs as a transmitter for simultaneous illumination and communication and receives the optical signal using a photodiode (PD). The ubiquitous deployment of LEDs means that VLC is attracting great interest in many scenarios, as shown in Fig. 2. VLC can also be integrated with sensors and mobile computing capabilities to enable various indoor and outdoor applications like smart home control, smart display, sensing, indoor positioning, vehicle communication, and underwater communication.

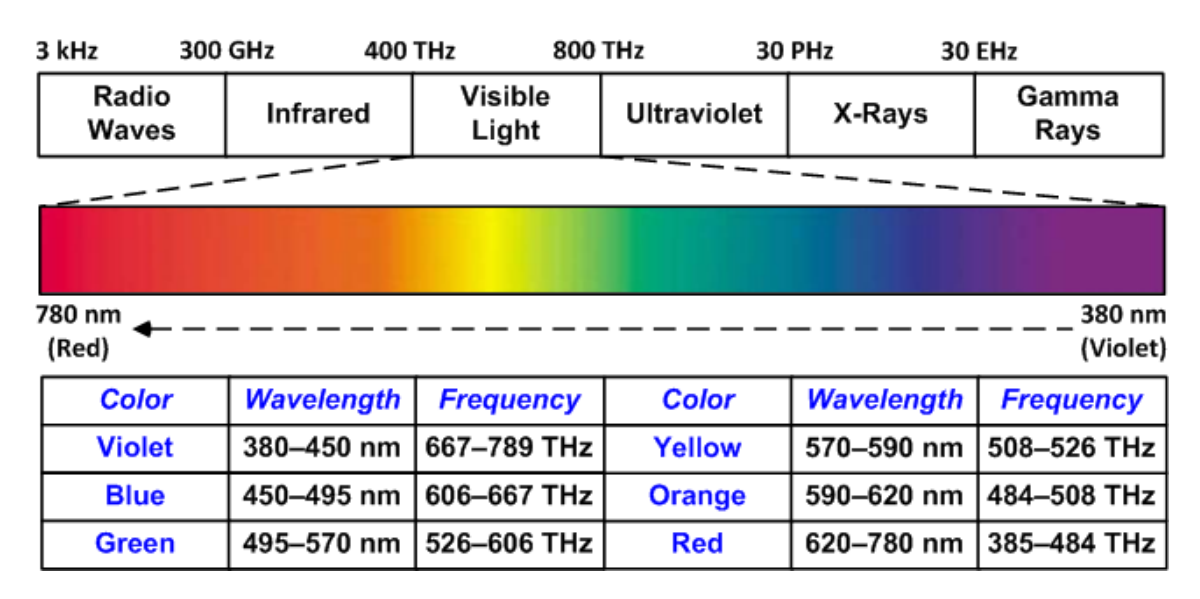


Fig. 1 Visible light spectrum ranging from 380 nm to 780 nm.

HEALTHCARE VLC

AUGMENTED EXPERIENCE VLC





OFFICE VLC

ONBOARD VLC

TRAFFIC DATA VLC







Fig. 2 Visible light communication use-cases [1].

Compared to conventional RF communications, VLC has many advantages, as summarized in Fig. 2: (1) Compared to the regulated RF spectrum, the visible light spectrum is unlicensed, making it attractive for low-cost applications. (2) On the electromagnetic spectrum, covering radio waves through to gamma rays, the available visible light spectrum is 1000 times wider (about 400 THz) than the RF spectrum, as shown in Table 1.1, and thus can provide a much higher capacity for high-speed and short-range wireless communication. (3) Since visible light cannot penetrate a wall, it has the advantage of providing enhanced security in a welldefined space because it can avoid being intercepted. (4) VLC has few electromagnetic interferences to existing RF communication systems and other sensitive systems, because VLC provides a local area network (LAN) in a small area where the light can reach, and the interference of EMI can be reduced a lot if the LEDs are placed well. Therefore, VLC is suitable to be deployed in places where radio wireless is not feasible, such as hospitals and airplanes, and enabling hybrid systems that employ VLC and RF together to take advantage of the merits of each technology [5–8]. For example, as shown in Fig. 3, VLC can supplement conventional radio frequency (RF) systems to achieve higher throughput and a larger coverage area, while RF can provide the uplink transmission capability for VLC systems to implement two-way communication. (5) Most importantly, VLC can be implemented using existing illumination infrastructure, making it possible to implement with a relatively low cost. (6) It can be predicted that visible light communication has huge market from the projected size of the global markets shown in Fig. 4. Therefore, the VLC employing LEDs as a transmitter source has a huge potential for wide deployment.

Table 1.1. Comparison of VLC and RF technology [2].

Property	VLC	RF
Bandwidth	Unlimited	Regulated and limited
Electromagnetic Interference	No	Yes
Hazard	No	Yes
Line of Sight	Yes	NO
Security	Good	Poor
Standards	IEEE802.15.7 in progress	IEEE802.11p Matured
Services	Illumination/Communication	Communication
Noise sources	Sun light/ambient lights	All electrical electronic
Power consumption	Low	Medium
Mobility	Limited	Good
FOV	Limited	Omni-directional
Communication range	Short	Short to long

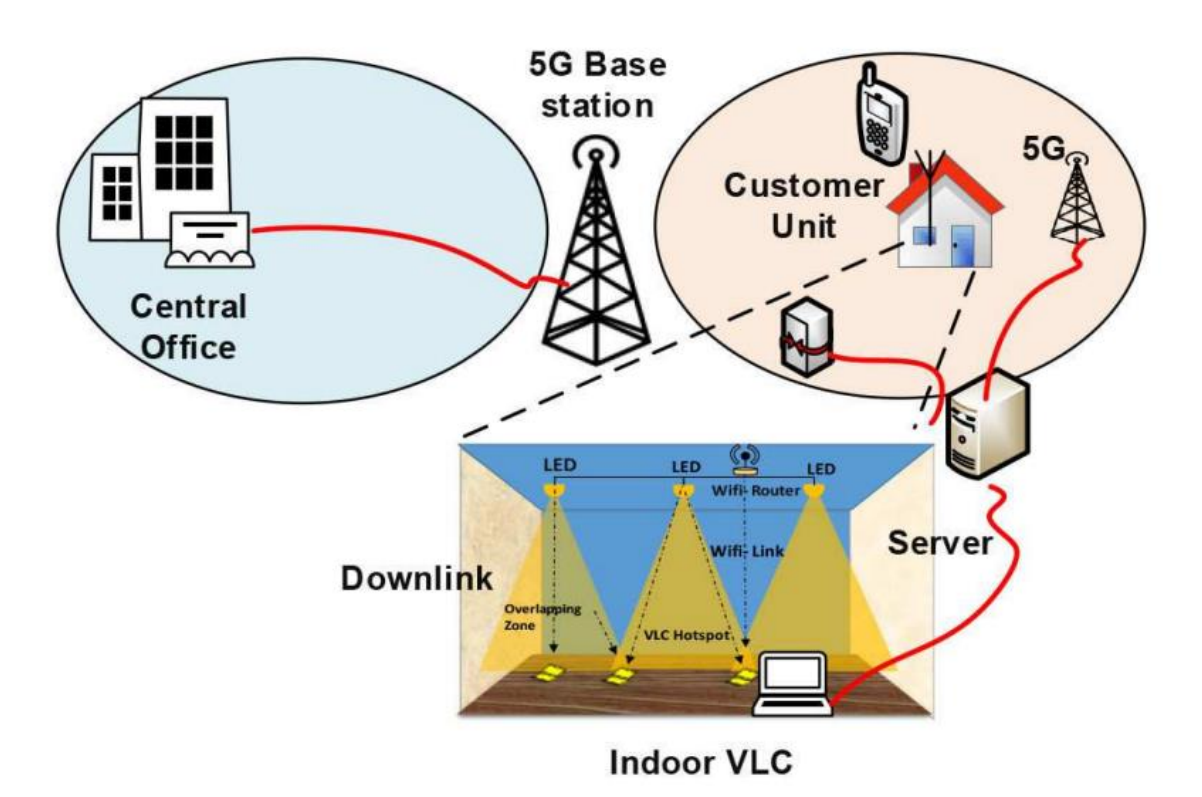


Fig. 3 VLC application: VLC as downlink and wireline as uplink in hybrid model for communication [3].

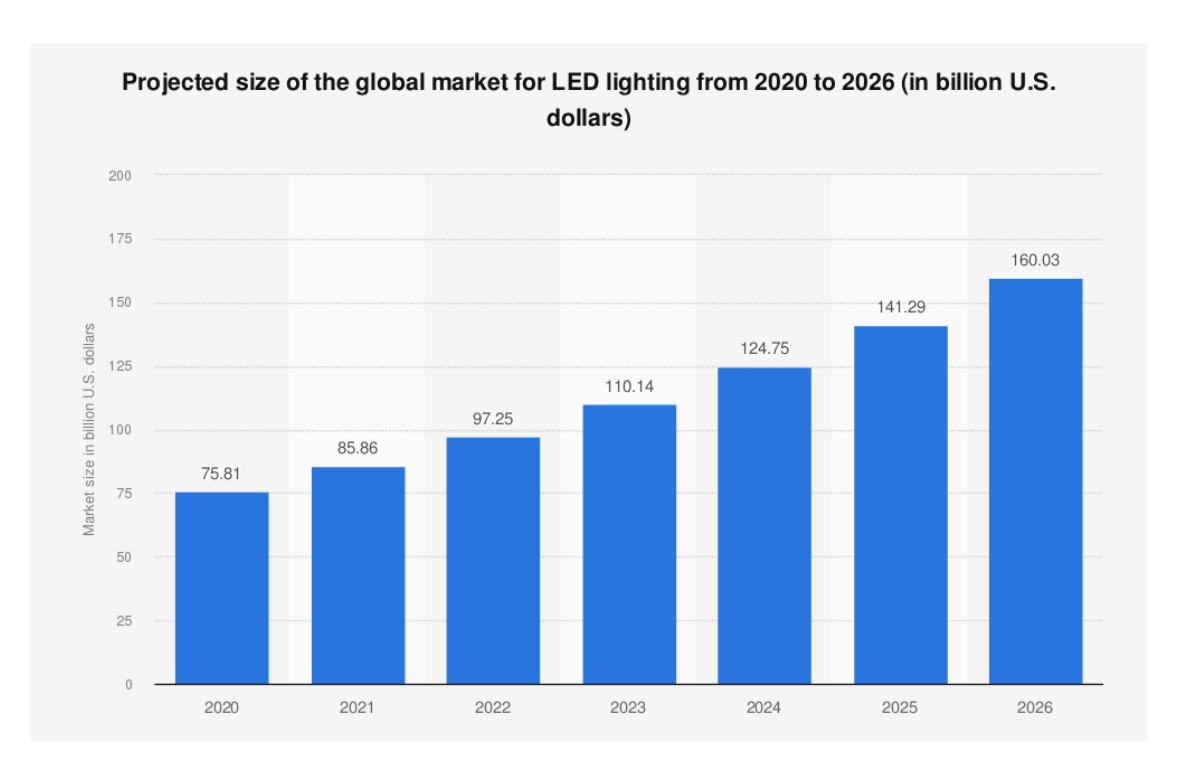


Fig. 4 LED lighting: projected size of the global markets: 2020–2026 [4].

1.2 Typical VLC Implementation

A typical VLC transceiver system implementation is shown in Fig. 5. The data source is encoded and modulated in the baseband design, and the modulated digital signal will be converted to an analog signal and amplified by the driver to drive modulate the LED, with DC separately biased for illumination. At the same time, the LED finishes the signal transformation from the electrical domain to the optical domain. The emitted light goes through the free space optical wireless channel and is then received by the PD. Usually, ambient light rejection is needed at the very front to ensure a good common mode for recovering the signal. The received small photo current signal will be amplified by a trans-impedance amplifier (TIA), and then be converted to a digital signal through an analog-to-digital converter (ADC). Finally, the signal can be demodulated and recovered in the baseband. Thus, the baseband design and front-end design are equally important for achieving better communication system performance.

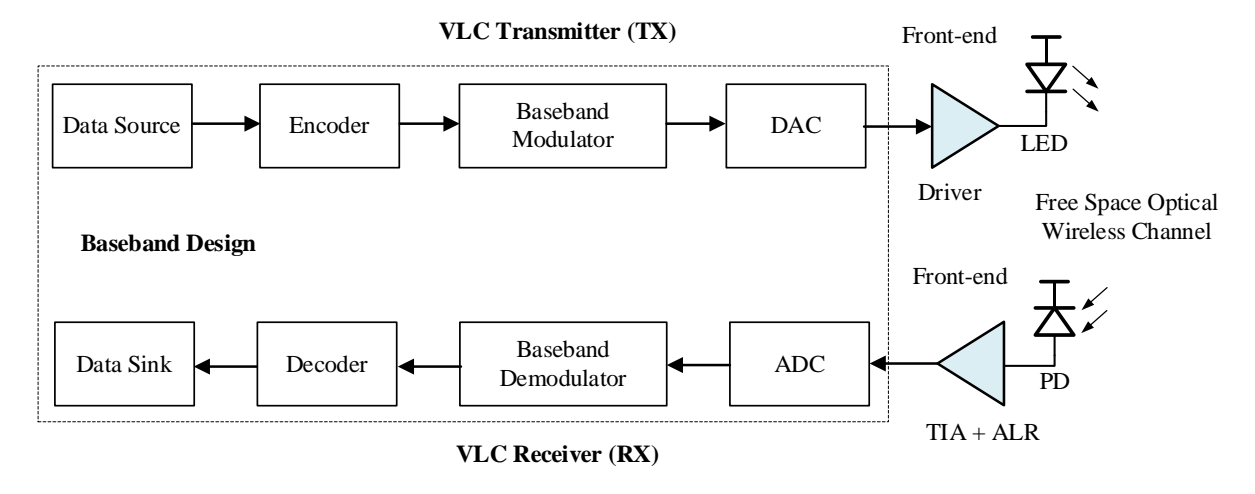


Fig. 5 A typical VLC transceiver system.

1.3 Challenges

Directivity

Communication Distance

1.3.1 Device Constraints

1.3.1.1 LED Bandwidth

The light source is essential to a VLC system since characteristics like directivity, modulation bandwidth and emitting power determine its achievable data rate and distance. The commonly used light sources in optical communication are compared in Table 1.2. Compared to high speed optical communication, the speed of VLC is extensively limited by the few MHz modulation bandwidth of the lighting source. The directivity and communication distance are limited by the high attenuation of the free-space optical wireless channel.

 Lighting Source
 Commercial LED
 μLED
 Laser Diode

 Cost
 Low
 Medium
 High

 Modulation Bandwidth
 Low
 Medium
 High

(<5 MHz)

Low

Short

Table 1.2. Comparison of light sources in optical communication.

(tens of MHz)

Low

Short

(tens of GHz)

High

Long

1.3.1.2 Sensitivity and Bandwidth Trade-off of PD

Photodiodes (PDs) are another significant optoelectronic device in optical communication for receiving light since the communication distance is decided by both photo-

sensitivity and sensing area. The commonly used photodiodes in optical communications are compared in Table 1.3. Compared to the high speed optical communication, a large light-sensing area is needed in VLC for high sensitivity due to the scattered light characteristics of LEDs. However, large parasitic capacitance is induced correspondingly and thus limit the modulation bandwidth. Therefore, the trade-off between sensitivity and bandwidth is a challenge for high system performance, especially for the VLC applications using large PDs. Considering the VLC in real environment with background light interference and acceptable communication distance, PD based VLC receiver is used for the thesis to support Gb/s data rate and distance of few meters.

Table 1.3. Comparison of photo diodes in optical communication

	Single-photon Avalanche Photodiode	Avalanche Photodiode	PIN Photodiode
Photosensitive Area	Large	Medium	Low
Terminal Capacitance	Large	Medium	Low
Photosensitivity	High	Medium	Low
Range	Tens-to-hundreds of meters	Hundreds of meters	Tens of meters
Modulation Bandwidth	Small	Medium	Medium
Illumination Peak Power	Tens of Watt	Tens of Watt	Tens of mW
Background light suppression	Low	Medium	High

1.3.2 Long and Expensive Verification

Advanced modulation schemes and other equalization techniques have been investigated to solve the bandwidth problem of optoelectronic devices. However, the verification of experiments after hardware implementation take a long time. In particular, a system-on-chip design for efficient area and low average cost requires an even longer verification period and thousands of dollars to tape out for trial. Thus, a cross-domain simulation platform for system performance evaluation is another requirement for VLC development.

1.4 Thesis Organization

The thesis is composed of four chapters.

Chapter 1 gives an introduction to visible light communication, including the research background, advantages, and challenges like device constraints and long and costly evaluation and verification of system performance. The motivation behind this thesis is also illustrated.

Chapter 2 introduces the motivation and implementation of a cross-domain simulation platform developed for VLC system evaluation, named the integrated system evaluation engine (ISEE). In addition, the prior-arts modulation schemes in baseband design are reviewed, and system performance with the different modulation schemes are compared. Then, the chapter presents the principle and analysis of pulse amplitude modulation (PAM) with feed-forward equalization (FFE), and direct-current offset orthogonal frequency division multiplexing (DCO-OFDM) with bit and energy allocation (BEA) implemented in the ISEE.

Chapter 3 proposes a low-noise cascode TIA employing a PMOS negative capacitor and NMOS negative g_m for bandwidth extension. The analysis, simulation results, comparison with state-of-the-art TIAs are illustrated. In addition, the design considerations and circuit implementation of a VLC receiver system-on-chip (SoC) design with ambient light rejection and a post-equalizer based on the proposed TIA are presented. The front-end receiver design supports both the NRZ & PAM-4 modulation schemes.

Chapter 4 presents a VLC transceiver employing the proposed receiver SoC design. The whole transceiver with pre- and post- equalization is simulated and evaluated through the ISEE. The results of different signaling and modulation schemes including non-return-to-zero (NRZ), 4-level pulse amplitude modulation (PAM-4), and DCO-OFDM are summarized and compared at the end of the chapter.

Chapter 5 draws conclusions and points out directions for future research.

CHAPTER 2. INTEGRATED SYSTEM EVALUATION ENGINE

2.1 Introduction to Integrated System Evaluation Engine

Visible light communication (VLC) employing standard white light-emitting diodes (LEDs) is has emerged as a promising alternative to address the ever-increasing radio frequency (RF) spectrum congestion problem. State-of-the-art VLC transceiver systems-on-chip (SoCs) employing simple on-off keying (OOK) modulation are limited to data rates below 25 Mbps [9],[10] due to the limited analog bandwidth of the transmitting white LEDs. Optimizing the LED die layout and DC biasing current density can greatly boost their -3-dB modulation bandwidth to reach over 70 MHz [11]. However, to accurately predict the system performance and perform circuit-level design tradeoff of such VLC systems poses a daunting design challenge as simulators in different domains are needed to cover photonic device modelling to transistor-level evaluation of the circuit under complex baseband signal excitation.

An integrated circuit evaluation engine (ISEE) [12],[13] is developed to address this problem. The ISEE is proposed not only for VLC, but also for millimeter wave communication [14] and optical communication [15]. The block diagram of the ISEE for VLC is shown in Fig. 6, while screenshots of the co-simulation interface in Cadence and ADS are shown in Fig. 7 and Fig. 8 respectively.

The modulated signal is generated in Matlab and then converted to go through a measurement data-based LED driver model in Cadence. The LEDs convert the driving current into an emitted optical signal, which then goes through a semi-empirical equation-based line-of-sight (LOS) channel model [16] implemented in Cadence. The complete LED-channel-photodiode model converts the detected optical power into the current, and accounts for the frequency response of the LEDs, the non-linear relationship between the forward bias current and the luminous flux, the spectral luminous efficiency, the normalized spectrum distribution, and responsivity of the photodiode. The relationship between the signal-to noise ratio (SNR) at the front of the receiver and transmission power and distance can be obtained with the channel model.

Pulse amplitude modulation (PAM) with feed forward equalization (FFE) for bandwidth compensation and direct-current offset orthogonal frequency division multiplexing (DCO-OFDM) with bit-and-energy allocation (BEA) for maximum bit efficiency are implemented in the designed engine. The data rate and bit error rate (BER) can be attained through demodulation for transceiver system comparison with these modulation schemes.

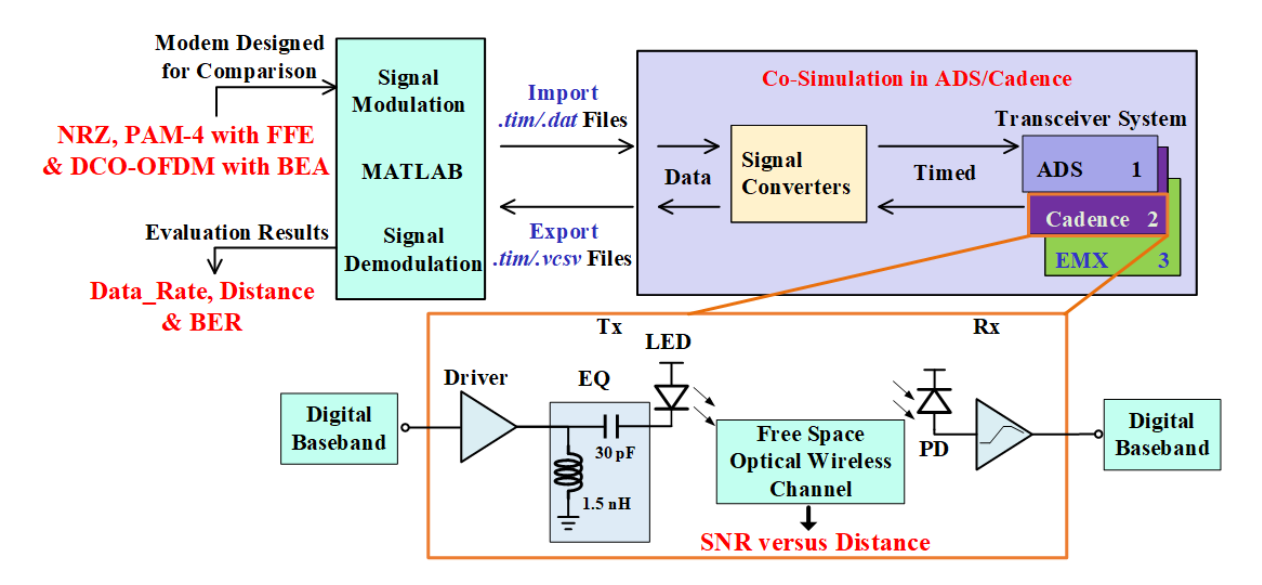


Fig. 6 Block diagram of the Integrated System Elevation Engine.

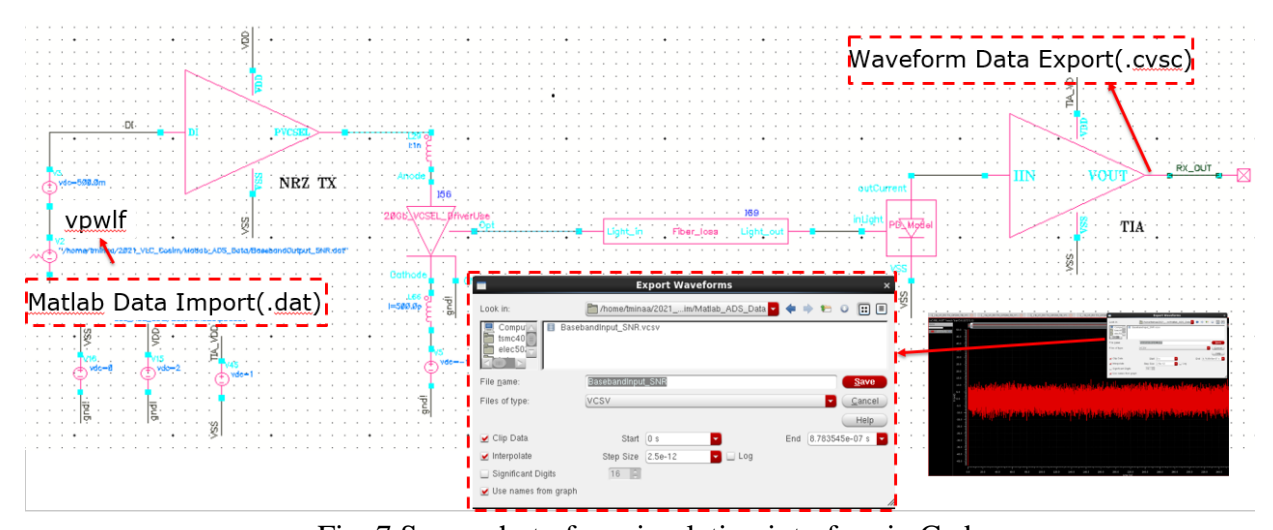


Fig. 7 Screenshot of co-simulation interface in Cadence.

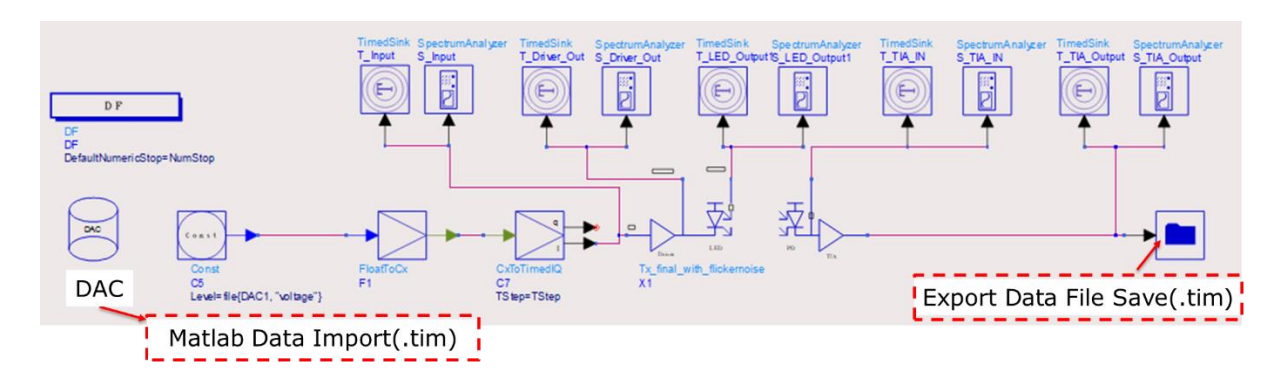


Fig. 8 Screenshot of co-simulation interface in ADS.

2.2 Motivation

2.2.1 Efficient Verification of System Performance

As illustrated in Chapter 1.3, verification of a VLC system adopting advanced modulation schemes for bit efficiency takes a long time and thousands of dollars. The cross-domain ISEE simulation platform introduced in this chapter targets efficient evaluation of such novel systems. With the platform, designers can attain the data rate and BER as well as communication distance through baseband design in Matlab and front end design and model ubcin Cadence or ADS, and it can serve as a benchmark to help IC designers verify their design with complex baseband modulation techniques before long-cycle and costly manufacturing. Thus, the open-source ISEE can save effort for researchers in VLC.

2.2.2 Joint Optimization for Baseband and Front-end Circuit Design

Implementations of pre- and post- equalizers in the baseband and front end require joint optimization of system performance. Since the baseband and front end designs are integrated in the ISEE, such joint optimization can be realized. Meanwhile, the contribution of a single part can also be attained using the ISEE.

2.3 Prior Arts of Baseband Design in VLC

In a VLC system, as pointed out above, the limited bandwidth of LEDs obstructs the advancement of high-speed VLC applications. To overcome this problem, various approaches have been proposed, including pre- and post- equalization techniques to compensate for the frequency response of the LEDs [22]-[25]. Moreover, different modulation techniques at the baseband have recently been proposed to tradeoff between factors including complexity, spectral and power efficiency, and robustness towards interference.

The modulation schemes for intensity modulation/direct detection (IM/DD) in VLC can be divided into subcarrier and non-subcarrier modulation which uses characteristics like amplitude, phase for modulation, and subcarrier modulation [17]. The popular non-subcarrier modulations include on-off keying (OOK), pulse-amplitude modulation (PAM), and pulse-position modulation (PPM), while the popular subcarrier modulations include carrier-less amplitude and phase modulation (CAP) and orthogonal frequency division multiplexing (OFDM). For IM/DD, OFDM has many variants, like asymmetrically clipped optical OFDM (ACO-OFDM) which gives up half of the spectrum but has higher spectral efficiency and DC-

biased optical OFDM, which has been shown to outperform other OFDM schemes in bit efficiency considering a practical system with a limited dynamic range [18].

Table 2.1. Review of VLC system performance with different baseband designs.

Reference	Modulation Scheme	Data Rate (Gb/s)	BW Extension	Distance (m)	LED Type	LED Bandwidth (MHz)	PD Type
[19]	OOK	0.614	EQ	0.45	Red LED	6.8	PD
[20]	ООК	4	No	0.2	Blue LD	2600	PD
[21]	PAM-4	1.1	EQ	0.46	P-LED	0.02	PD
[22]	PAM-4	2	EQ	0.6	μLED	0.15	PD
[23]	PAM-8	1.5	EQ+DNN	1.2	Blue LED	-	PD
[24]	DCO- OFDM	2	EQ	1.5	P-LED	28	PD
[25]	DCO- OFDM	5	-	1	μLED	800	PD
[26]	OFDM	3	EQ+BEA	0.05	μLED	60	APD

Among the modulation schemes, NRZ, PAM-4, and DCO-OFDM have been widely discussed and verified in high-speed optical communication systems to boost bandwidth efficiency. Thus, PAM and DCO-OFDM have been implemented in the designed engine. Related works using different lighting sources are reviewed in Table 2.1. Other newly developed modulation schemes like neural network-based equalization are not considered in the thesis, but the engine can be extended to such schemes with an additional section for transient signal processing for verification.

In conclusion, it has been verified that a VLC system can reach Gb/s data rates and a 0.5~3m distance employing advanced techniques for bandwidth compensation. However, the performance varies with the optoelectronic devices. For fair comparison of VLC systems, the significant parameters of the devices should be considered.

2.4 Baseband Modem Implemented in Matlab

PAM with FFE for bandwidth compensation and DCO-OFDM for maximum bit efficiency are integrated in the designed engine. The principle and demodulation analysis of these modulation schemes are presented in the following sections.

2.4.1 Pulse Amplitude Modulation

PAM is a one-dimensional multilevel modulation scheme with low implementation complexity. The improved spectral efficiency of PAM is achieved by transmitting more than one bit of data during each symbol period.

PAM-2 (also called NRZ) and PAM-4 are commonly used in VLC. The PAM-4 scheme utilizes four levels for signal transmission and each symbol period can represent two bits of logic information. Compared to NRZ, PAM-4 has almost twice the data rate and higher bandwidth efficiency, while PAM-8 will have three times the data rate. However, the high-order modulations are only supported with a larger SNR. In addition, higher-order modulations also induce increased inter-symbol interference (ISI), so they are more sensitive to tap numbers and weights of the FFE.

Fig. 9 shows the difference in the modulated waveforms using PAM-4 and PAM-2 (NRZ) for the same bit rate.

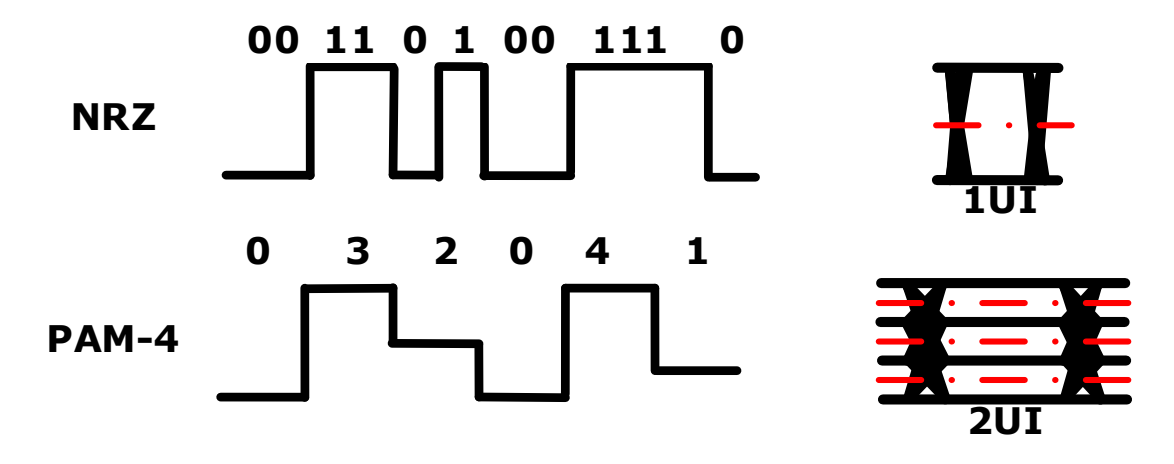


Fig. 9 Modulated waveform using NRZ (1 bit per UI), and PAM-4 (2 bits per UI).

The block diagram of PAM with FFE modulation and demodulation implemented in the ISEE is shown in Fig. 10. The original pseudo-random binary sequence (PRBS) signal is modulated as PAM-2, PAM-4, and PAM-8 with or without superposition. After that, the FFE can be added or bypassed through full zero settings for tap number, tap weights and tap space.

The FFE is realized through the addition of the original data and the delayed data with the scaling factor of the tap weights. The tap space decides whether the FFE will be integer or fractional type. Normally, a larger tap weight will provide more BW compensation, whereas the de-emphasis characteristic of FFE will decrease the transmitted signal output.

After the FFE, the modulated signal will be up-sampled and the transient signal will be generated for baseband output with another time dimension added according to the symbol rate setting. The output will be the excitation for an analog transceiver designed in Cadence or ADS. The simple models used are presented in Chapter 2.5, and mainly include the bandwidth limitation of the optoelectronic devices. After data are exported from the transient simulation of the transceiver, the function of additive white Gaussian noise (AWGN) in Matlab will be used for determining the SNR with white noise. Then the data will be synchronized by taking the signal starts one by one and demodulating them to find the minimum bit error rate. The demodulated PRBS can be attained with the M-1 threshold settings from the transient eye diagram after down-sampling. The BER is calculated by comparison of each bit, as shown in Eq. 2.1:

bit error rate =
$$\frac{\text{Number of bits received in error}}{\text{Number of bits received in total}}$$
. (2.1)

In the code implementation, the original PRBS sequence is used for 2-path data generation. The second data path uses the 2-bit delayed PRBS, and the two paths are added together to generate the output with multiplication factors of 1 and 2 respectively. Other PAM-M can be generated with the same methods, where each symbol will have $N = log_2M$ bits for transmission.

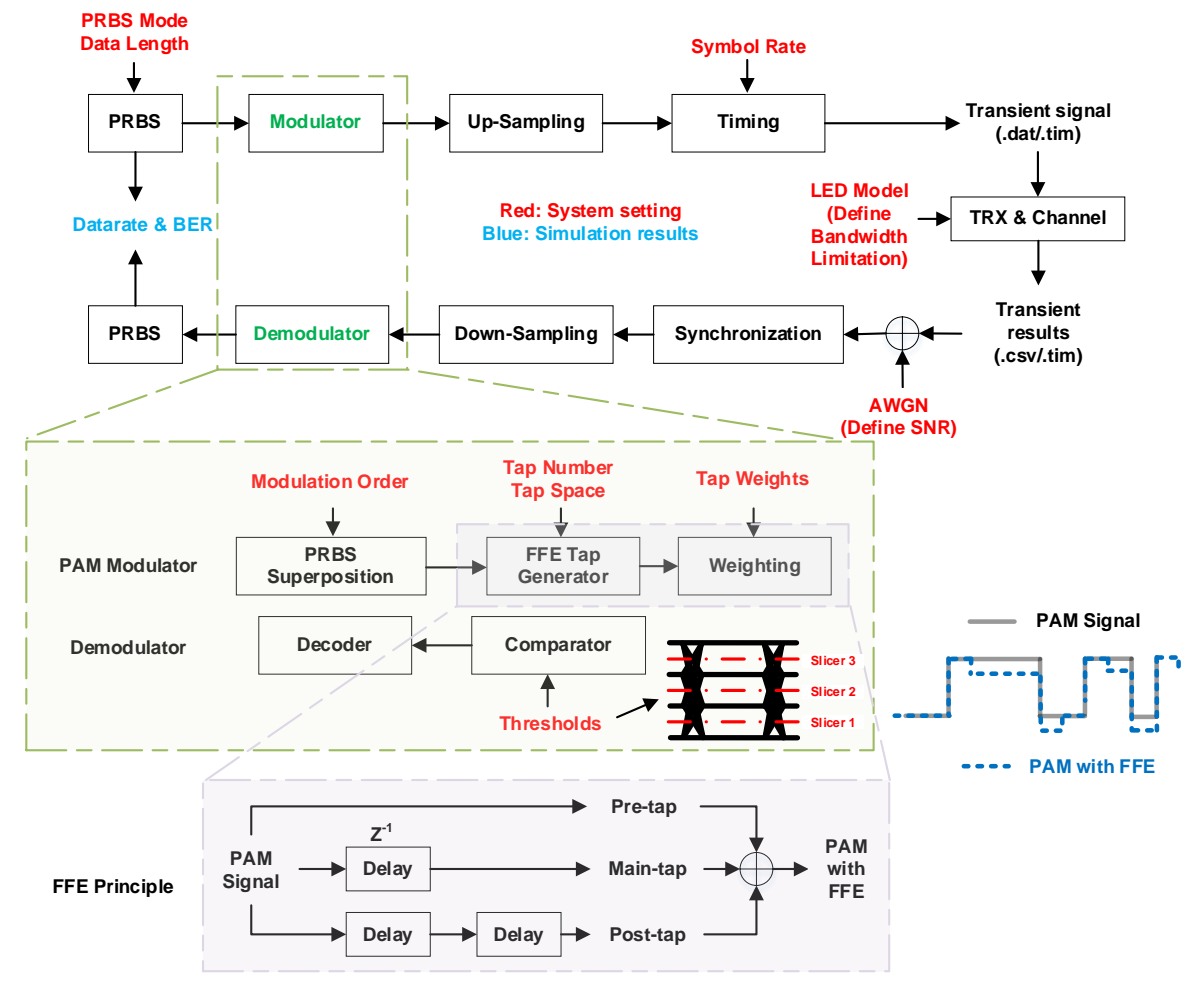


Fig. 10 Block diagram for modulation and demodulation of PAM with FFE implemented in ISEE.

2.4.2 Feed-Forward Equalizer in PAM

The pre-equalization method of FFE used in a PAM-M modulation scheme at the transmitter is proposed in order to achieve a high bit efficiency with a limited bandwidth. It has already been widely applied for high-speed optical links to reduce ISI and increase the transmission data rate [27]. Small overheads with a small number of equalizer taps and simple circuits can achieve great performance improvements.

The implementation of the FFE in Matlab is shown in the Fig. 11. After an uncompensated channel, the signal will have a long tail due to the ISI, as shown by the green line on the left side of the figure. The FFE uses the delayed and re-weighted signal in addition to deducting the tail signal so as to get the pulse shown by the red line on the right side of Fig. 11. If the transmitted PAM-M pulse signal is x[n], then the signal after FFE is y[n], as displayed in Eq. 2.2:

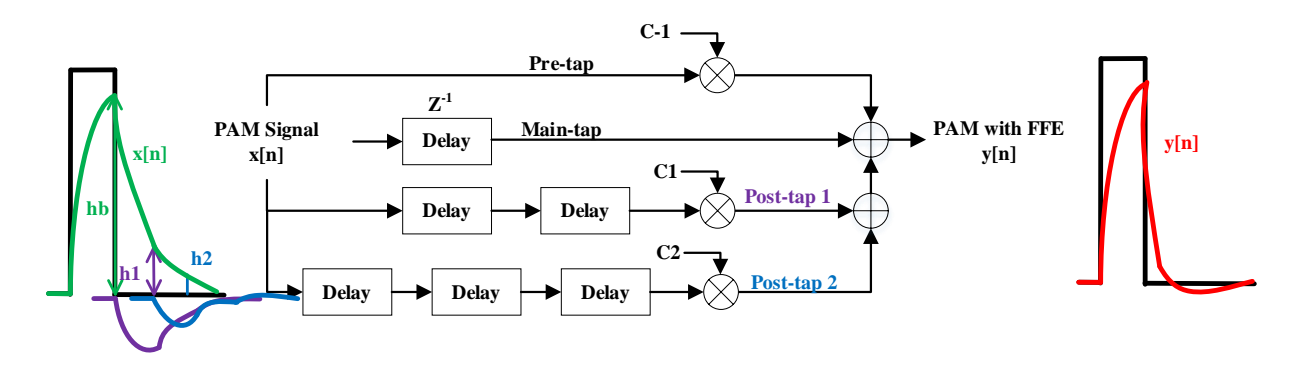


Fig. 11 Schematic of feed-forward equalizer and effects of FFE.

$$y[n] = \sum_{k=-N}^{M} c_k x[n-kT]$$
 (2.2)

(pre_tap number: N; post tap number: M; ck:coefficient)

$$H(Z) = \sum_{k=-N}^{M} c_k Z^{-k}$$
 (2.3)

(pre_tap number: N; post tap number: M; c_k:coefficient)

where H(Z) represents the transfer function of the FFE, C_k stands for the tap coefficients, k stands for the unit tap numbers delayed compared to the main-tap, and T stands for the time width of the pulse.

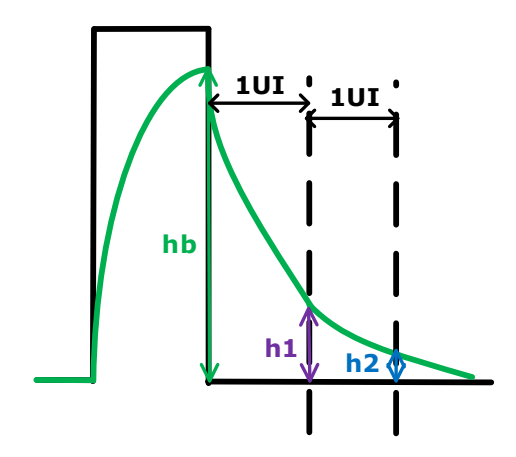


Fig. 12 Calculation of tap numbers and coefficients of FFE.

To get the right compensation with FFE, the transient pulse signal should be tested through the uncompensated channel. After the output signal with a long tail shown in Fig. 12, the calculation of tap numbers and coefficients of FFE can be attained through Eq. 2.3:

$$c_{-1} = 0; c_1 = \frac{h_1}{h_b}; c_2 = \frac{h_2}{h_b}.$$
 (2.4)

The modulated PAM-2 signal with FFE implementation can be seen in Fig. 13. Intuitively, a sharp transition signal with high-frequency characteristics is obtained after FFE.

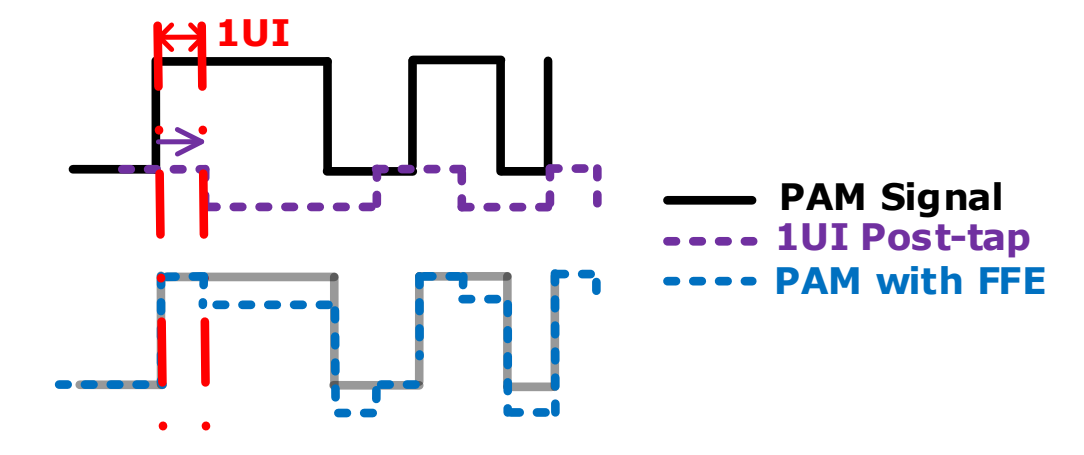


Fig. 13 Modulated waveform using NRZ with FFE

2.4.3 Pulse Amplitude Demodulation

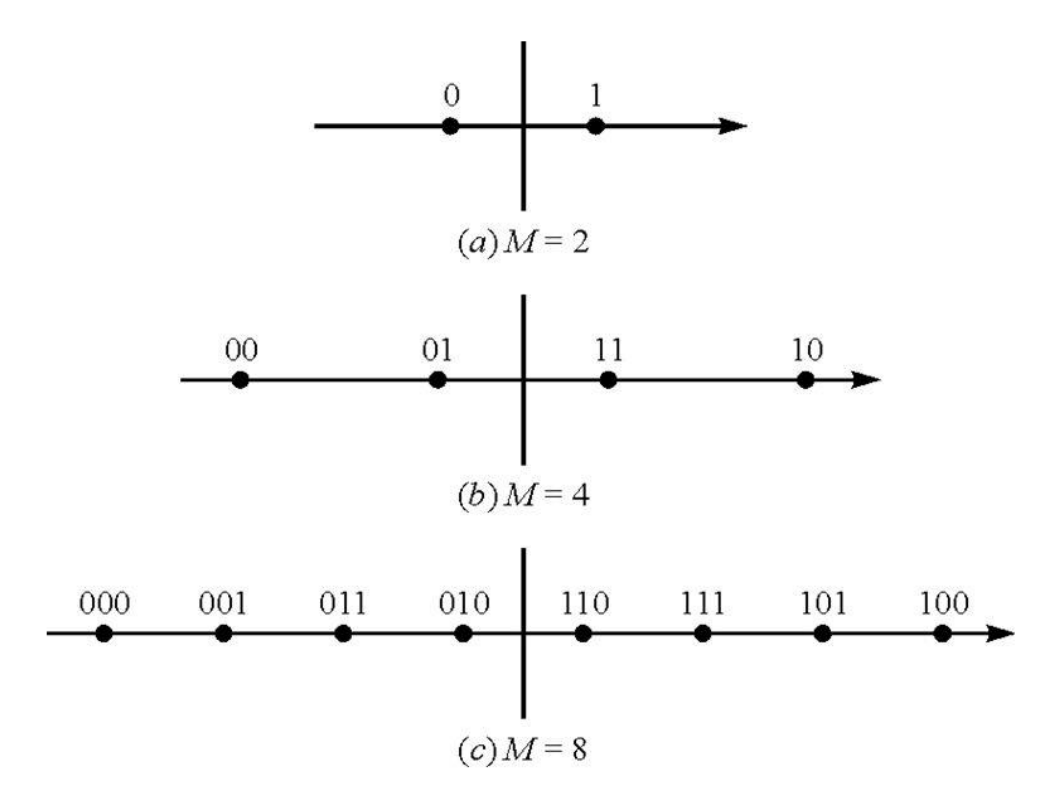


Fig. 14 Signal constellation of PAM-M [32].

Figure 14 illustrates the signal constellation of PAM-M. The demodulation can be done through amplitude comparison of the M-1 levels. After level comparison, each level will be mapped to the corresponding 0 and 1. Then the BER for the transmission can be expressed as Eq. (2.1) through bit-by-bit comparison with the original sequence:

2.4.4 DCO-OFDM Modulation

Applying multi-carrier modulation schemes such as OFDM in VLC has been proposed to boost spectrum efficiency, reduce the multipath effect and suppress frequency-selective fading [28]. OFDM exploits a collection of closely spaced orthogonal sub-carriers to transmit parallel data streams simultaneously, which is also known as discrete multi-tone (DMT). Since each sub-carrier in OFDM is modulated at low speed within a narrow band, channel equalization is simplified compared to wideband modulation. Low-speed subcarriers also facilitate the use of a guard interval between symbols to eliminate ISI. Different from the conventional OFDM used in RF communication, where the generated signal is complex and bipolar, real and positive output is needed for a VLC system because IM/DD is used. Thus, a DC bias is employed by forcing Hermitian symmetry on the subcarriers in the frequency domain for unipolar signal generation in VLC, as shown in Fig.13.

Figure 15 shows the block diagram of DCO-OFDM with bit-and-energy allocation (BEA) modulation and demodulation implemented in the ISEE. The original PRBS signal is firstly quadrature amplitude modulated (QAM). After that, Hermitian symmetry is implemented before inverse a fast Fourier transform (FFT) to ensure a fully real output. It means that the DCO-OFDM is not a constant envelope modulation. And a cyclic prefix (CP) is extended in each frame to eliminate the ISI and inter-carrier interference (ICI) caused by the delay spread of the communication channel. Once the CP length is larger than the channel delay, the system capacity is optimized and so is the system performance. Then, a finite impulse response (FIR) filter is designed to further improve power spectral density and BER.

In the next stage, the modulated signal will be up-sampled and the transient signal will be generated for baseband output with another time dimension added according to the symbol rate setting. The output will be the excitation for an analog transceiver designed in Cadence or ADS. After data is exported from the transient simulation of the transceiver, the function of the AWGN in Matlab will be used for determining the SNR with white noise. Then the data can be synchronized by comparison of a threshold with the addition result of the 32 bit mark signal. For demodulation, the inverse steps are implemented correspondingly.

For the first round, the SNR can be attained to calculate the bit and energy allocations for each subcarrier based on the error vector calculation. Then the transmitted DCO-OFDM signal with a bit and energy allocation algorithm is used for the second round. Finally, going through the same process for the VLC channel link, the BER is calculated for DCO-OFDM with BEA modulation schemes.

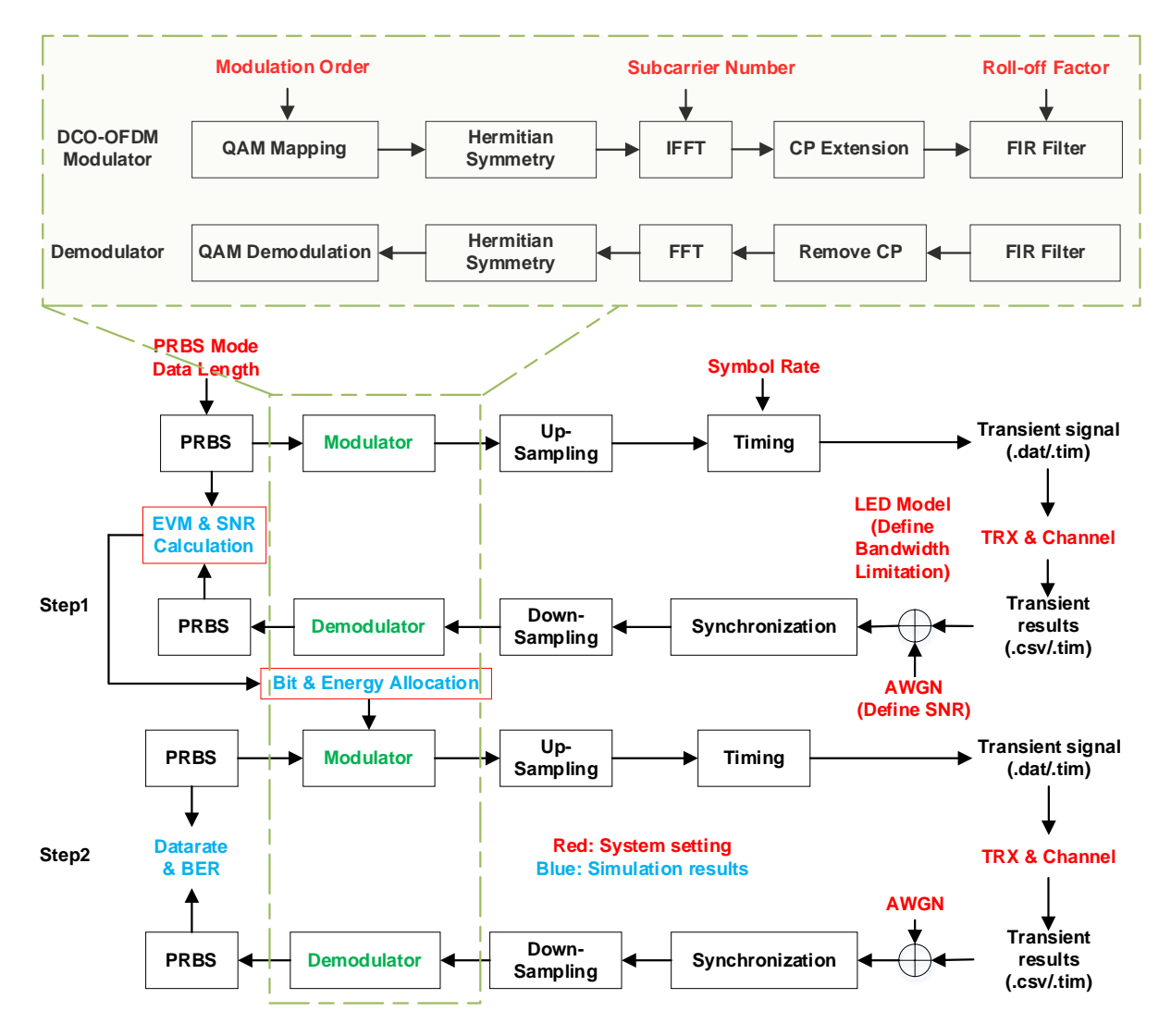


Fig. 15 Block diagram for modulation and demodulation of DCO-OFDM with BEA implemented in ISEE.

The following section gives the mathematical derivation to show the formation of the DCO-OFDM modulation schemes. There will be (N-1)/2 subcarriers in each OFDM frame assuming an N-point inverse fast fourier transform (IFFT) is used in the proposed transmitter.

If K is the total number of bits in one OFDM frame, the bit sequence can be written as $B = [b_1, b_2, b_3, \dots, b_k, \dots, b_k]$, where b_k equals 0 or 1. Then, the sequence is paralleled according to the modulation scheme of each subcarrier. The paralleled matrix is written in Eq. 2.5, where the row number stands for the maximum number of bits of each symbol and the column stands for the number of subcarriers. The effective bits of each row are mapped into the symbol according to the corresponding modulation scheme. The average energy e_n of each subcarrier is set to one in the digital processing for the first round, and then an energy scaling factor is

applied on the modulated symbols to complete the energy loading for the second round. The symbols of one OFDM frame with energy scaling are shown in Eq. 2.6:

$$B = \begin{bmatrix} b_1 & b_{11} & b_{19} & \cdots & b_K & 0 \\ \cdots & \cdots & \cdots & \cdots & \cdots & 0 \\ b_7 & b_{17} & 0 & \cdots & 0 & 0 \\ b_8 & b_{18} & 0 & \cdots & 0 & 0 \\ b_9 & 0 & 0 & \cdots & 0 & 0 \\ b_{10} & 0 & 0 & \cdots & 0 & 0 \end{bmatrix}$$

$$(2.5)$$

$$X = \left[\sqrt{\frac{e_1}{2}}X_1, \sqrt{\frac{e_2}{2}}X_2, \cdots, \sqrt{\frac{e_n}{2}}X_n, \cdots, \sqrt{\frac{e_{N/2-1}}{2}}X_{N/2-1}\right]. \tag{2.6}$$

A typical OFDM data package structure before IFFT and Hermitian symmetry is illustrated in Fig. 16, where the x- and y-axis represent the time and frequency domain, respectively.

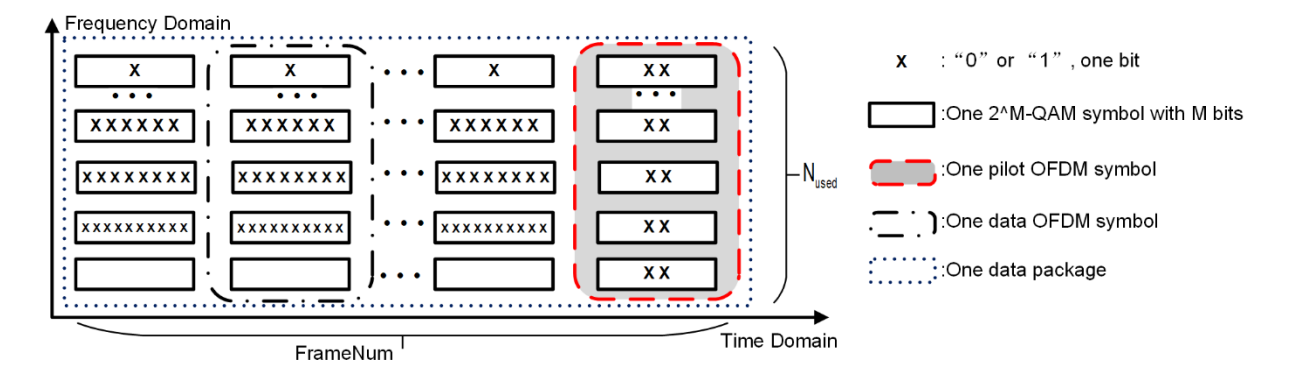


Fig. 16 OFDM data package in the time and frequency domain.

The symbol of the constructed vector after Hermitian symmetry is shown in Eq. 2.7 where $X^*(N-n) = X(n)$, n = 1,2,..., N/2-1. A vector of length N is constructed based on the symbols of one OFDM frame.

$$X = \left[0, \sqrt{\frac{e_1}{2}} X_1, \cdots, \sqrt{\frac{e_{N/2-1}}{2}} X_{N/2-1}, 0, \sqrt{\frac{e_{N/2-1}}{2}} X_{N/2-1}^*, \cdots, \sqrt{\frac{e_1}{2}} X_1^*\right]. \tag{2.7}$$

After that, an IFFT is applied to transform the signal from the frequency domain to the time domain. Then, a CP with length $N_{\rm CP}$ is added to avoid the ISI and synchronization offset

compensation. The DCO-OFDM frame in the time domain can finally be presented as in Eq. 2.8:

$$x(k) = \frac{1}{N} \sum_{n=0}^{N-1} X(n) e^{\frac{-j2\pi n \times mod(k,N)}{N}}$$
 (2.8)

where k is the sampling index ranging from 0 to N+N_{cp}+1.

After performing Hermitian symmetry, IFFT, CP extension and matrix reshaping again, the sequence combined with the pilot sequence is generated for the output of the digital baseband on the transmitter side, as shown in Fig. 17.

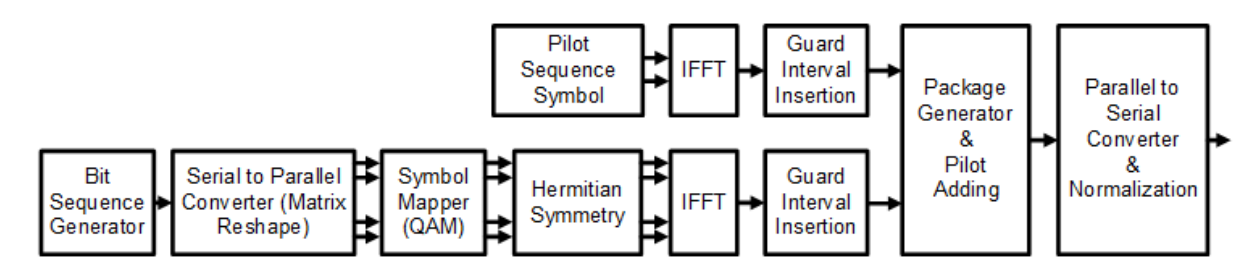


Fig. 17 Modulation of DCO-OFDM on the transmitter baseband.

2.4.5 DCO-OFDM Demodulation

The demodulation steps of DCO-OFDM on the receiver are displayed in Fig. 18. The pilot and data sequence are separated firstly. Then, the pilot sequence is used for synchronization and channel estimation, and the result of the channel estimation is used to recover the transmitted data sequence.

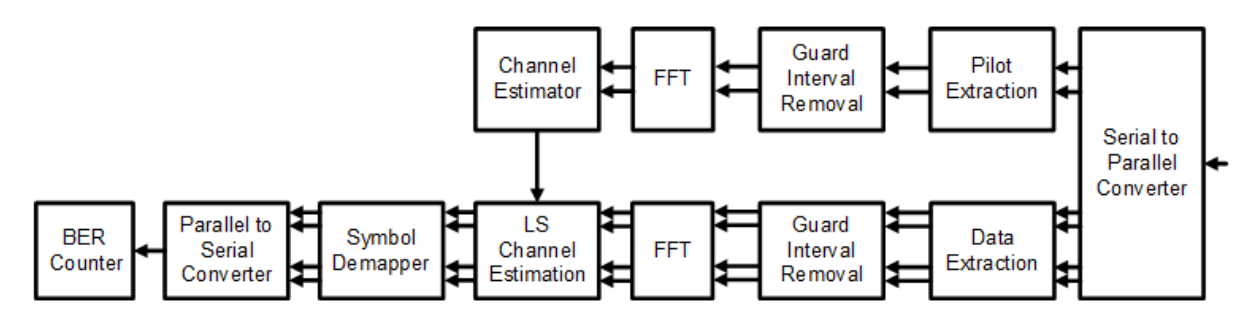


Fig. 18 Demodulation of DCO-OFDM on the receiver baseband.

2.4.6 DCO-OFDM Modulation with BEA

Compared to adopting a fixed modulation scheme and constant energy scaling factor for each subcarrier as in standard OFDM, BEA based on the photonic device properties, optical wireless channel attenuation characteristics, and SNR measurements can achieve better spectrum utilization using DCO-OFDM. The graphical user interface (GUI) of a VLC system employing DCO-OFDM with BEA for simplified operation and broadcast is shown in Fig. 19. The settings for the DCO-OFDM transmission signal and BER target for bit and energy allocation can be input, and the measured SNR, BEA results, transmitter and receiver constellation results, the signal spectrum, and BER results are also shown in the GUI.

The mathematical analysis of BEA is illustrated in the following sections.

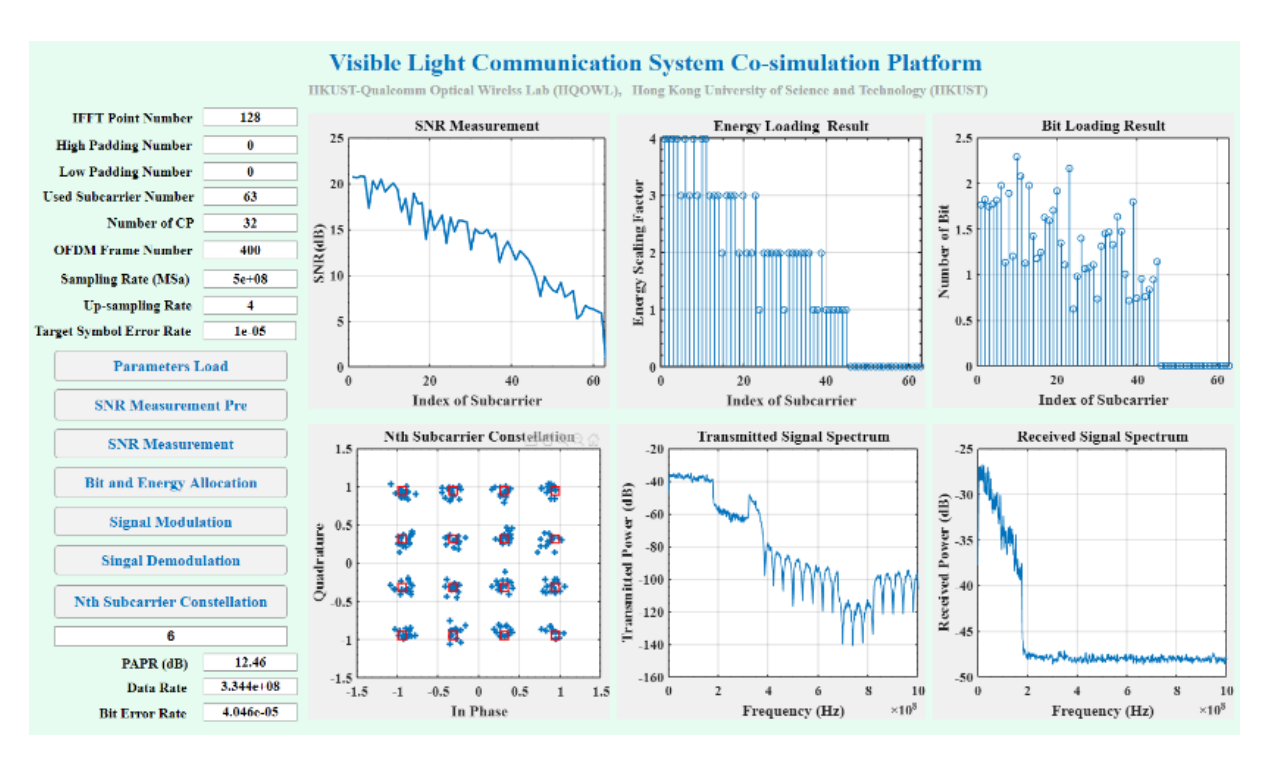


Fig. 19 Graphical user interface of VLC system employing DCO-OFDM with BEA [12].

2.4.7 Bit and Energy Allocation in DCO-OFDM Modulation

2.4.7.1 SNR Estimation Algorithm

A training sequence is employed to estimate the SNR in our design. The SNR is defined as the ratio of the signal power and the noise power, and it can be approximated by Eq. 2.9 when the measured number of symbols is much larger than the categories of modulation symbols:

$$SNR = \frac{Signal\ Power}{Noise\ Power} = \frac{\frac{1}{N} \sum_{n=1}^{N} (V_{I,n})^{2} + (V_{Q,n})^{2}}{\frac{1}{N} \sum_{n=1}^{N} (n_{I,n})^{2} + (n_{Q,n})^{2}},$$
(2.9)

where N is the total number of measured symbols, $V_{I,n}$ and $V_{Q,n}$ are the in-phase amplitude and the quadrature signal amplitude, respectively of the M-ary modulation, and $n_{I,n}$ and $n_{Q,n}$ are the in-phase amplitude and the quadrature noise amplitude, respectively.

Error vector magnification (EVM) is defined as the root-mean-square (RMS) value of a collection of the difference between received symbols and transmitted symbols, which are often shown as a percentage of the average power per symbol of the constellation [29]. It can be estimated through Eq. 2.10:

$$EVM_{RMS} = \frac{\frac{1}{N} \sum_{n=1}^{N} |S_n - S_{i,n}|^2}{\frac{1}{N} \sum_{n=1}^{N} |S_{i,n}|^2},$$
(2.10)

where S_n is the normalized n^{th} symbol and N is the number of symbols in the constellation.

In the proposed model, Eq. 2.10 is employed to calculate the EVM and Eq. 2.11 is then applied to get the SNR of each subcarrier:

$$SNR \approx \frac{1}{EVM^2}.$$
 (2.11)

The BER describes the error probability according to the number of erroneous bits per total bits transmitted. For the DCO-OFDM with the same modulation for each subcarrier, the BER can be attained through Eq. 2.12 [32]:

$$Q = \int_{x}^{\infty} \frac{1}{\sqrt{2\Pi}} e^{\frac{-x^{2}}{2} dy}$$

$$BER \approx \frac{2\left(1 - \frac{1}{L}\right)}{\log_{2} L} Q \left[\sqrt{\left[\frac{3\log_{2} L}{L^{2} - 1}\right] \left[\frac{2 \times SNR}{\log_{2} M}\right]}\right]. \tag{2.12}$$

where L stands for number of levels in each subcarrier of the M-QAM modulation system.

2.4.7.2 Bit and Energy Allocation Algorithm

Using the SNR result in the previous section, the number of bits and energy scaling factor can be decided considering different constraints on bits and energy. They are investigated to be attained through BER-adaptive (BA) [30], which means the minimum BER for a fixed data rate and transmit energy

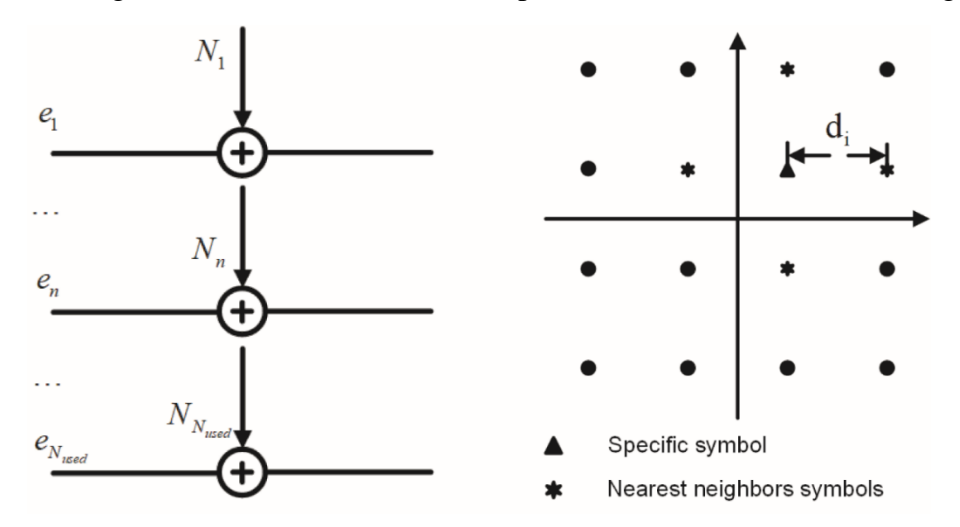
BA, as shown in Eq. 2.13, is finally used for the proposed system with both the transmission energy and rate constraints:

min(*BER*), subject to
$$\sum_{n=1}^{N_{used}} e_n(b_n) \le E_{target}$$
 and $\sum_{n=1}^{N_{used}} b_n = B_{total}$. (2.13)

Then the bit and energy scaling factors are allocated on each subcarrier to minimize the BER.

The basic principle of the algorithm is briefly introduced below.

Considering N subcarriers are used as independent channels, as shown in Fig. 20(a),



(a) Independent channels of each subcarrier. (b) Signal constellation of one subcarrier. Fig. 20 Equivalent channels and constellation of the subcarrier QAM signal.

where e_n is the normalized energy, N_i (i=1,2...n) is the noise variance and n is the index of the subcarrier used. The signal constellation of one subcarrier is shown in Fig. 20 (b).

The symbol error rate of the n_{th} subcarrier using QAM can be calculated with Eq. 2.14:

$$Q = \int_{x}^{\infty} \frac{1}{\sqrt{2\Pi}} e^{\frac{-x^{2}}{2} dy}$$

$$P_{r}$$
 {symbol error for ith channel} = $K_{i} \cdot Q\left(\sqrt{\frac{d_{i}^{2}/4}{N_{i}/2}}\right)$, (2.14)

where d_i is the minimum Euclidean distance between signal points, as shown in Fig. 20 (b), Q is the complementary Gaussian integral function and K_i stands for the interference from the nearest neighbors. The optimum situation is that all subcarriers have the same BER.

When K_n is assumed to be equal for all subcarriers used, the optimum situation can be expressed as Eq. 2.15:

$$\frac{d_n^2/4}{N_n/2} = \dots = SNR_0 = const, \ n = 1, 2, \dots N_{used},$$
 (2.15)

where SNR₀ stands for the squared distance to the decision threshold relative to the noise variance per dimension.

Therefore, the BEA algorithm is transformed to an optimization problem, which is given by Eq. 2.16 under the constraint of Eq. 2.17:

$$\frac{d_i^2/4}{N_i/2} = SNR_0 \text{ to max, } i = 1, 2 \cdots N_{used}$$
 (2.16)

$$B_{total} = \sum_{n=1}^{N} b_n = const$$

$$E_{total} = \sum_{n=1}^{N} e_n = const. \qquad (2.17)$$

After the continuous approximation and Lagrange optimization, we can get the allocated number of bits on each subcarrier as in Eq. 2.18:

$$b_{\rm n} = \frac{B_{\rm total}}{N_{\rm used}} + \frac{1}{N_{\rm used}} \cdot \log_2 \left(\frac{\prod_{l=1}^{N_{\rm used}} N_l}{N_{\rm n}^{N_{\rm used}}} \right). \tag{2.18}$$

In the above calculation, the subcarrier whose b_n is non-positive will be discarded, and the calculation is repeated until the b_i of all the subcarriers used are positive. The number of subcarriers finally used is denoted as N_{used} , and the corresponding indices comprise the set L. Then b_n is quantized to be an integer, as shown with Eq. 2.19:

$$b_{n} = \begin{cases} b_{max}, \ b > b_{max} \\ INT(b+0.5), \ 0.5 < b < b_{max} - 0.5 \ . \\ 0, \ b < 0.5 \end{cases}$$
 (2.19)

Under the constraint of Eq. 2.19, the energy allocated on each subcarrier finally used can be calculated as Eq. 2.20:

$$e_{n} = \frac{E_{\text{total}} \times N_{n} \times 2^{b_{n}}}{\sum_{l=1}^{N_{\text{used}}} N_{l} \times 2^{b_{n}}} . \tag{2.20}$$

2.5 VLC Channel Model

To evaluate and compare VLC system performance using the ISEE in order to solve the problem of the long and expensive verification cycle, the limiting factors of the optoelectronic devices cannot be ignored, as previously illustrated. An equivalent circuit model of the LED and PD for simulation are designed based on the measurement results or given datasheet of a real LED and PD. The intrinsic parameters of PD and LED model are obtained through curve fitting of the frequency response.

2.5.1 Light-emitting Diode (LED) Model

The LED model transforms the driving current into the emitted optical power. Two non-ideal effects should be considered in the LED model: bandwidth limitation and the non-linear effects. Bandwidth limitation occurs in the electrical domain due to the parasitic capacitance, while non-linear effects exist in the transformation between the electrical and the optical domain because the relationship between the input current and output flux is non-linear. However, in the proposed model, the bias point is chosen as the middle point. Thus the non-linearity is ignored in the LED model.

Fig. 21 shows the schematic of the equivalent model, where the C_p stands for the parasitic capacitance, and C_d and R_d represent the diffusion capacitance and impedance of the micro-LED [11] separately. The LED model consists of two parts: 1) the electrical part described by the PCB test fixture, wire bonds, and package, and 2) the intrinsic parameters of the LED. For the optical stage, the current bandwidth versus the current bias can be gained through the same methods. In the LED model, the current bandwidth variation with different bias current is ignored for simplicity.

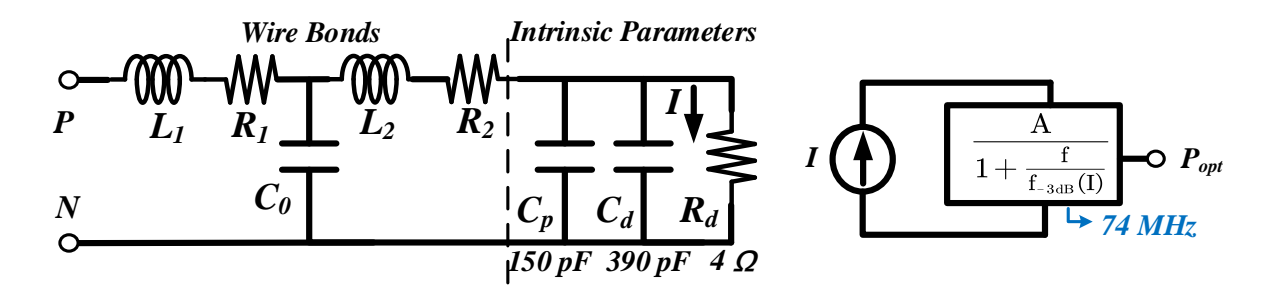


Fig. 21 Equivalent LED model.

2.5.2 Photodiode (PD) Model

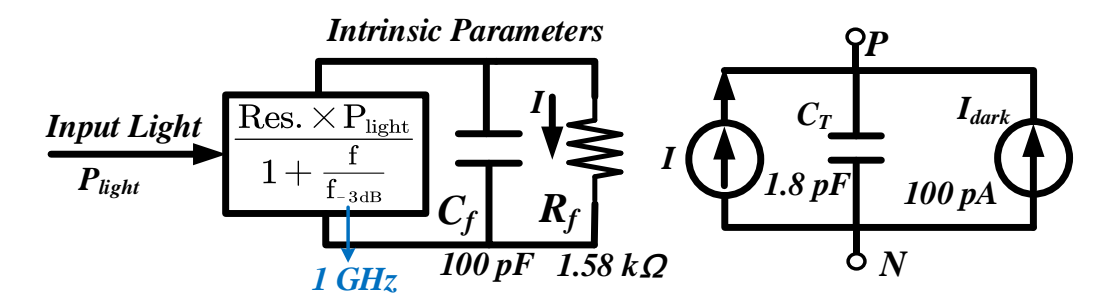


Fig. 22 Equivalent PD model.

The PD modeling is based on the physical manufacturing principles and photoelectric conversion characteristics of the device, using the test results and empirical formulas studied in the past, and the modeling shown in Fig. 22 is obtained. It includes the inherent bandwidth limitation of PDs based on carrier lifetime, photoelectric response and parasitic capacitance, and diode dark current noise. In the PD model, C_T represents the terminal capacitance including PD, pad and wire bonds capacitances. C_f and R_f are the intrinsic parasitic for the -3 dB bandwidth f_{-3dB} of the PD.

2.5.3 Lighting Standards in Practical VLC

In practical VLC, the typical transmit power depends on the application scenario. Using the recommended ~150 lux illumination level of light, the transmit power of LEDs on the ceiling is around 10~20 W to provide illumination over 3~8 m². The transmit power of the LEDs on the table is around 3~6 W to provide illumination over 0.5~2 m².

If the application of the VLC is for precision & detailed works where the level of light may range between 1500 to 2000 lux, the transmit power of the LEDs is around $6\sim12$ W to provide illumination over $0.1\sim0.4$ m².

Considering the above, the LED output power in the proposed design is fixed to 10 W.

2.5.4 Line-of-sight Channel Model

The VLC channel model is shown in Fig. 23, where an LED panel with 10 watt output power is assumed as the transmitter and a PD with a lens is modeled for the receiver. A line-of-sight (LOS) channel model [16] is employed in the proposed design. The frequency response of the VLC channel is considered relatively flat, and the frequency responses of the LED and PD modeled in LOS channel model are shown in Fig. 24 and Fig. 25 respectively. The -3 dB

bandwidth of the LED is modeled as 74 MHz, assuming 4*4 LED arrays are used for the transmitter. The -3dB bandwidth of the PD is modeled as 1 GHz assuming an off-chip PD S5973 is used. The key calculation parameters of the LOS channel model are summarized in Table 2.2.

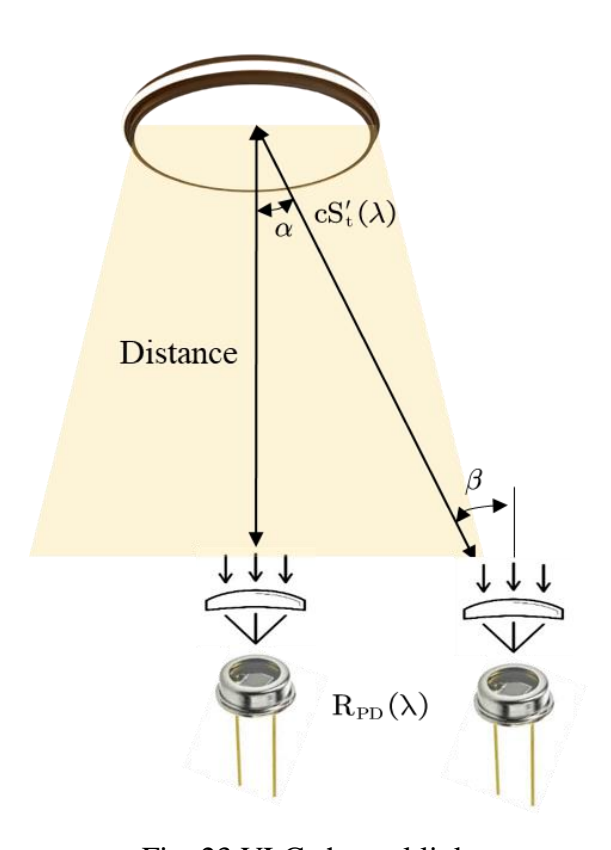
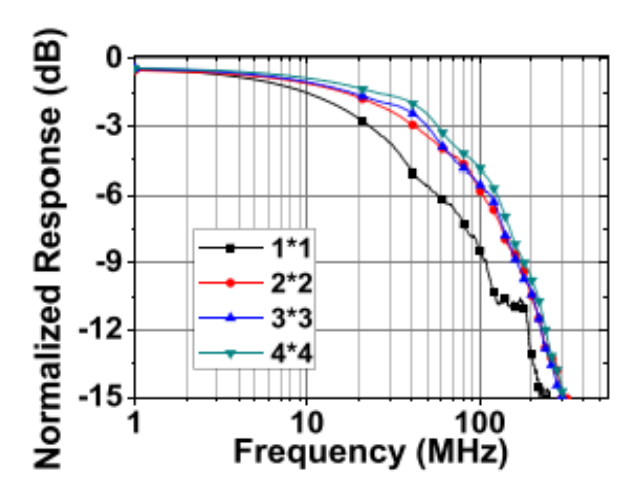


Fig. 23 VLC channel link.

Table 2.2. Calculation parameters of the proposed VLC link model.

	Name	Typical Value	
155.11	-3 dB Bandwidth	74 MHz	
LED Model	Luminous Flux	1000 lm	
(micro-LED) Parameters	Total Transmitte Power	10 W	
Tarameters	Half Power Angle	50°	
	Transmitter Ange	0°	
LOS Channel	Receiver Angle	$0 \circ$	
Characteristic	RX Lens Magnification	Φ_{Lens}/Φ_{PD}	
	Transmission Distance	1 m ~ 3 m	
	Responsivity	0.4 A/W @λ=710nm	
PD Model	Effective Photosensitive Area	0.12 mm^2	
(S5973)	-3 dB Bandwidth	1 GHz	
parameters	Terminal Capacitance	1.8 pF (with parasitic)	
	Dark Current	0.01 nA	



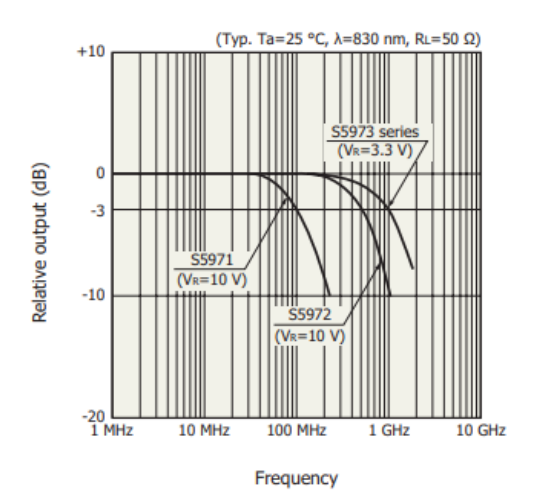


Fig. 24 Frequency response of the equivalent Fig. 25 Frequency response of the PD model LED model [11].

used.

In order to calculate the attenuation of the LOS channel, the transmitter power from LEDs is firstly decided. The transmitter power of one LED is attained through Eq. 2.21.

$$P_{t} = \int_{\lambda_{t}}^{\lambda_{t}} cS'_{t}(\lambda) d\lambda$$
 (2.21)

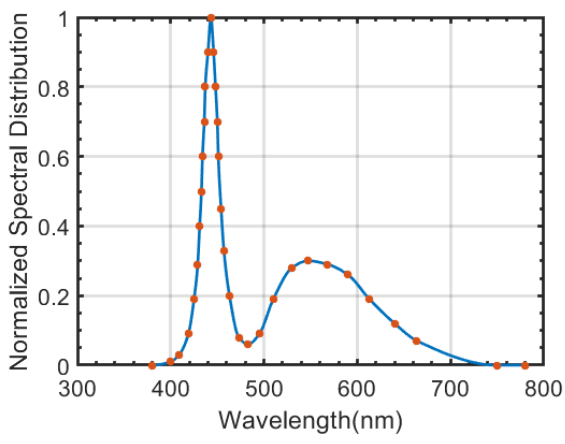
where P_t represents the output power of LED, c stands for the scaling factor and $S'_t(\lambda)$ is the normalized spectrum distribution. The output power of single LED can be gained though Eq. 2.21 where $\lambda_{\!\scriptscriptstyle H}$ and $\lambda_{\!\scriptscriptstyle L}$ are 780 nm and 380 nm, respectively, because visible light is assumed to be used. It is worthwhile to mention that $S_t'(\lambda)$ is available from the datasheet and the $S_t'(\lambda)$ used in the VLC channel is shown in Fig. 26.

The scaling factor c can be gained through Eq. 2.22:

$$c = \frac{\phi_{V}}{683 \int_{\lambda_{L}}^{\lambda_{H}} S'_{t}(\lambda) V(\lambda) d\lambda}$$

$$\phi_{V} = 683 \int_{\lambda_{L}}^{\lambda_{H}} S_{t}(\lambda) V(\lambda) d\lambda, \qquad (2.22)$$

where $V(\lambda)$ is the spectral luminous efficiency function which measures the human eye's response to various wavelengths of light, and ϕ_V stands for the luminous efficiency of the typical LED model.



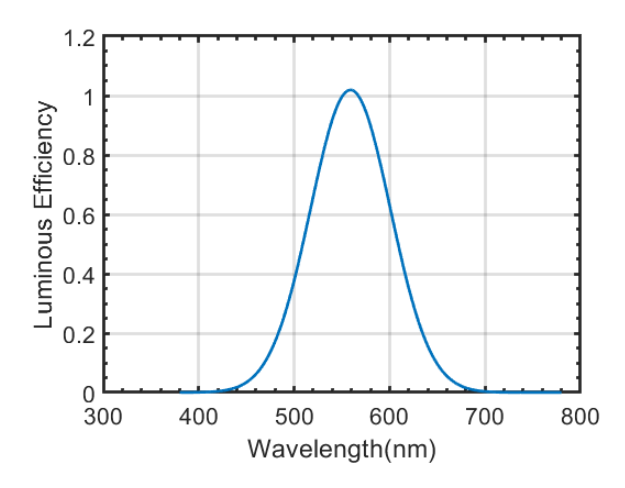


Fig. 26 Normalized spectrum distribution $S'_t(\lambda)$ of equivalent LED model.

Fig. 27 Spectral luminous efficiency of typical LED model.

Approximated by the Gaussian curve shown in Fig. 27, the luminous efficiency $V(\lambda)$ of the typical LED model is represented in Eq. 2.23:

$$V(\lambda) = 1.019 \exp(-285.4(\lambda - 0.559)^2). \tag{2.23}$$

The path loss (PL) of VLC channel attenuation can be calculated as Eq. 2.24:

$$ext{PL} pprox rac{(ext{m}+1) ext{A}_{ ext{Photo_sense}}}{2 \, \Pi ext{d}^2} \cos^{ ext{m}}(lpha) \cos(eta), \tag{2.24}$$

where d is the distance between the LEDs and the PD, α is the transmitter angle, β is the receiver angle, A_{Photo_sense} is the active area of the PD, and m stands for the directivity of the source beam, which is an important parameter for LED light and can be calculated through Eq. 2.24. Assuming the transmitter is right under the receiver for a simple LOS link, both α and β are assigned 0 degrees.

Lambert's mode number m expresses the directivity of the source beam, and can be expressed by Eq. 2.25:

$$m = \frac{-\log 2}{\log[\cos(\theta)]},$$
(2.25)

where θ is the LED semi angle at half power.

The received photo current can be attained through Eq. 2.26:

$$I_{PD} = \frac{1}{2} PL \times M \times \int cS'_{t}(\lambda) R_{PD}(\lambda) d\lambda,$$
 (2.26)

where M stands for the non-imaging concentrator gain, $S'_{t}(\lambda)$ represents the normalized spectrum distribution of the equivalent LED model, c is the scaling factor, which has been

illustrated above, and $R_{PD}(\lambda)$ stands for the responsivity of the PD model as shown in Fig. 28.

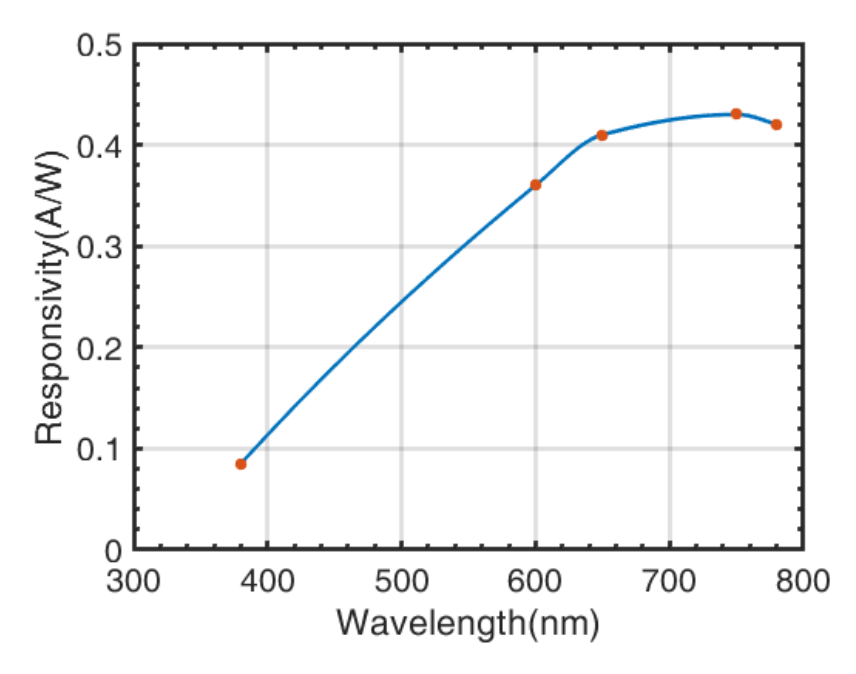


Fig. 28 Responsivity of the PD model used from wavelength of 380 nm to 780 nm.

Since the distance is assumed to be at the meter range, which is quite long compared to the diameter of the lens, the transmitter power angle effect can be ignored. The magnification gain M is calculated in Eq. 2.27:

$$M = (1 - R) \cdot \frac{\Phi_{\text{LENS}}}{\Phi_{\text{PD}}} , \qquad (2.27)$$

where R is the reflection coefficient of the lens, $\Phi_{\rm LENS}$ is the diameter of the lens, and $\Phi_{\rm PD}$ is the diameter of the PD. The reflection coefficient R is derived from Fresnel's equations and calculated through Eq. 2.28 [31]:

$$R = \left[\frac{n_2 - n_1}{n_2 + n_1}\right]^2, \tag{2.28}$$

where n_2 is the indice of refraction of the lens and n_1 is the indice of refraction of the air. n_2 uses 1.74 and n_1 uses 1 in the proposed model. Since the calculated R is very small, for simplicity, a lens with a magnification factor of 100 is assumed before signal reception in the VLC channel model.

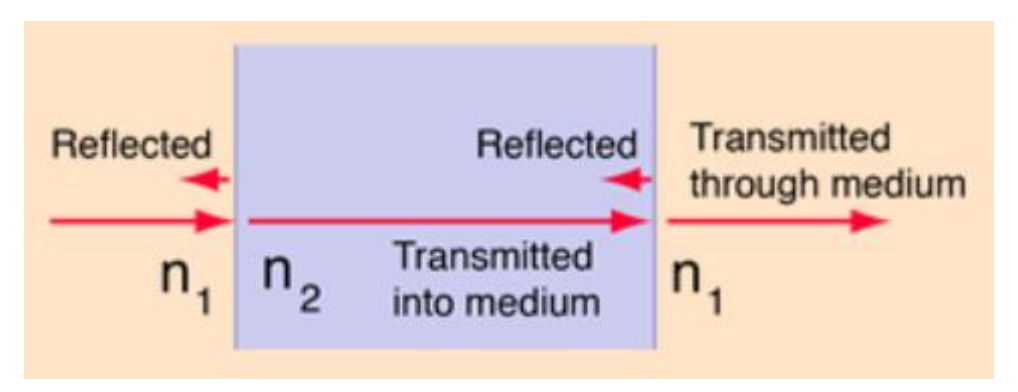


Fig. 29 Model for reflection coefficient calculation [31].

The received photocurrent calculated in Eq. 2.26 versus distance with 10 W transmitter output power is shown in Fig. 30.

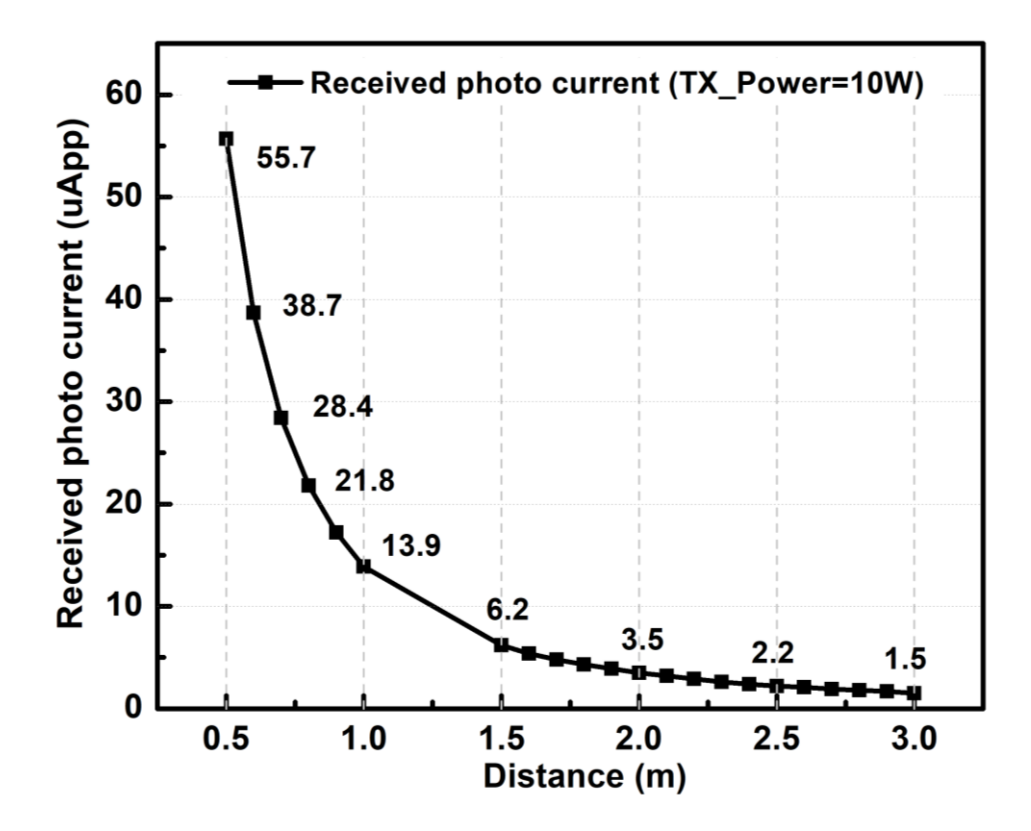


Fig. 30 Received photocurrent versus distance at the receiver side.

After calculating the received photo current, the SNR can be attained through Eq. 2.29 with the simulated input-referred noise current results of the designed receiver.

$$SNR = \frac{I_{PD}}{I_{IRN}}.$$
 (2.29)

CHAPTER 3. VLC RECEIVER SYSTEM-ON-CHIP DESIGN

3.1 Introduction to VLC Receiver SoC

Although significant progress including LED die layout optimization [11], pre- and post- equalization techniques [28], [33] employed in circuit design for bandwidth compensation, and advanced modulation schemes [17] for maximum bit efficiency has been made in visible light communication (VLC) development, most of the demonstrated prototypes are constructed with discrete components, resulting in high power consumption, large form factor, and high cost. Therefore, it is necessary to integrate VLC systems on-chip for practical applications.

Since the optoelectronic devices are significant to the system performance, the VLC receiver SoCs based on Single-photon avalanche diode (SPAD), Avalanche photodiode (APD), and PIN photodiode are summarized in Table 3.1. The comparison of the three PDs has been introduced in Table 1.3. In the comparison table, it is clear that the PIN PD based receivers achieve the highest speed of 2.5 Gb/s in [36], and the SPAD based receivers integrating 4096 elements for photo-sensing achieve the highest sensitivity in [34]. The tradeoffs between a high sensitivity with large photo-sensing areas and a large bandwidth with small parasitic capacitance of the PD are hard to balance from physical considerations. Therefore, the tradeoffs of the noise performance and bit efficiency are the paramount target of the VLC receiver design. Other considerations of the receiver design for the VLC applications are discussed below.

Since light-emitting diodes (LEDs) serve as the transmitter source and the free-space optical wireless channel is used for VLC applications, the bandwidth limitation and interference of ambient light and the environment should be taken into consideration for a low-cost VLC system. Therefore, an ambient light rejection unit is considered significant for canceling the dc interference from the environment to avoid circuit saturation, and an equalization block with high-frequency gain boosting is needed for bandwidth compensation. Additionally, taking account into the low power consumption needed for internet-of-things (IoT) applications, a power-hungry decision feedback equalizer (DFE) is out of the range of choice for the equalization block. Since the receiver targets supporting various modulation schemes, such as PAM-M and DCO-OFDM, the linearity of the receiver should be considered. What is more, similar to the conventional RF wireless system, a wide dynamic range is required to cover a certain variation of the communication distances, and thus a variable gain amplifier is required. It should also be mentioned that the capability of reducing the gain of the receiver is significant to ease the non-linearity requirement for large signal, as is the ability to magnify the small signal to provide a decent amplitude of the buffer output.

Table 3.1. Comparison of VLC SoC receivers with different photodiodes.

Reference	[34]	[35] [36]		[10]
Type	SPAD	APD PD		PD
Technology	130nm	0.35um 0.35um		0.18um
Elements	4096	1	1 1	
Sensitivity (dBm)	-46.1	-34.6	-23	/
Modulation Type	PAM-4, OFDM	ООК	OOK	ООК
Bit Rate	500Mb/s, 350 Mb/s	1000Mb/s	1000Mb/s 2500Mb/s	
BER	2E-3	1E-9 1E-3		1E-4
Consumption (pJ/bit)	230	244	86	92

3.2 Typical Receiver Architecture

The architectures of the typical single-ended and fully-differential receiver systems-on-chip (SoCs) are shown in Fig. 31 and Fig. 32, respectively. A VLC receiver with ambient light rejection and equalization capability is proposed in Fig. 32. It consists of an error amplifier (EA) with a low pass filter (LPF) and a PMOS transistor M_{REJ} as the ambient light rejection module [10].

In the typical optical receiver, a photodiode (PD) converts the optical signal to electric current signal and a trans-impedance amplifier (TIA) is used for further amplifying the signal. A continuous-time linear equalizer (CTLE) to boost the high-frequency gain is used to compensate for the limited bandwidth of the optoelectronic devices. Finally, a multi-stage buffer is employed to increase the gain. A comparison summary of the fully-differential and single-ended VLC receiver is illustrated in Table 3.2.

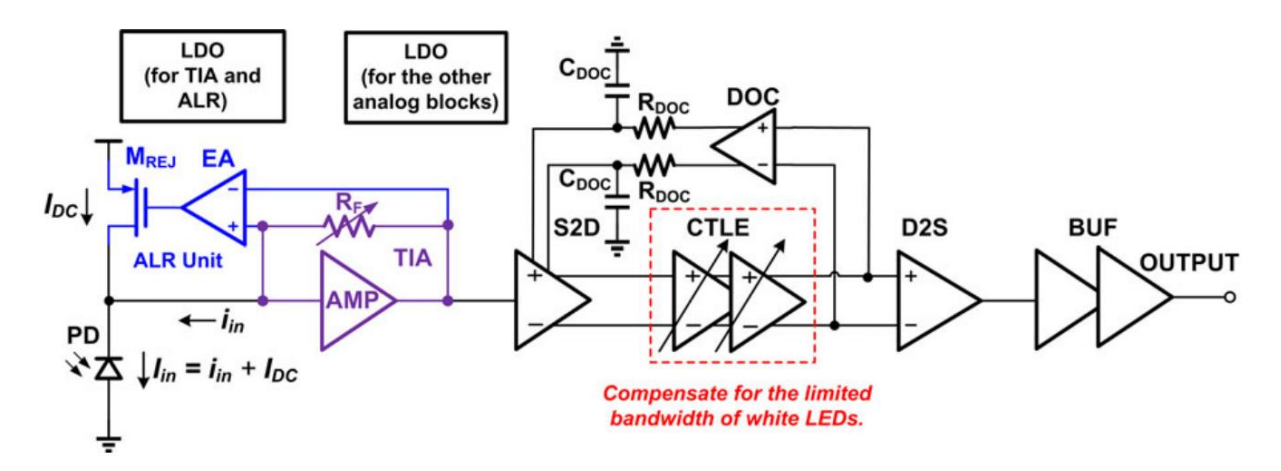


Fig. 31 Architecture of the typical single-ended receiver SoC [10].

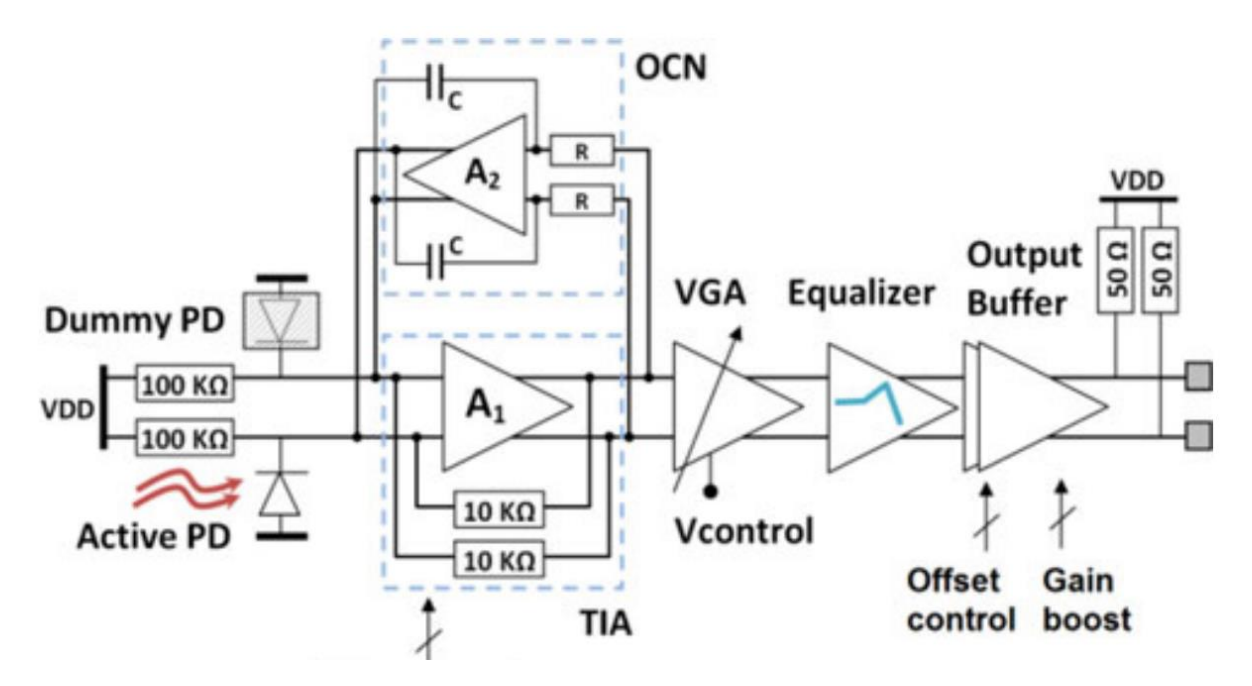


Fig. 32 Architecture of the typical fully-differential receiver SoC [36].

Table 3.2. Comparison of the fully-differential and single-ended VLC receiver.

Structure	IRN	CMRR	PSRR	Power	Area
Fully-differential	×2	high	high	high	large
Single-end	×1	Moderate	Moderate	low	low

3.3 Proposed VLC Receiver Architecture

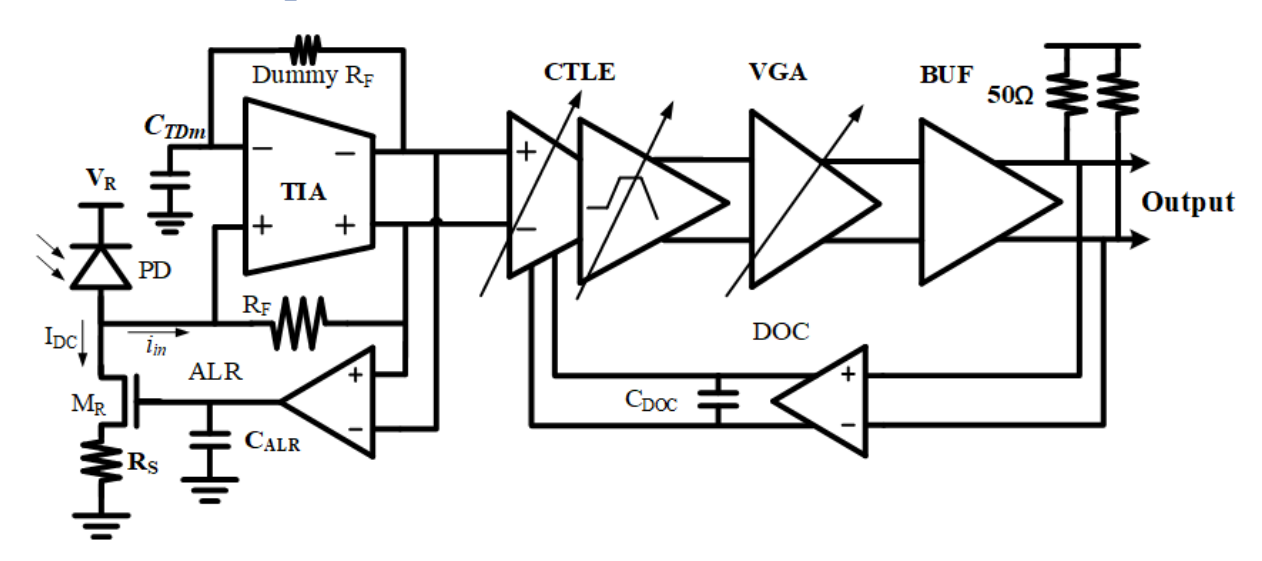


Fig. 33 Proposed VLC receiver architecture.

Based on the considerations discussed in Section 3.2, a VLC receiver is proposed, as shown in Fig. 33. The receiver consists of a TIA, an ambient-light rejection unit, a cascade of two continuous time linear equalizers (CTLEs), a DC offset cancellation (DOC) amplifier, an analog output buffer (BUF), and a variable gain amplifier (VGA) to achieve a good linearity.

The operation principle of the proposed receiver SoC is described: The modulated VLC signal and the other ambient light is detected by the PD and converted into photocurrent I_{in} . The I_{in} flows into the feedback resistor R_F of the TIA and generates a corresponding voltage at its output. At the same time, the voltage drop across the TIA feedback resistor R_F is amplified and low-pass filtered by an EA, which is then used as a control signal for an NMOS transistor to implement ambient light rejection. The CTLE will boost the gain at high frequencies to compensate for the gain loss caused by the low-speed phosphorescent white LEDs. In addition, the DOC module suppresses the potential DC offset due to process variations. Then, the output of the CTLE is further amplified through a the VGA, which is used either to decrease the large signal to decrease the difficulty of designing a buffer with a high linear input range or to avoid the signal being too small, as caused by the long transmission distance. Finally, the signal will be output through the BUF with capability of handling a large capacity load and 50Ω impedance matching.

3.4 Proposed Low Noise Cascode TIA

3.4.1 Introduction to TIA

A trans-impedance amplifier (TIA) is typically used for photo-current amplification. Balancing the trade-off of the TIA design between the input capacitance, mainly comprising of the photodiode (PD), the gain, bandwidth (BW), and noise is significant for transceiver performance, especially when a PD with a large-sensing area for high sensitivity is used in VLC.

The BW of the TIA is determined by the equivalent input impedance and capacitance. Techniques to improve the TIA BW include adding inductive peaking or capacitive feedback [37] to decrease the equivalent input capacitance, using a multi-stage amplifier [38] for gain-boost to decrease the equivalent input impedance, and employing cross-coupled pairs [39]-[41] for either a negative gm or a negative capacitor. However, inductive peaking costs a large area, and capacitive feedback [37] uses multi-stage amplifiers, while using multi-stage TIAs [38] brings additional power consumption and noise.

The negative gm and negative capacitance employed in the inverter-based TIA core in [39] do improve the BW efficiently. However, the noise contribution of the negative gm will be amplified by M3 and the large Miller capacitance C_{gd} cannot be ignored. Adding a negative g_m at both the input and the output of the TIA as in [40] also exhibits efficient BW improvement, but the noise of M3-4 contributes directly to the most sensitive input. The cascode TIA with a negative capacitor proposed in [41] solves the Miller capacitance problem and attains better BW enhancement due to the larger output impedance. However, this larger impedance brings a smaller second pole which will cause poor stability for optical receivers with small PDs. In addition, the corner variation of the cascode TIA is large, and this has not been discussed in [5]. VLC applications using large PDs have a low-frequency dominant pole, which alleviates the stability issue. Furthermore, the TIAs in [39–41] employ cross-coupled pairs on a symmetrical design with a replica dummy side, and thus the noise power and power consumption double.

To address the limitations of the previous work, this paper proposes an asymmetric differential cascode TIA with a scaled dummy side for area, power and noise reduction. An indispensable PMOS negative capacitor and NMOS negative gm are employed for BW enhancement.

3.4.2 Trade-offs of the Shunt TIA

A simplified diagram of the front-end of the VLC receiver is shown in Fig. 34. The PD finishes the optical light-to-electrical current conversion and a TIA provides the current-to-voltage conversion. A shunt-shunt feedback network is employed to provide low equivalent input resistance and thus extend the operation bandwidth, as illustrated in Eq. 3.2.

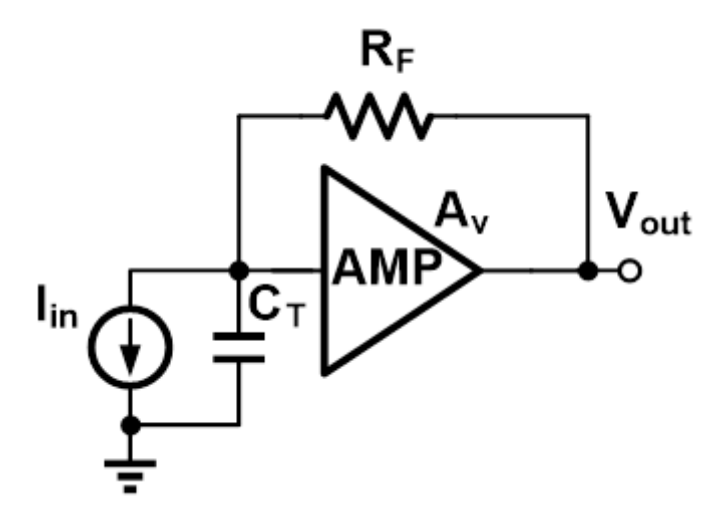


Fig. 34 Simplified front-end of the VLC receiver.

The trans-impedance gain is given by Eq. 3.1:

Trans-impedance gain:
$$Z = R_F$$
. (3.1)

The operation bandwidth is given by Eq. 3.2, assuming that the -3 dB bandwidth is determined by the main pole:

$$BW = main pole = \frac{1}{2\pi R_F C_T}.$$
 (3.2)

Since the most sensitive signal is the received photo-current at the very front of the VLC receiver, the input-referred noise current is given by Eq. 3.3, which mainly consists of the noise of the feedback resistor, the noise of the amplifier and the noise of the NMOS transistor used for ambient light rejection:

$$\overline{i_{\rm eq,in}^2}(s) \approx \frac{4KT}{R_{\rm F}} + \frac{4KT\gamma s^2 C_{\rm GS}^2}{g_{\rm mp} + g_{\rm mn}} + 4KT\gamma g_{\rm mR}, \ i_{\rm n}^2(s) \approx \overline{i_{\rm eq,in}^2}\left(s\right) * \Delta f \label{eq:ieq,in} \tag{3.3}$$

The noise bandwidth BW_n can be calculated as follows [42]:

$$BW_{n} = \Delta f = \frac{1}{H_{0}^{2}} \int_{0}^{\infty} |H(f)|^{2} df , \qquad (3.4)$$

where H(f) is the transfer function of the receiver and H_0 is the midband frequency of H(f).

From the calculations above, the following conclusions can be made about the tradeoffs for the design of the TIA:

- 1. Larger feedback resistor R_F and smaller bandwidth, but larger trans-impedance gain and bandwidth.
- 2. Larger gate capacitance C_{GS}, but larger high-frequency noise induced in the circuit.
- 3. Larger DC current generated from the environmental interference, but larger g_{mR} induced to generate larger noise.
- 4. Larger power consumption of the amplifier, but larger g_m attained to reduce the noise contribution.

3.4.3 Proposed TIA Design

An asymmetric differential cascode trans-impedance amplifier (TIA) employs a PMOS negative capacitor and NMOS negative gm for achieving a 2.8x bandwidth improvement. The scaled dummy side used in the proposed asymmetric design not only leads to area, noise, and power consumption reduction, but brings better bandwidth extension compared to a symmetrical design with a replica dummy side. Using a photodiode (PD) with 1.8 pF parasitic capacitance, the proposed low noise cascode TIA achieves a bandwidth of 2.3 GHz with a transimpedance gain of 75 dB Ω . It also attains a 0.21 uA_{rms} input-referred noise current, the lowest among the comparison TIAs.

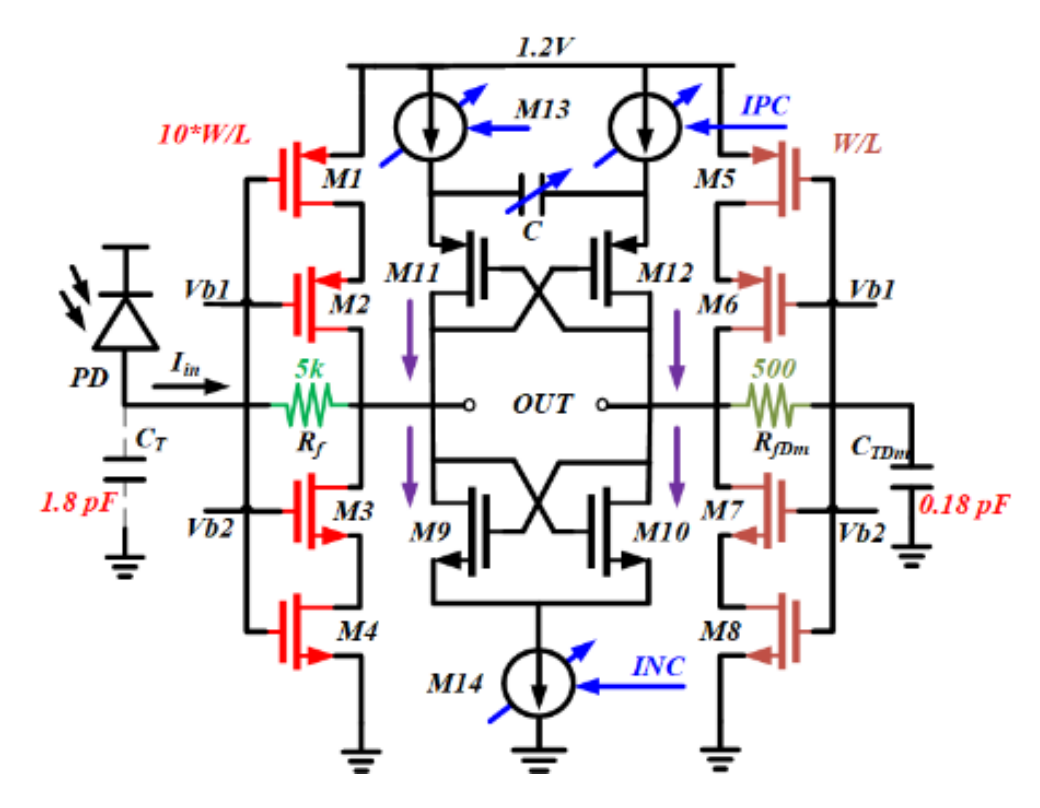


Fig. 35 Schematic of the proposed TIA.

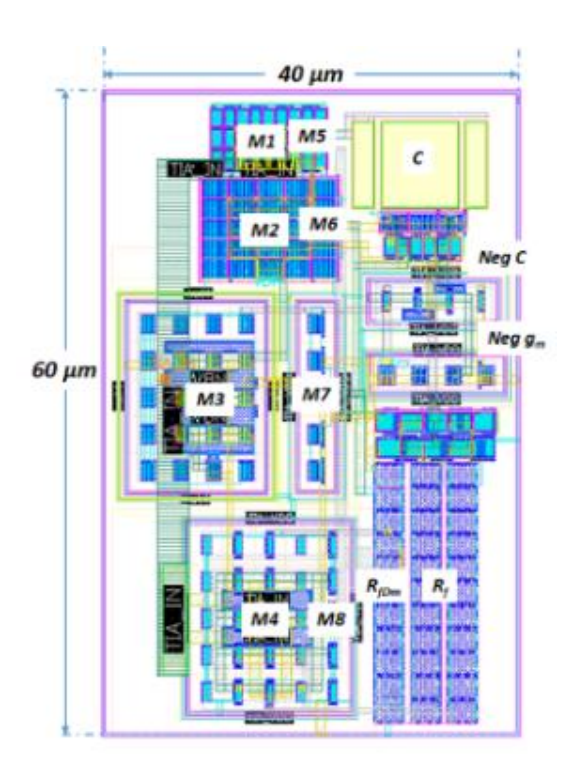


Fig. 36 Layout of the proposed TIA.

The schematic of the proposed TIA design is shown in Fig. 35, and the layout of the proposed TIA is shown in Fig. 36. Vb1 and Vb2 are biased through current mirrors on-chip to keep M1-8 in the saturation region over process corners. The dummy side is scaled down by a factor of 10 to realize the trade-off between power and noise. The current flows from the PMOS negative g_m to NMOS negative g_m . Compared to [41], the additional negative g_m pair brings another dimension for BW extension under corner variations and it is indispensable for the good current flow of the proposed TIA with a scaled dummy side.

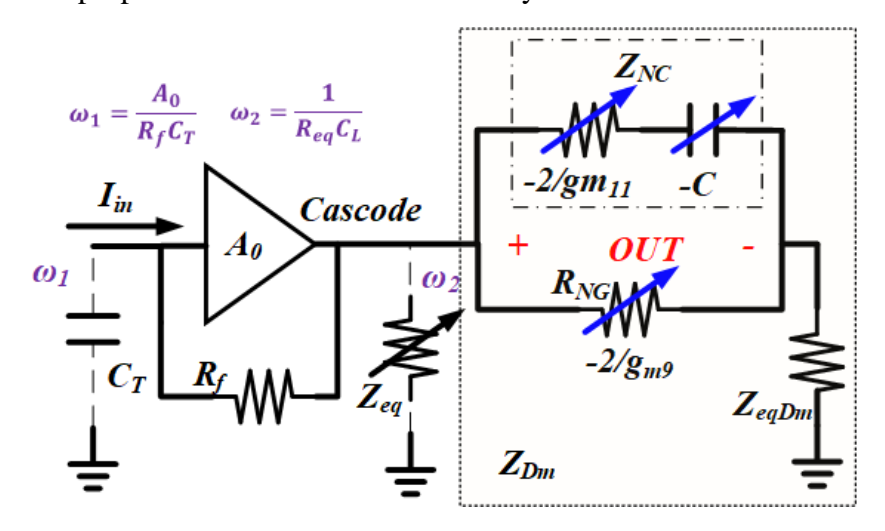
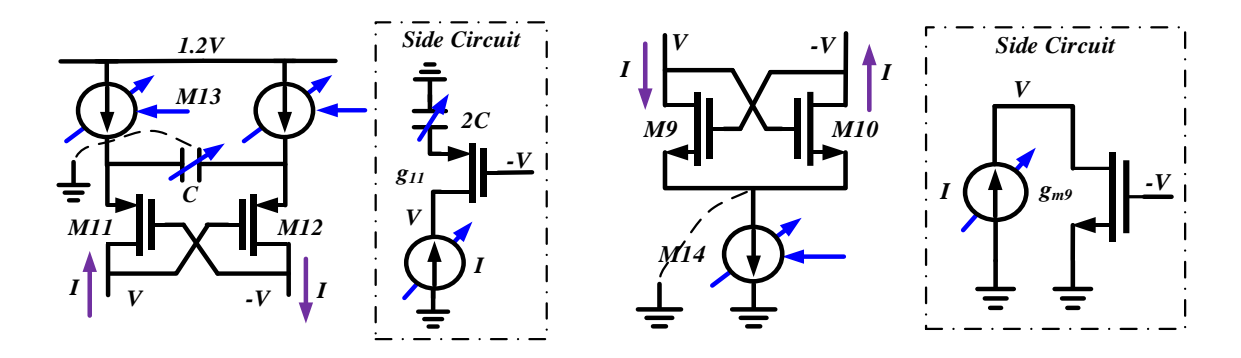


Fig. 37 Equivalent small-signal model of the proposed TIA.

Fig. 37 shows the equivalent small-signal model of the proposed TIA. The impedance of the cross-coupled pairs are simplified as Z_{NC} and R_{NG} . Due to the pseudo-differential input, the dummy side of the TIA is regarded as an equivalent resistor Z_{eqDm} .

Detailed analysis and calculations of the small-signal model in the proposed TIA are illustrated in Eq. 3.5~ Eq. 3.8. Fig. 38 and Fig. 39 shows the small-signal analysis of the PMOS and NMOS cross-coupled pairs respectively.



- a. Small-signal analysis of the PMOS negative capacitor.
- b. Small-signal analysis of the NMOS negative $g_{\rm m}$.

Fig. 38 Small-signal analysis of the cross-coupled pairs.

In Fig. 38(a), the excitation signal V and I are added at the differential output. The half circuit is shown in Fig. 38b and the equivalent impedance $R_{NC} + C_{NC}$ is calculated in Eq. 3.5:

$$I = g_{m11} \left(-V - I \frac{1}{s(2C)} \right)$$

$$R_{NC} + C_{NC} = \frac{2V}{I} = -\frac{2}{g_{m11}} - \frac{1}{sC} , \qquad (3.5)$$

In Fig. 38(b), excitation signal V and I are added at the differential output. The half circuit is shown in Fig. 38b and the equivalent impedance R_{NG} is calculated in Eq. 3.6:

$$I = \frac{V}{r_{o}} - g_{m9}V$$

$$R_{NG} = \frac{2V}{I} = \frac{2r_{o}}{1 - g_{m9}r_{o}} \cong \frac{-2}{g_{m9}}.$$
 (3.6)

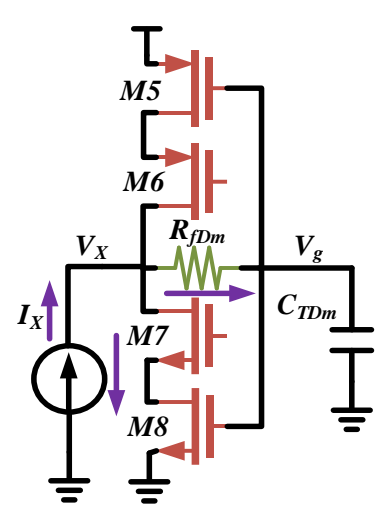


Fig. 39 Small-signal analysis of the scaled dummy side of the proposed TIA.

In Fig. 39, excitation signal V_X and I_X are added at the output end, and the equivalent impedance R_{eqDm} is calculated in Eq. 3.7:

$$V_{g} = V_{X} \frac{\frac{1}{sC_{TDm}}}{R_{fDm} + \frac{1}{sC_{TDm}}} = V_{X} \frac{1}{sC_{TDm}}R_{fDm}$$

$$I_{X} = (g_{m5} + g_{m8})V_{g} + \frac{V_{X}}{R_{fDm} + \frac{1}{sC_{TDm}}}$$

$$R_{eqDm} = \frac{V_{X}}{I_{X}} = \frac{1 + sR_{fDm}C_{TDm}}{g_{m5} + g_{m8} + sC_{TDm}} . \tag{3.7}$$

The equivalent output impedance Z_{eq} of the proposed TIA is attained in Eq. 3.8:

$$Z_{eq} = R_{eqcascode} ||Z_{Dm}; Z_{Dm} = Z_{NC}||R_{NG} + Z_{eq_{Dm}};$$

$$R_{eqcascode} = R_o ||R_f \approx (g_{m2}r_{o2}r_{o1})||(g_{m3}r_{o3}r_{o4})||R_f.$$
(3.8)

Since the TIA BW is extended by a boosted R_{eq} with the negative g_m , the impact of the cascode amplifier BW on the TIA BW cannot be ignored. The second-order transfer function [43] of the TIA is presented in Eq. 3.9:

$$Z_{T}(s) = \frac{-R_{f}A(s)}{A(s) + 1 + sR_{f}C_{T}} = \frac{T_{R}}{s^{2}/\omega_{0}^{2} + s/(Q\omega_{0}) + 1},$$

$$T_{R} = \frac{-R_{f}A_{0}}{1 + A_{0}}, A(s) = \frac{A_{0}}{1 + s/\omega_{2}}, A_{0} = (g_{m1} + g_{m4})R_{eq},$$

$$\omega_{0} = \sqrt{\frac{(1+A_{0})\omega_{2}}{R_{f}C_{T}}}, Q = \frac{1}{2\xi} = \frac{\sqrt{(1+A_{0})\omega_{2}R_{f}C_{T}}}{1+\omega_{2}R_{f}C_{T}} \approx \sqrt{\frac{A_{0}}{\omega_{2}R_{f}C_{T}}},$$
(3.9)

where T_R shows the TIA gain, A(s) represents the cascode amplifier transfer function with a single pole ω_2 , and R_{eq} represents the DC value of the Z_{eq}

Assuming $\xi = \frac{\sqrt{2}}{2}$ for an optimum bandwidth, the TIA BW is shown in Eq. 3.10. A larger R_{eq} with a limitation in Eq. 3.11 for good stability is expected for better BW extension.

$$BW = \omega_0 \sqrt{1 - 2\xi^2 + \sqrt{(1 - 2\xi^2)^2 + 1}} \approx \frac{\sqrt{2}A_0}{2\pi R_f C_T}$$
 (3.10)

$$\xi \ge \frac{\sqrt{2}}{2}, R_{eq} \le \sqrt{\frac{R_f C_T}{2(g_{m_1} + g_{m_4})C_L}}, Z_{C_L} \approx Im(Z_{eq})$$
 (3.11)

The input-referred noise (IRN) current power spectral density calculation [38] for the proposed TIA, neglecting the noise contribution of M2-M3 as well as the noise of the current mirror, is shown in Eq. 3.12. The scaled C_{TDm} and R_{fDm} decrease the thermal noise and high frequency noise of the dummy side shown in Fig. 41(b). Since a larger IPC/INC is used compared to the proposed design with a replica dummy side, the flicker noise of the proposed TIA increases.

$$\overline{\iota_{n,in}^{2}} = \frac{4kT}{R_{f}} + \overline{\iota_{n,in,cascode}^{2}} + \frac{\overline{v_{n,ccp}^{2}}}{R_{f}^{2}} + \frac{\overline{v_{n,in,Dm}^{2}}}{R_{f}^{2}}$$

$$\overline{\iota_{n,in}^{2}} = \frac{4kT}{R_{f}} + 4kT\gamma \frac{|sC_{T}|^{2}}{(g_{m1} + g_{m4})} + \left[\frac{4kT\gamma}{R_{f}^{2}} \left(\frac{2}{g_{m9}} + \frac{2}{g_{m11}}\right) + \frac{K \times (IPC + INC)^{a}}{f^{b}}\right]$$

$$+ \left[\frac{4kTR_{fDm}}{R_{f}^{2}} + 4kT\gamma \frac{|s \times C_{TDm}|^{2} \times R_{fDm}^{2}}{(g_{m5} + g_{m8})R_{f}^{2}}\right], \qquad (3.12)$$

where $v_{n,ccp}$ and $v_{n,in,Dm}$ are the IRN voltages of the cross-coupled pairs and the dummy side, respectively.

3.4.4 Verification of the Proposed TIA

A reference fully-differential cascode TIA, the proposed TIA with a scaled dummy side and with a replica dummy side are both designed using the same parameters. Fig. 40(a) shows that the proposed technique improves the TIA BW from 0.81 GHz to 2.3 GHz with a gain of 75 dB Ω . As shown in Fig. 40(b), the IRN current of the TIA with a scaled dummy side is 0.21 uA_{rms}, 0.04 uA_{rms} lower than the TIA with a replica dummy side. The noise influence on the system performance is illustrated in chapter 4.3.

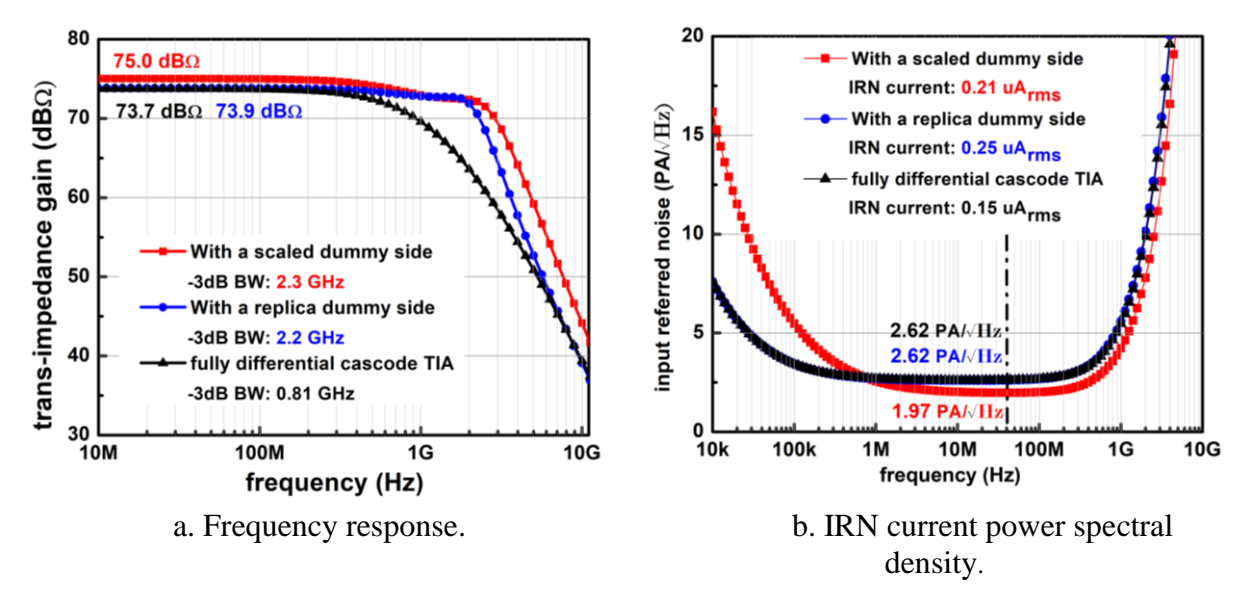


Fig. 40 Bandwidth and noise comparison of the cascode TIA, the proposed TIA with a scaled dummy side. and the proposed TIA with a replica dummy side.

Fig. 41 shows the comparison of the pre- simulation and post- simulation on noise performance which is quite similar. The eye diagrams based on a 2^{15} –1 pseudorandom binary sequence (PRBS-15), presented in Fig. 42, are simulated with the RC-extracted post layout of the proposed TIA, overlaying 2000 periods. These verify the data rate of 4 Gb/s with an input current swing of 2.1 μ A_{pp} through an NRZ signal, and 5 Gb/s data rate with an input current swing of 6.3 μ A_{pp} through a PAM-4 signal.

Table 3.3 presents a comparison with state-of-the-art TIAs. It illustrates that the proposed TIA achieves the lowest IRN current of $0.21~uA_{rms}$ over 2.3~GHz bandwidth for high-speed, long-distance VLC applications using large PDs.

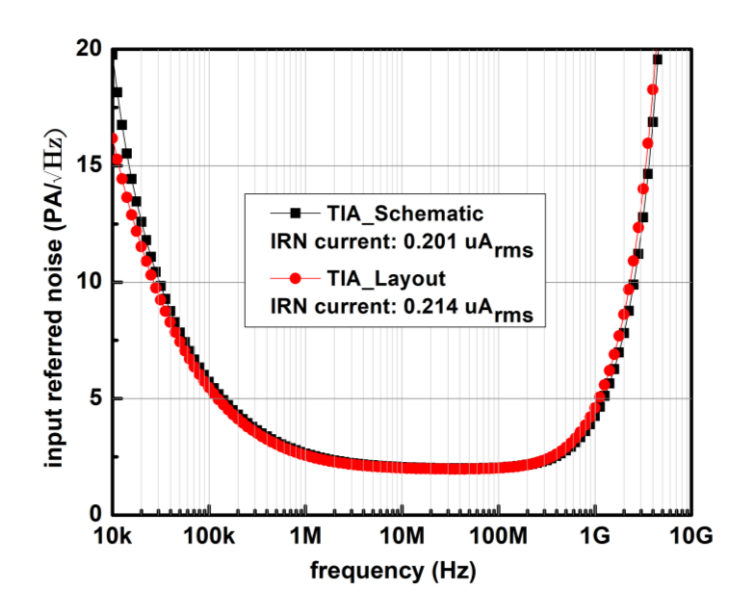
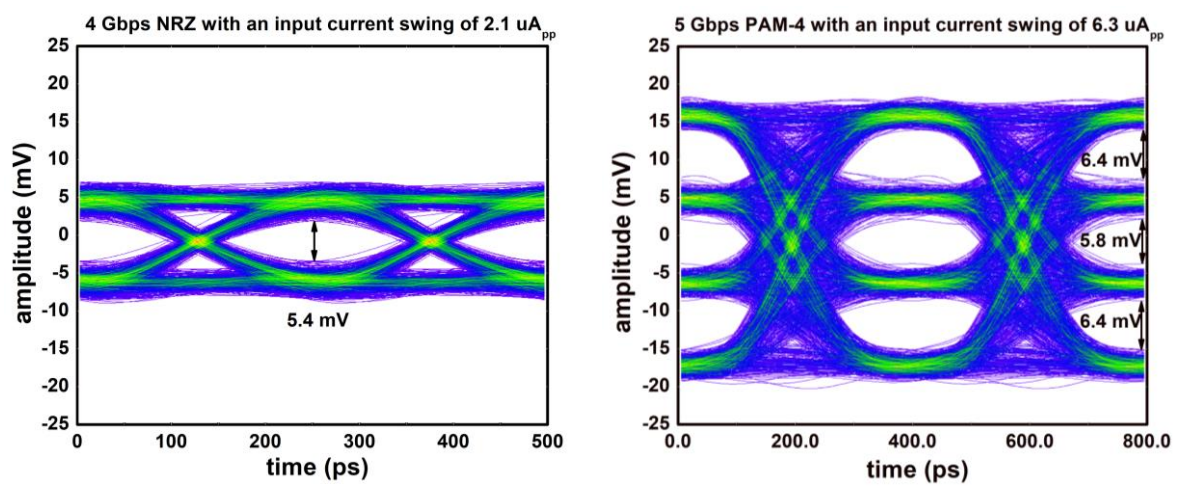


Fig. 41 Comparison of the pre-simulation and post-simulation on noise performance.



a NRZ eye diagram with SNR of 20 dB.

b PAM-4 eye diagram with SNR of 29.5 dB.

Fig. 42 RC-extracted post-layout simulation at the proposed TIA output with noise on.

Table 3.3. Comparison of the proposed TIA with state-of-the-art TIAs

	[37] ^a	[38]	[39]	[40]	[41]	This work ^a
Technology (nm)	40	65	40	28	65	40
Input cap. CT (fF) ^b	500	100	150	250	480	1800
Gain (dB Ω)	89.4	86	54	46	58	75
-3 dB BW (GHz)	3	3.5	6.3	9	12.7	2.3
IRN current (μA _{rms})	0.43	0.30	2.41	9	8.8	0.21 ^e
Power (mW)	1	2.30	91°	10	11	7.34 ^e
Data rate (Gbit/s)	4.3	12	25	25	18	5
Equalizer	no	DFE	CTLE	FIR	CTLE	no
Normalised IRN ^d (m)	3.7	4.6	12.4	21	8.9	1.42

^aSimulated

3.4.5 Corner Variation Compensation of the Proposed TIA

As in Fig. 44, the cascode TIA BW degrades severely at the FF corner and at high temperature because $R_{eqcascode}$ decreases at the FF corner and g_m decrease at high temperature. Thus larger g_{m9-12} and C are required to decrease $|Z_{Dm}|$ for corner variation compensation (CVC) at FF corner and high temperature according to Eq. 3.15. $R_{eqcascode}$ changes from ~1.5 k Ω at SS corner to ~450 Ω at FF corner. Fig. 43 shows the simulated negative impedance for CVC in

^bExcluding the parasitic capacitance from the TIA input stage

^cPower of the TIA+LA

^dNormalised IRN = IRN(μA_{rms})/ $\sqrt{C_T(fF) \times (BW(GHz))^3}$ [44].

the proposed design with C tuning from 0.1 pF to 0.9 pF and the IPC/INC tuning from 0 to 800 uA. Fig. 44 shows the simulated bandwidth over corners with a phase margin (PM) above 60° after CVC. The proposed TIA achieves a BW of over 2.1 GHz and the BW variations of less than 10 %.

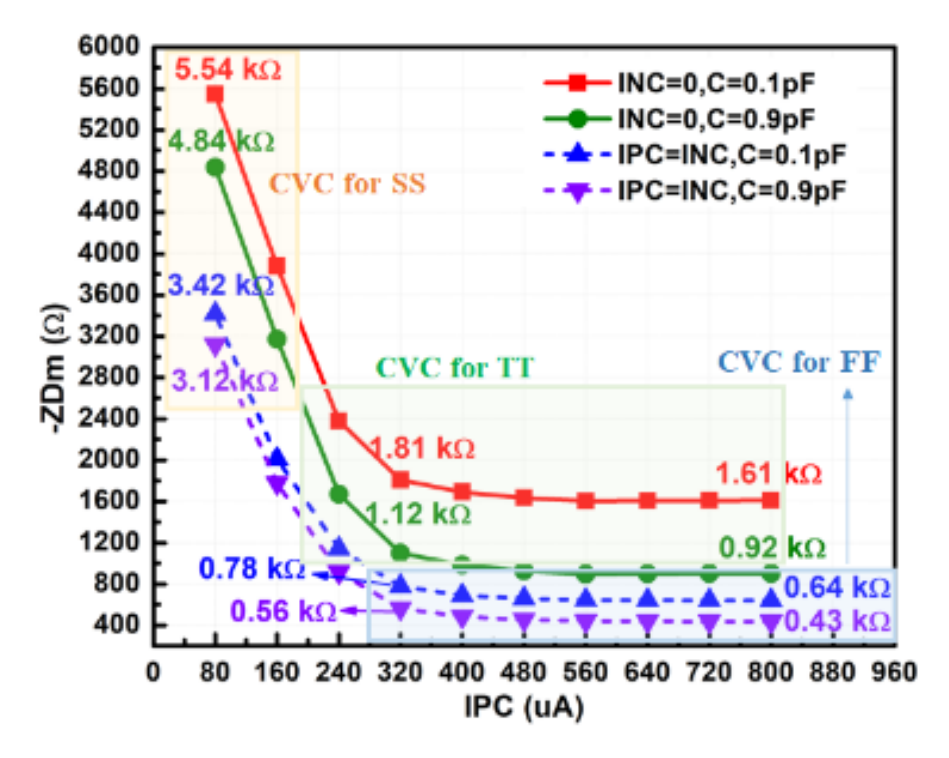


Fig. 43 Simulated negative impedance for corner variation compensation.

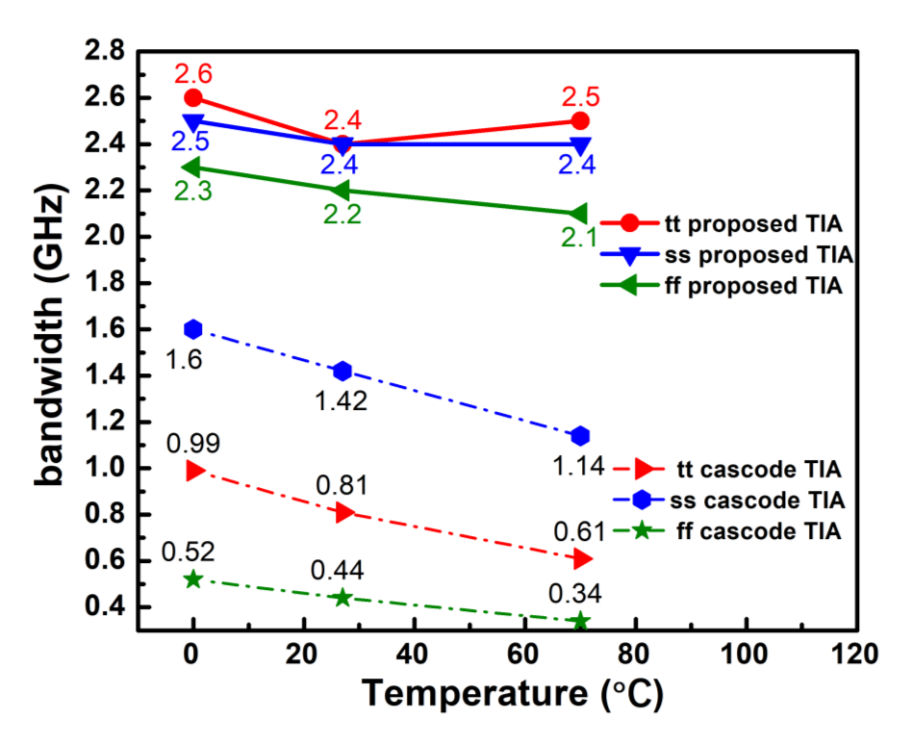


Fig. 44 Simulated bandwidth over corners of the fully-differential cascode TIA and the proposed TIA.

3.5 Continuous Time Linear Equalizer

At the receiving end, one reason for the deterioration of signal quality is channel loss, and the main function of a CTLE at the receiving end is to compensate for the loss of high-frequency components of the signal in the channel, thereby improving the quality of the received signal and reducing the BER.

The designed continuous-time equalizer adopts a two-stage current-mode logic (CML) architecture, as shown in Fig. 45. The first-stage CTLE uses a parallel resistor and capacitor at the source to gain low-frequency degeneration, while the second-stage CTLE uses a resistor and capacitor in series to generate two adjustable zeros under the same power consumption to achieve pole compensation and bandwidth expansion.

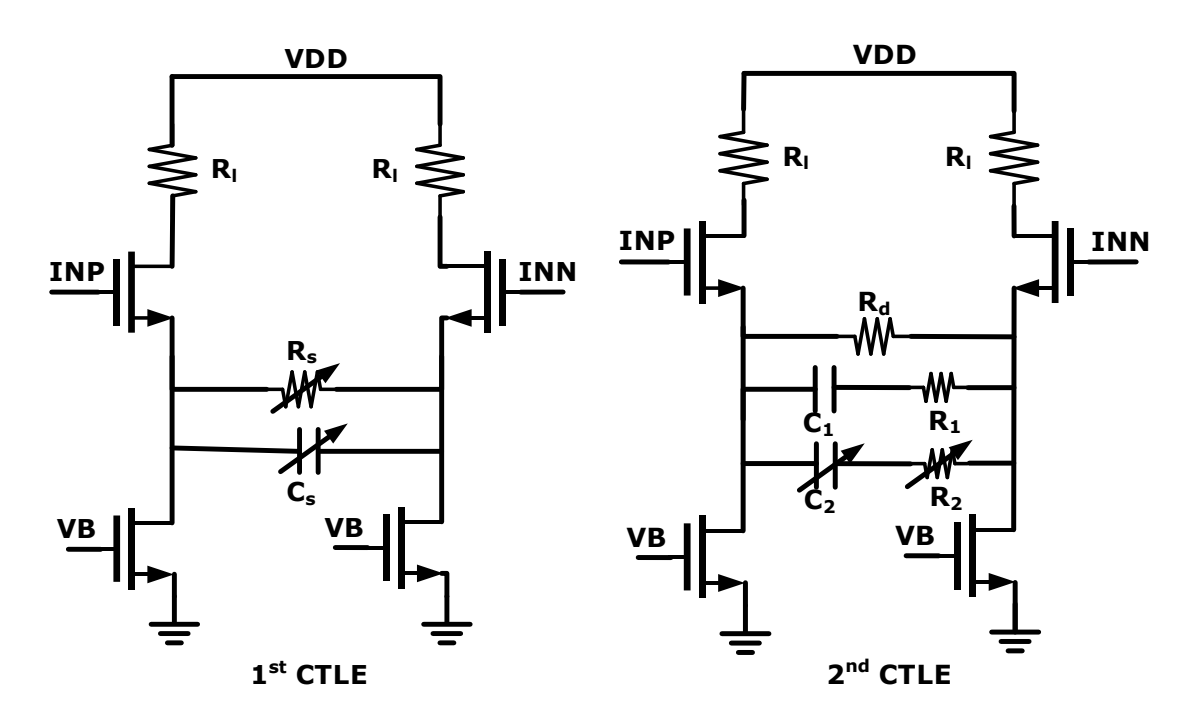


Fig. 45 Schematic of continuous time linear equalizer.

The transfer functions of the two CTLE stages are calculated as Eq. 3.14 and Eq. 3.15 respectively.

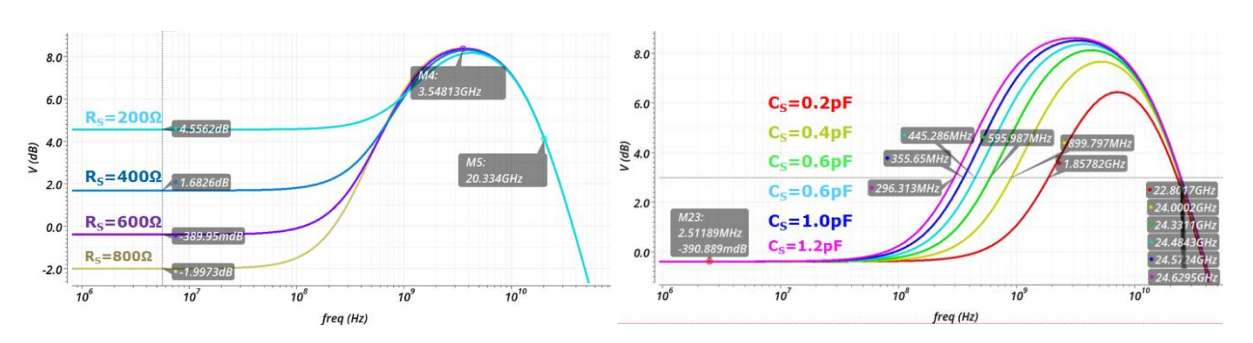
$$H_{1} = \frac{-g_{m}R_{1}}{1 + \frac{g_{m}R_{S}}{2}} \frac{1 + sR_{S}C_{S}}{1 + s\frac{R_{S}C_{S}}{1 + \frac{g_{m}R_{S}}{2}}} \frac{1}{1 + sR_{1}C_{1}},$$
(3.14)

with
$$\omega_z=\frac{1}{R_sC_s};~w_p=\frac{1+g_mR_s/2}{R_sC_s}$$
 generated in the first-stage CTLE, and

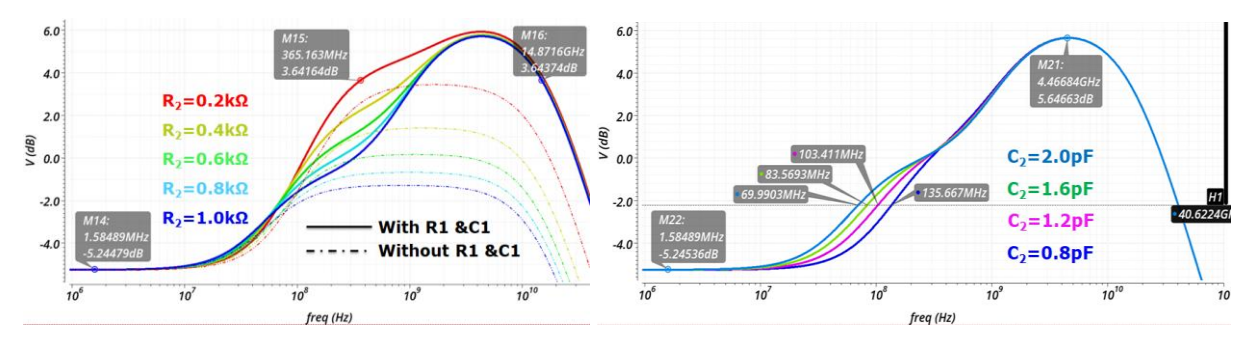
$$H_2 = \frac{-g_m R_1}{1 + g_m Z_S}; Z_S = R_d | | \left(R_1 + \frac{1}{sC_1} \right) | | \left(R_2 + \frac{1}{sC_2} \right),$$
 (3.15)

with two zeros generated in the second-stage CTLE.

The AC response simulation results of the individual CTLE stages are shown in Fig. 46, and the tuning range for DC gain and achievable equalization can be gained from adjusting Rs, Cs, R₂, and C₂. The ac response simulation results show that the design of the CTLEs works in conjunction with multiple zeros in the frequency domain, which is beneficial to more flexibly compensate for high-frequency loss, increase the compensation range of the CTLE, and further improve its compensation capability to achieve a higher transmission rate. What is more, the eyes at different process corners can be compensated to open widely and recover the signal with adjustable peaking of the CTLEs.



(a) AC response of the first-stage CTLE.



(b) AC response of the second-stage CTLE.

Fig. 46 AC response of the CTLE with adjustable peaking.

3.6 Other Blocks

3.6.1 Ambient Light Rejection Unit

It is noted that the free-space optical wireless channel is adopted for VLC, and the PDs respond to all light sources received. The interfering light source will also be converted into a DC signal to change the operating point of the circuit, which greatly affects the working and linearity of the communication receiver. Therefore, the ambient light rejection (ALR) unit formed by a negative feedback loop is specially designed to eliminate the direct current light

source of optical communication and the ambient light that produces interference, which expands the use range and environment of the optical receiver. In the proposed receiver architecture, an ambient light rejection loop can eliminate the interference light below 1 mA, which is 200 times the ac light signal. It means that the ambient light, which is more than 200 times stronger than the output power of the VLC light signal will saturate the receiver, but it can still be solved by modifying the ALR design. Therefore, the saturation limit is defined by the photodiode, and the value is 15 mA photocurrent, 3000 times the ac light signal.

However, the use of the ALR loop introduces current thermal noise of the M_R at the input, which is proportional to the transconductance of the MOSFET. This means that the greater the DC that is suppressed, the greater the transconductance, and the greater the noise. Therefore, R_S is introduced at the source end of the MOSFET, as shown in Fig. 34, to reduce the equivalent transconductance, thereby reducing the effect of additional noise. The amplifier used for the ALR unit is shown in Fig. 47.

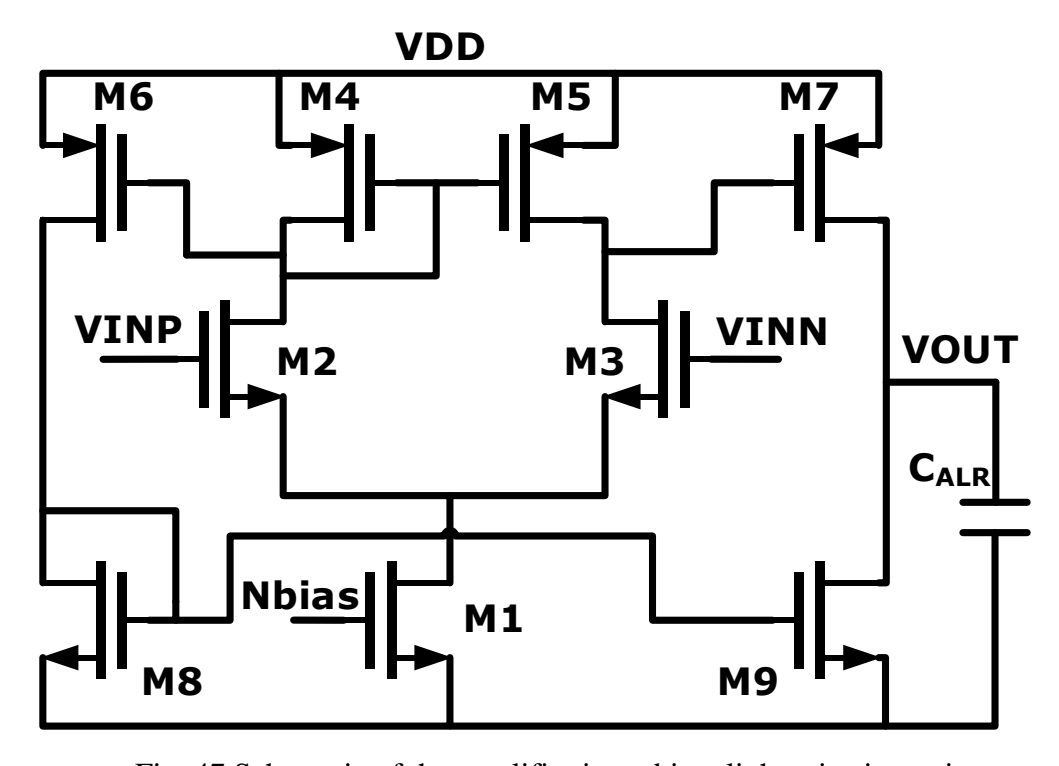


Fig. 47 Schematic of the amplifier in ambient light rejection unit.

The error amplification gain and the cut-off frequency is calculated as follows:

$$A_{V_{ALR}} = g_{m2} \frac{1}{g_{m4}} \times g_{m6} \frac{1}{g_{m8}} \times g_{m9} (r_{o7} | | r_{o9}) + g_{m3} (r_{o3} | | r_{o5}) \times g_{m7} (r_{o7} | | r_{o9})$$

$$\omega_{ALR} = \frac{1}{(r_{o7} | | r_{o9}) \times C_{ALR}}.$$
(3.16)

3.6.2 DC Offset Cancellation Unit

A DC offset suppression loop is proposed to provide a certain common mode deviation suppression. It can also overcome matching problems to gain a balanced differential output under process variations. The amplifier used for DOC is shown in Fig. 48.

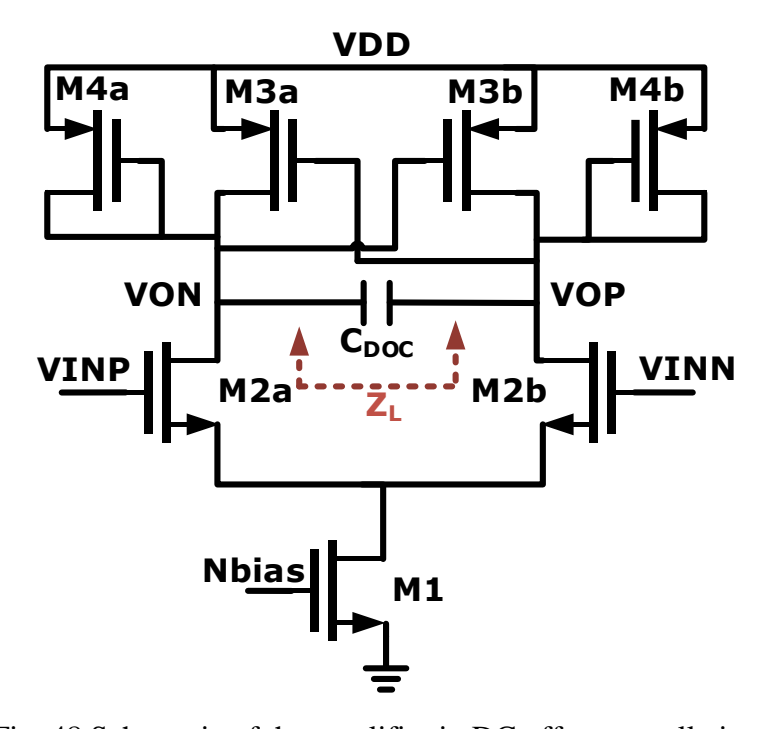


Fig. 48 Schematic of the amplifier in DC offset cancellation.

The error amplification gain and the cut-off frequency are calculated as follows:

$$\begin{split} Z_{L} = Z_{g3} || Z_{g4} = -\frac{2}{g_{m3}} || \frac{2}{g_{m4}} = \frac{2}{g_{m4} - g_{m3}} \\ A_{V_DOC} = g_{m2} Z_{L} \\ \omega_{DOC} = \frac{1}{\frac{Z_{L}}{2} \times 2C_{DOC}} = \frac{1}{Z_{L} \times C_{DOC}} \ . \end{split} \tag{3.17}$$

3.6.3 Variable Gain Amplifier

The VGA used in our design adopts the traditional Gilbert architecture. It uses different current ratios to achieve different gain control, amplifies or limits different input signals, and achieves signal linear output and a wide receiver range. The variable gain range is shown in Fig. 50.

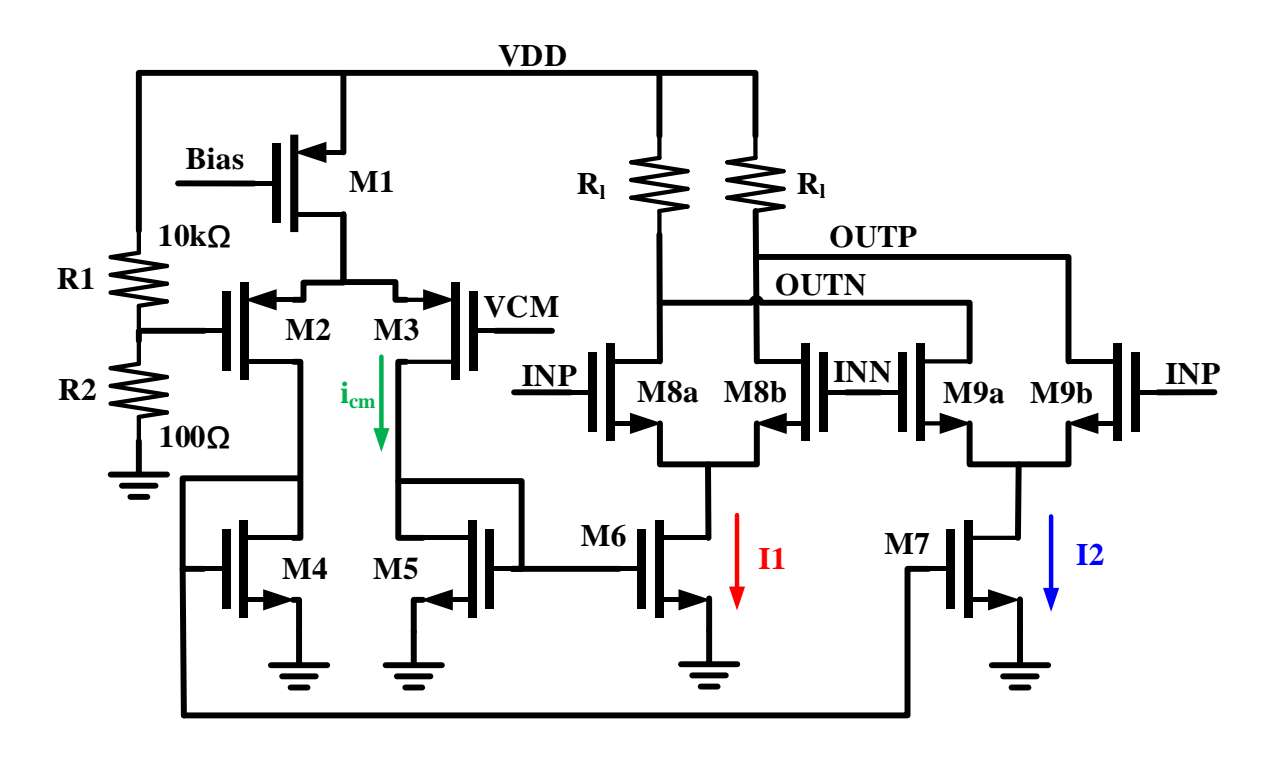


Fig. 49 Schematic of the variable gain amplifier.

The gain of the VGA can be calculated as Eq. 3.18:

$$A_{V_{\perp}VGA} = (g_{m8} - g_{m9})R_1 = \left(\frac{2I_1}{V_{gs} - V_T} - \frac{2I_2}{V_{gs} - V_T}\right)R_1 = \frac{2(I_1 - I_2)R_1}{V_{gs} - V_T} \ . \eqno(3.18)$$

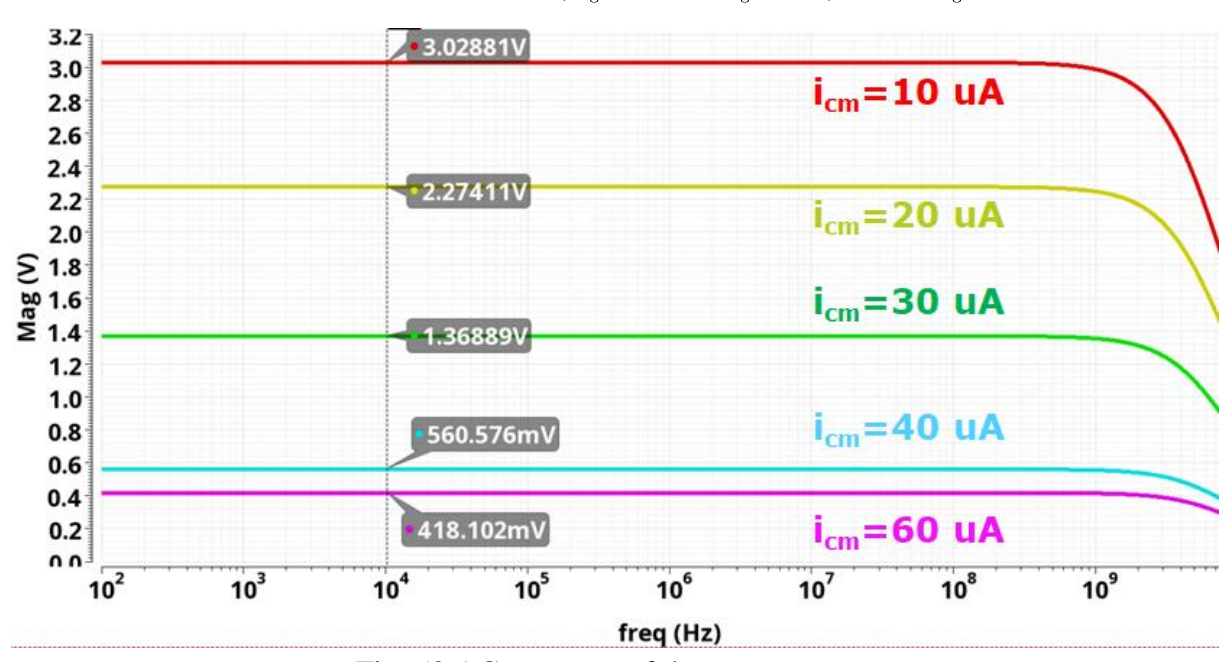


Fig. 50 AC response of the variable gain amplifier.

3.6.4 Analog Buffer

In the proposed VLC receiver, an analog buffer is designed for supporting advanced modulation schemes like PAM-4 and DCO-OFDM, as shown in Fig. 51. A 50 Ω load is utilized

in the design for impedance matching. Transient PAM-4 eye simulation with 0.16 V and 0.24 V input swing is conducted, as shown in Fig. 52, to provide the direct linearity requirement for the input of the buffer.

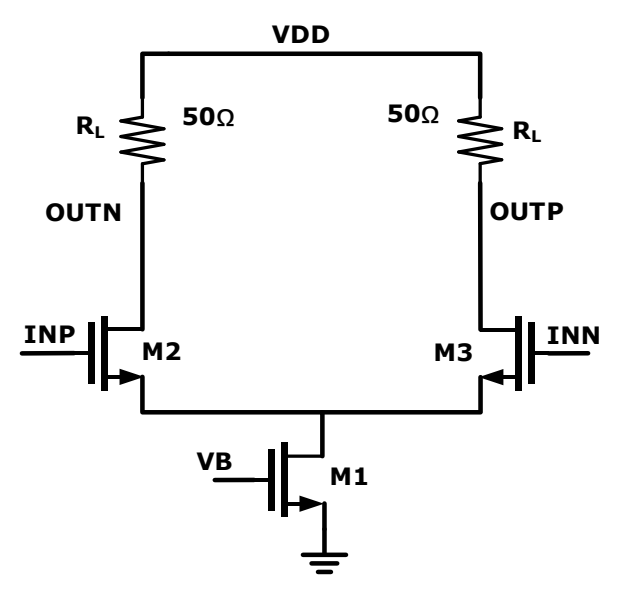


Fig. 51 Schematic of the analog buffer.

The gain of the buffer can be easily attained as $A_V=g_mR_L$.

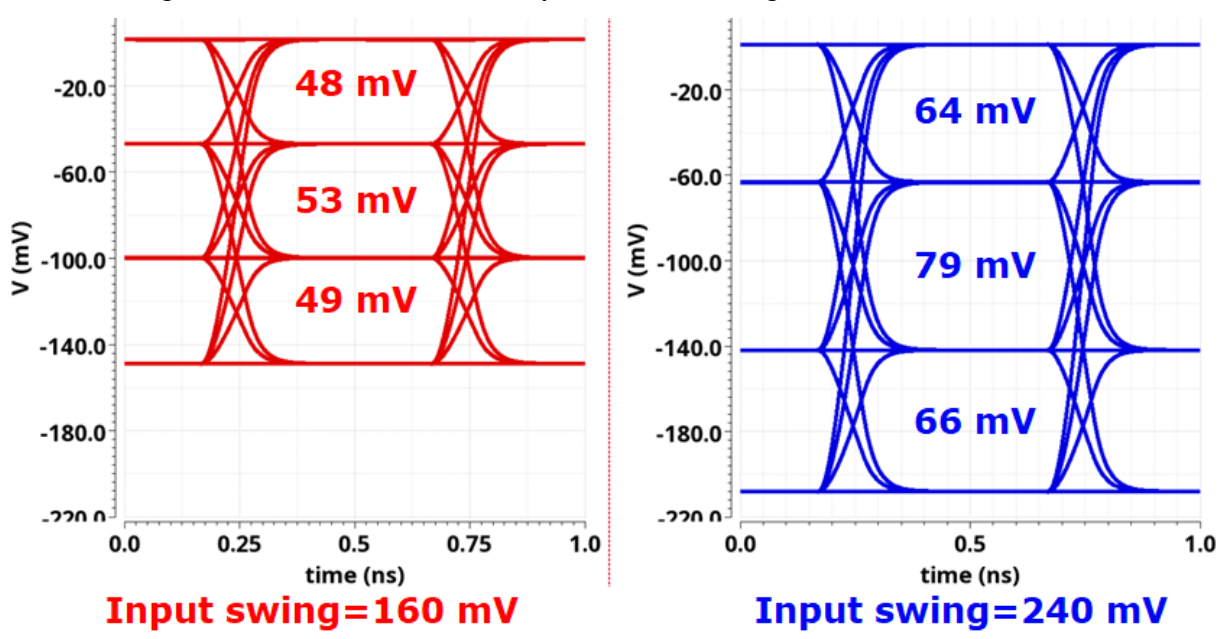


Fig. 52 Transient PAM-4 eye simulation of the analog buffer.

CHAPTER 4. VLC TRANSCEIVER DESIGN AND EVALUATION

4.1 VLC Transceiver with Pre- and Post- Equalization

Part-I Integrated System Evaluation Engine

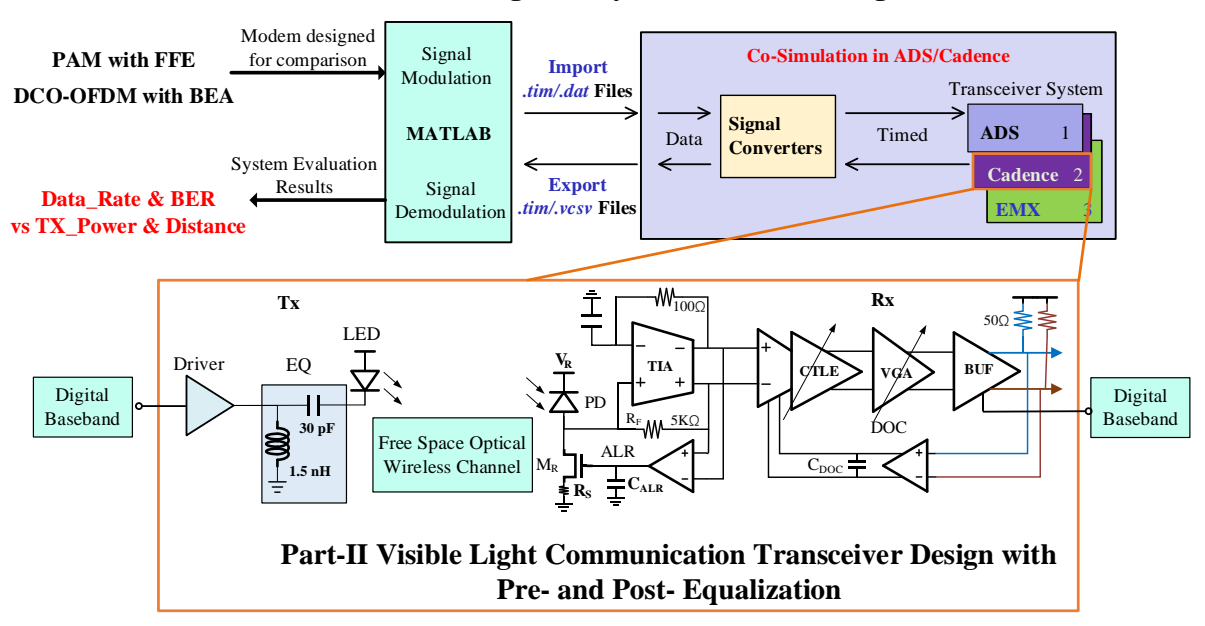


Fig. 53 Diagram of the VLC transceiver design and evaluation through ISEE.

A diagram of the visible light communication (VLC) transceiver design and its evaluation through the integrated system evaluation engine (ISEE) is shown in Fig. 53. The descriptions of the ISEE can be found in Chapter 2, and the block designs of the VLC receiver integrated circuit (IC) are illustrated in Chapter 3.

The model of the VLC channel is given in Chapter 2, where a light-emitting diode (LED) of 74 MHz -3dB bandwidth and a photodiode (PD) of 1 GHz -3dB bandwidth are utilized for the VLC transceiver design. Additionally, the VLC receiver uses PDs with a large sensing area for high sensitivity. Using an off-chip PD S5937 with an 1.8 pF parasitic capacitance, the proposed trans-impedance amplifier (TIA) achieves a trans- impedance gain of 74 dB Ω and a -3 dB bandwidth of 2 GHz.

At the transmitter, the proposed design models the power amplifier module ZHL-6A+ as the driver, which consumes the power of 8.4 W to provide 22 dBm power output to drive the LEDs. Besides, there is a pre- equalizer including a passive LC equalizer and an optional feed forward equalizer (FFE) implemented at the baseband. At the receiver, there is a two-stage continuous time linear equalizer (CTLE) architecture is utilized. The two equalizers work in conjunction to compensate the VLC channel bandwidth, as illustrated above.

4.1.1 Pre- Equalizer at the Transmitter

4.1.1.1 Passive Equalizer

The schematic of the passive equalizer used in the proposed design is shown in Fig. 54. Its structure is the same as a high-pass filter to boost the high-frequency gain loss, and the L and C values are determined as follows:

$$L = \frac{1 \text{ H} \times 50}{2\pi \times f_{\text{target}}} \tag{4.1}$$

$$C = \frac{1 \text{ F}}{50 \times 2\pi \times f_{\text{target}}} . \tag{4.2}$$

From the AC simulation results shown in Fig. 55, the bandwidth extension of the LED from 74 MHz to 470 MHz at the cost of signal attenuation is verified.

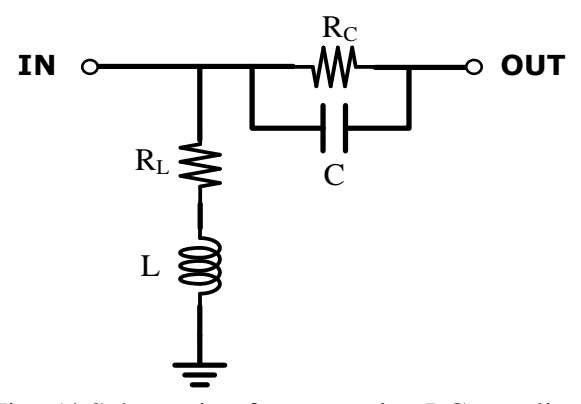


Fig. 54 Schematic of pre- passive LC equalizer.

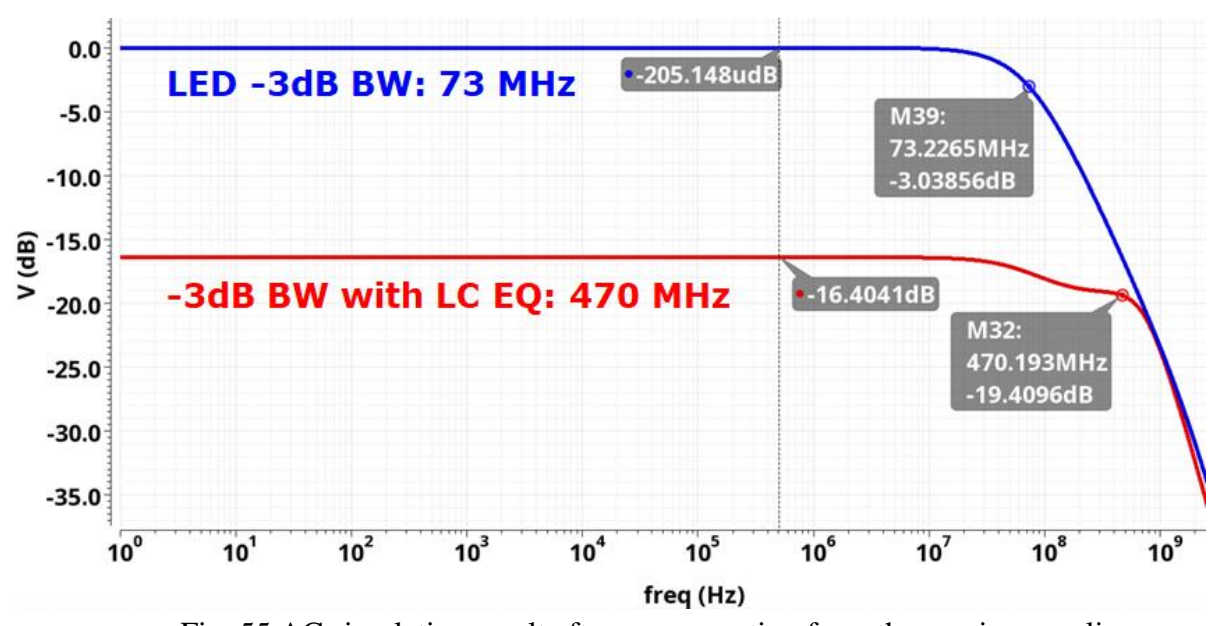


Fig. 55 AC simulation result after compensation from the passive equalizer.

4.1.1.1 Feed-forward Equalizer

Working in addition to the passive LC equalizer, the feed-forward equalizer introduced in Chapter 2 is optional for pulse-amplitude modulation (PAM) schemes. The tap numbers and coefficients of the FFE are determined by the pulse response of the VLC transceiver at the target Nyquist frequency.

4.1.2 Post- Equalizer at the Receiver

A two-stage continuous time linear equalizer (CTLE) follows to compensate for the limited modulation bandwidth of the LEDs and PD. The micro-LEDs used for the VLC link have a -3 dB bandwidth of 74 MHz, and the PD has a -3 dB bandwidth of 1 GHz. The passive LC pre-equalizer as shown in Fig.56 extends the modulation bandwidth of the transmitter to 460 MHz and the transceiver bandwidth falls back to 220 MHz after the bandwidth limitation of the PD. Shown in Fig. 9(a), the two-stage CTLE extends the whole transceiver bandwidth from 220 MHz to 1.45 GHz.

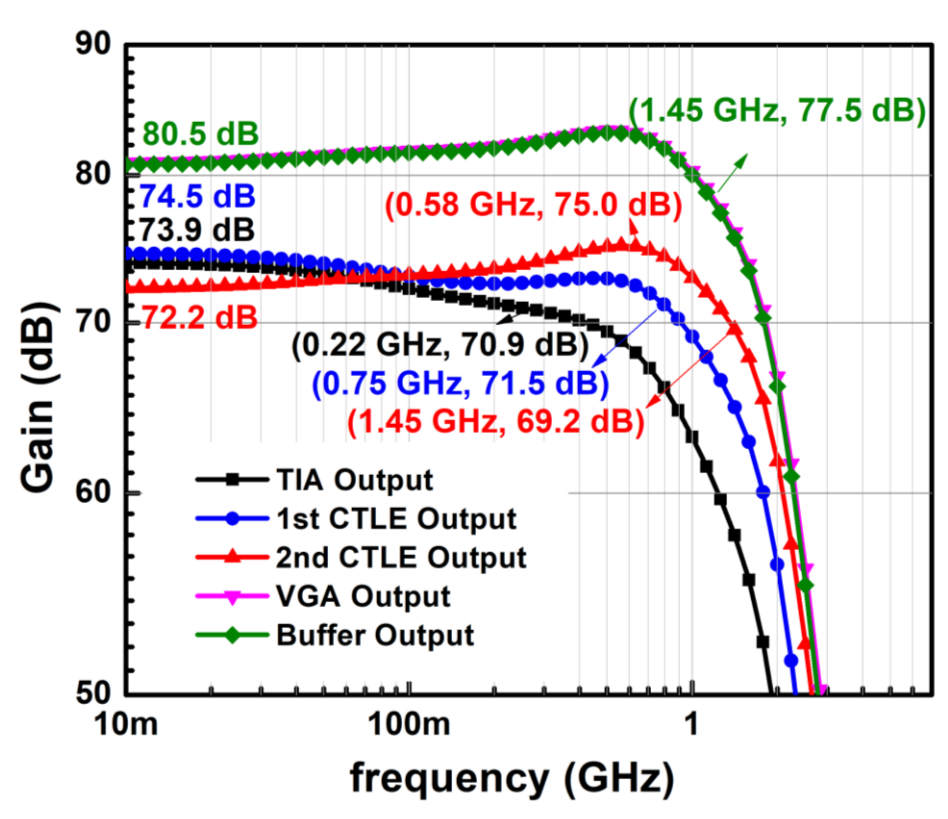


Fig. 56 AC response of the overall transceiver.

4.1.3 Simulation Results of the Equalizers

The simulated eye diagrams of the transceiver with/without the CTLE are provided in Fig. 57. The signal is corrupted at 3 Gb/s after passing the high-frequency attenuated channel. Using the two-stage CTLE to boost the high-frequency gain, the signal is recovered because

the eye opens after the CTLE. It is worth mentioning that the eye diagrams in Fig. 57 are all simulated with noise.

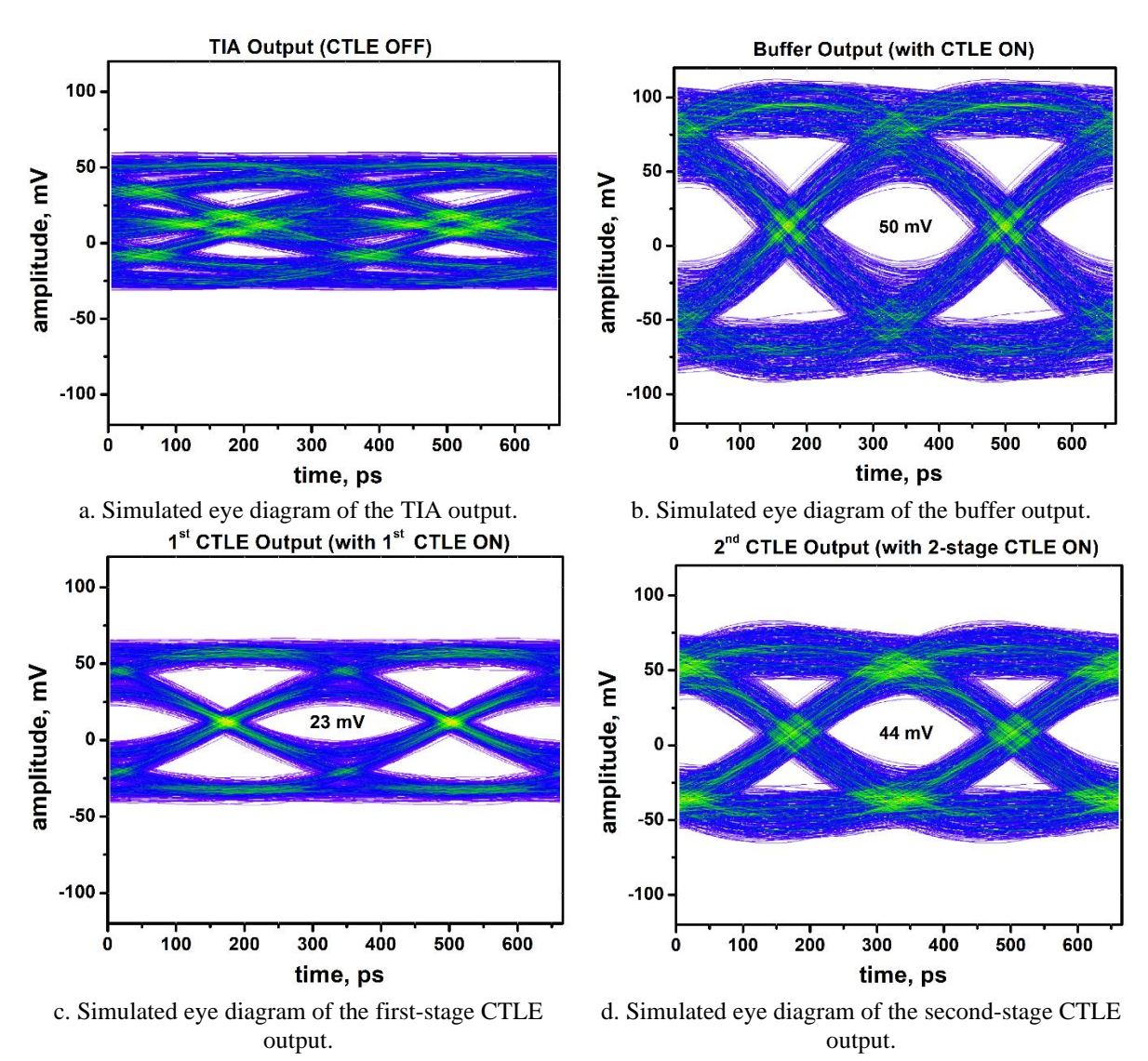
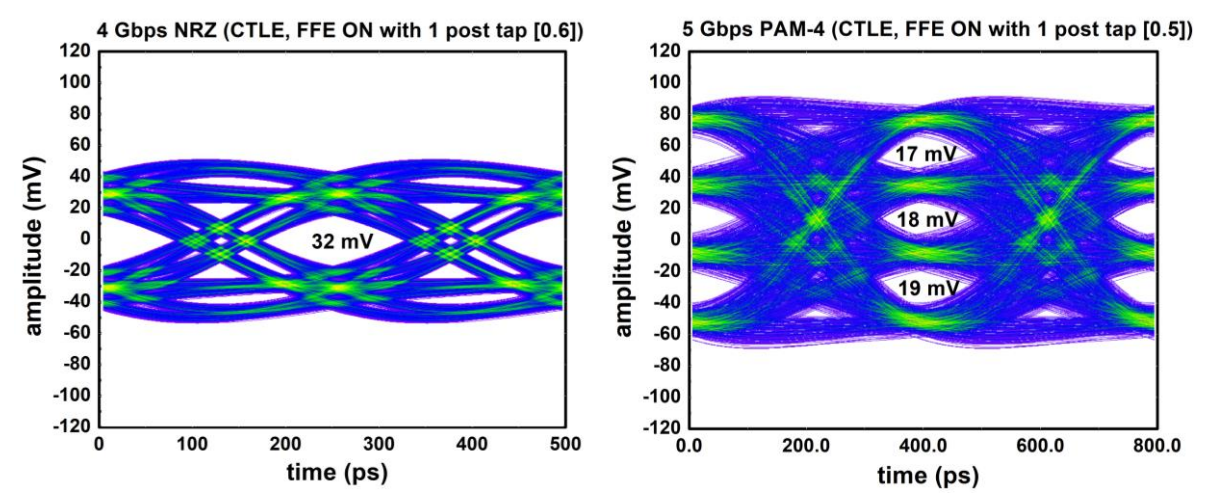


Fig. 57 Simulated eye diagram of the VLC transceiver with/without CTLE at 3 Gb/s data rate & 1.5 m distance.

At a distance of 1.5 m with the SNR of 29 dB, 5 Gb/s data rate is achieved through PAM-4 modulation schemes with FFE, and 4 Gb/s data rate is achieved through NRZ modulation schemes with FFE. The eye diagrams are shown in Fig. 58 with FFE settings. It should be noted here that the FFE developed in Matlab is a 1-post tap and $\frac{1}{2}$ -UI spaced equalization based on practical considerations. The tap weights for compensation of NRZ and PAM-4 signals are 0.6 and 0.5 respectively.



a. Simulated NRZ eye diagram of the buffer output.
 b. Simulated PAM-4 eye diagram of the buffer output.
 Fig. 58 Simulated NRZ & PAM-4 eye diagram of the VLC transceiver with FFE at a distance of 1.5 m.

4.2 System Simulation Results

Firstly, the ambient light rejection (ALR) and DC offset cancellation (DOC) of the proposed design are simulated. The AC simulation results, shown in Fig. 60, illustrate that the ALR provides 30 dB cancellation of DC gain. With the DOC feedback loop, an additional 45 dB reduction of DC gain is attained.

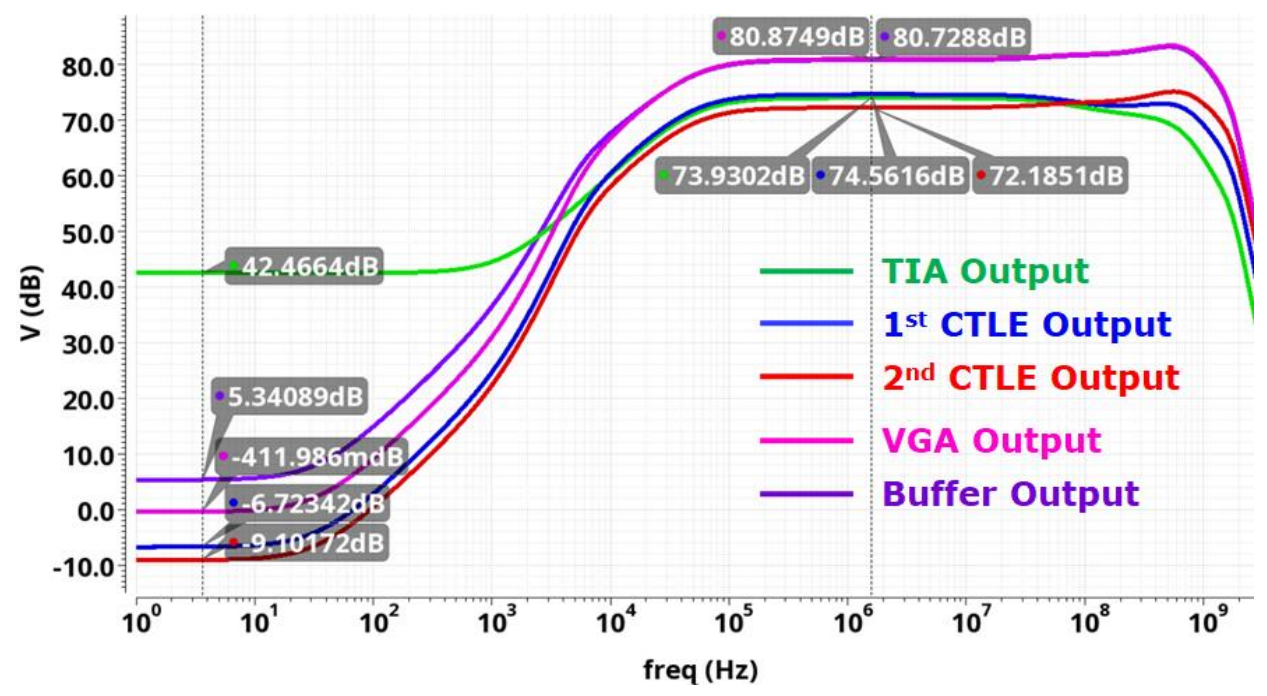


Fig. 59 AC simulation results of the whole transceiver.

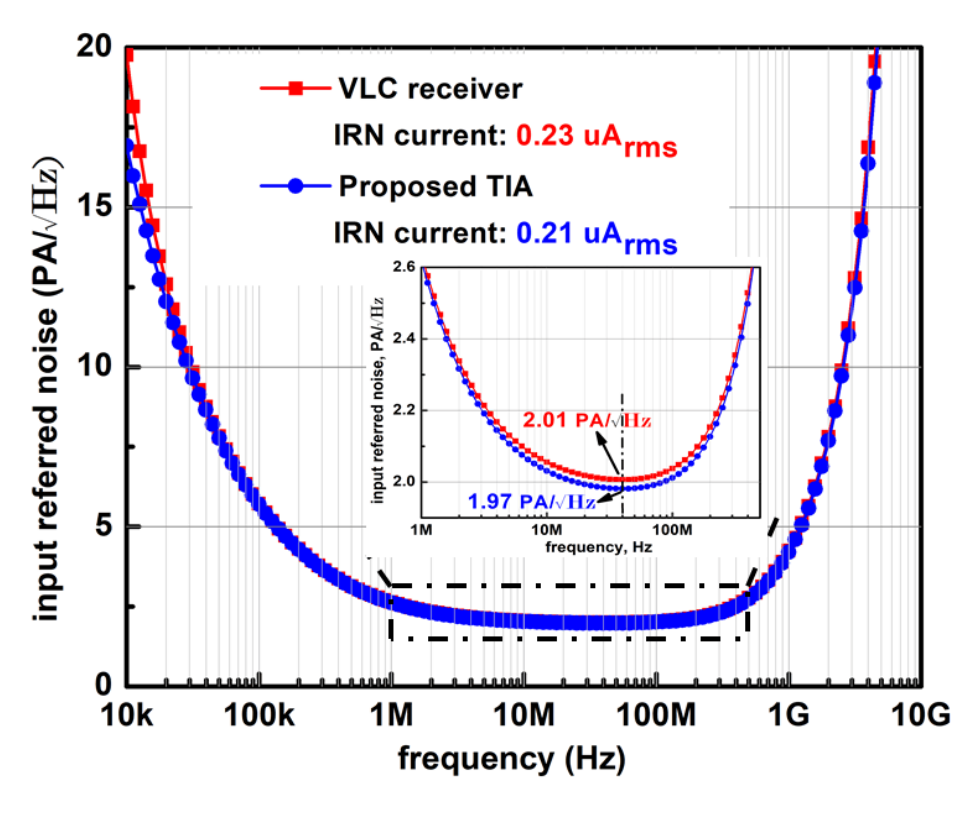
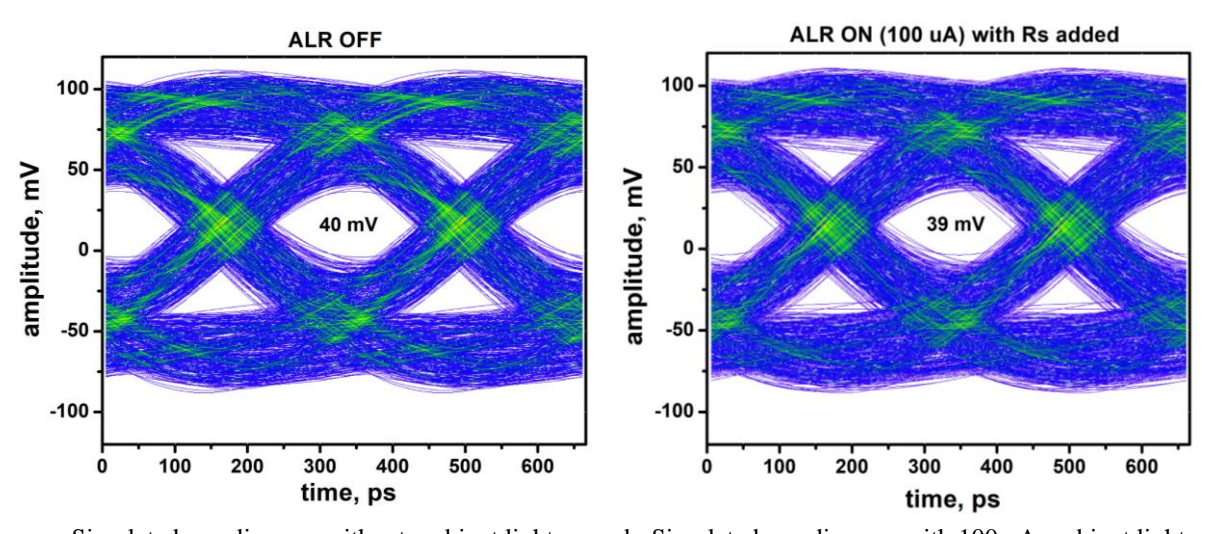
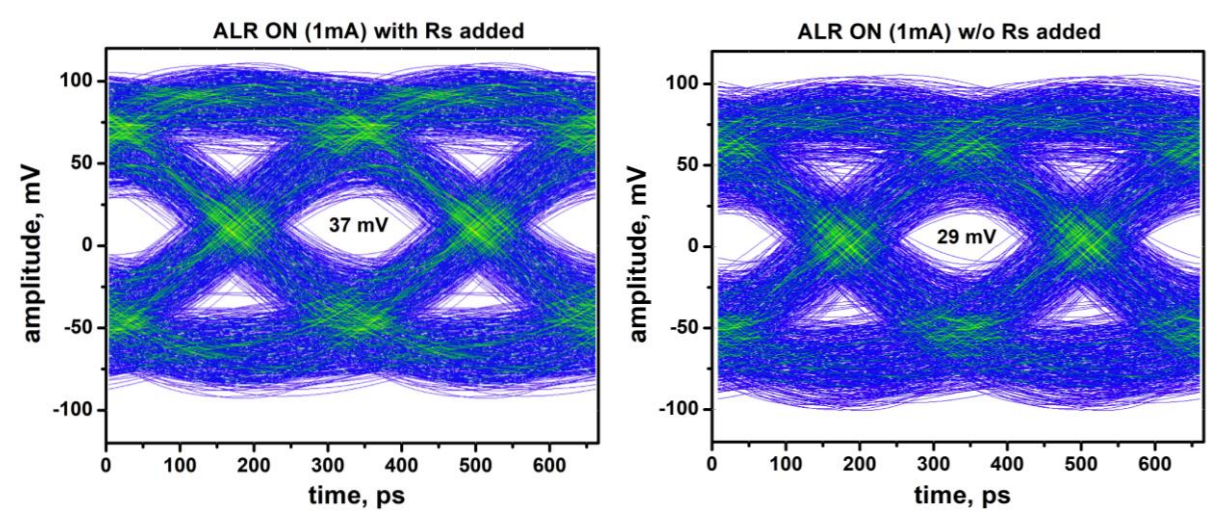


Fig. 60 IRN current power spectral density of the VLC receiver.

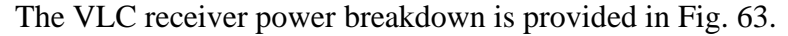
Secondly, the transient simulation with and without ambient light is conducted, and results are provided in Fig. 61 and Fig. 62 with noise on. The function of the R_s for noise reduction with heavy ambient photocurrent DC of 1 mA is shown in Fig. 62. In the transient eye diagram, a vertical eye height of 8 mV is achieved through the added R_s .



a. Simulated eye diagram without ambient light.
 b. Simulated eye diagram with 100 uA ambient light.
 Fig. 61 Simulated eye diagram of the VLC transceiver with/without ambient light at 3
 Gb/s data rate & 1.5 m distance.



a. Simulated eye diagram with R_s added in ALR.
 b. Simulated eye diagram without R_s added in ALR.
 Fig. 62 Simulated eye diagram of the VLC transceiver with/without R_s added in ALR at 3 Gb/s data rate & 1.5 m distance.



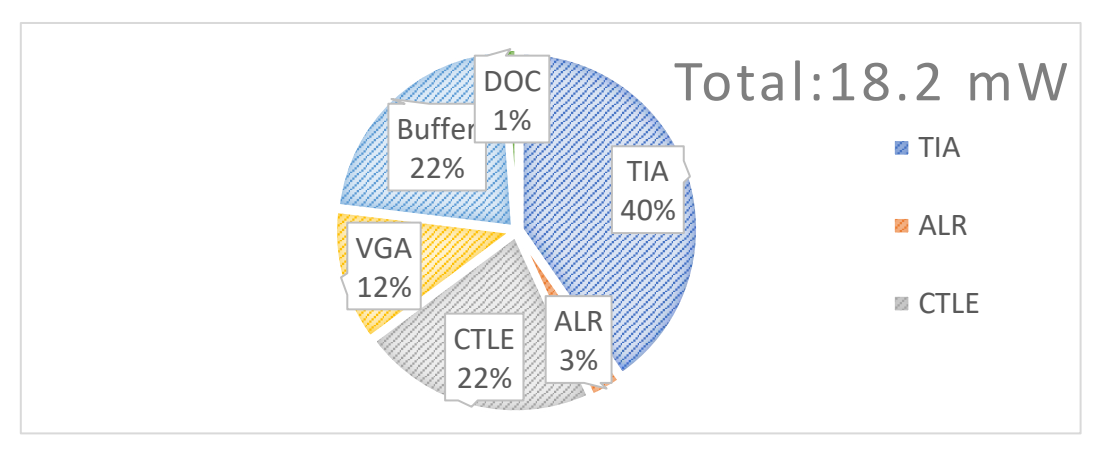


Fig. 63 VLC receiver power breakdown.

4.3 System Evaluation Results with ISEE

The modulated baseband signal of PAM, PAM with FFE, and DCO-OFDM with bit and energy allocation (BEA) generated in Matlab is imported into the VLC transceiver designed. The transient signal from the buffer output is attained after co-simulation in Cadence. Through demodulation and analysis of the ISEE, the system performance measures of the VLC transceiver, such as BER, distance, and data rate, are generated. Systems with the different modulation schemes are compared, and the results are presented as follows.

The SNR versus communication distance of the VLC link is calculated in Matlab and the fitting curve with IRN current of 0.23 uA_{rms} for the proposed receiver with a scaled dummy side and 0.27 uA_{rms} for the proposed receiver with a replica dummy side are shown in Fig. 64.

The ISEE discussed in chapter 2 with modulation schemes of NRZ, NRZ with FFE, PAM-4, PAM-4 with FFE, and DCO-OFDM with BEA is utilized for system evaluation. The SNR for distance modulation is added to the exported signal in Matlab. Then the data rate and BER are calculated. The maximum data rate attained with BER lower than FEC upper limit 3.8E-3 versus distance is as in Fig. 65. The dynamic range of the VLC signal is 1.5 uA_{pp} to 22 uA_{pp} at the receiving input of TIA. And the corresponding communication range in the proposed design can reach 0.75 m ~ 3 m with a data rate of over 2.5 Gb/s.

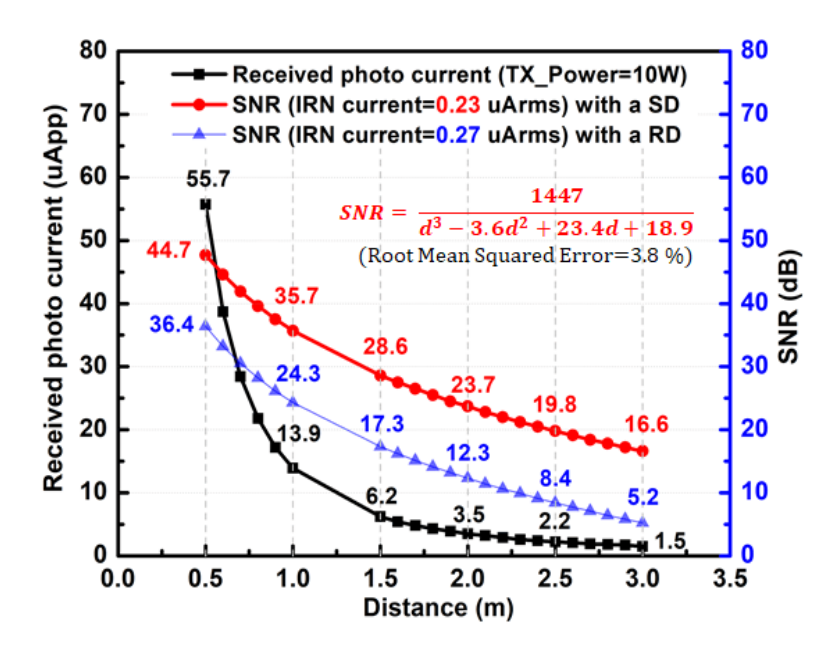


Fig. 64 SNR versus distance fitting curve of line-of-sight channel model.

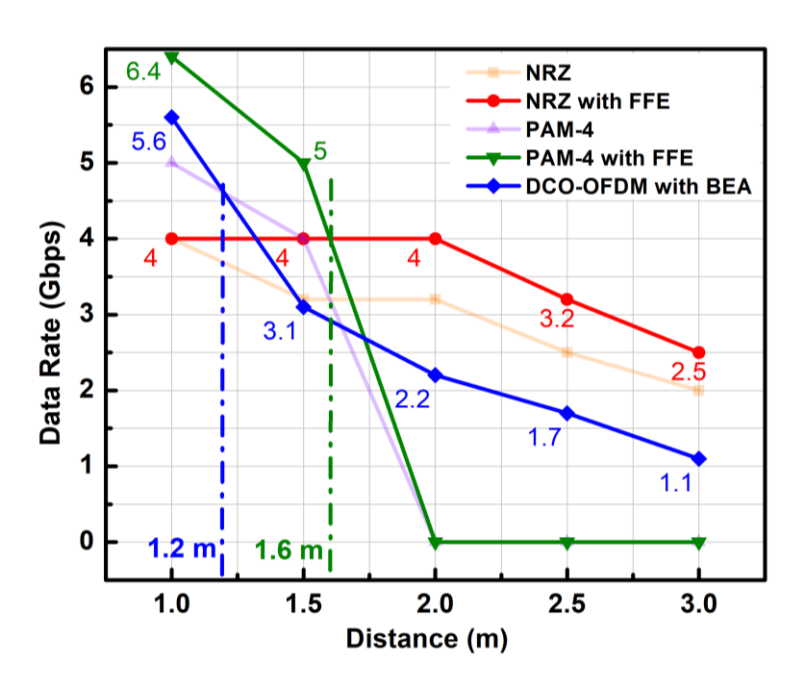


Fig. 65 Simulated maximum data rate versus communication distances with a lens used before the photodiode.

The DCO-OFDM with BEA modulation schemes with a modulation bandwidth of 1.45 GHz achieves a 3.1 Gb/s data rate at an SNR of 29 dB. But it exceeds the other modulation schemes except PAM-4 with FFE when the SNR is larger than 32.5 dB. The PAM-4 with FFE modulation scheme is verified to attain the maximum bit efficiency with an SNR greater than 27.5 dB. However, it requires an additional 9.5dB SNR compared to the NRZ modulation scheme, which limits the applicable communication range. NRZ with FFE modulation scheme is verified to be the best choice for movable VLC applications or long-distance VLC. At a distance of 1.5 m, BER versus data rate with the IRN current of 0.23 uA_{rms} for the proposed receiver with a scaled dummy side and 0.27 uA_{rms} for the proposed receiver with a replica dummy side are shown in Fig. 66. The SNR is calculated as 28.6 dB and 17.3 dB respectively. It shows that when the SNR is 17.3 dB, only NRZ modulation is supported, and a 3 Gb/s data rate is achieved with FFE for the receiver with a replica dummy side. A maximum data rate of 5 Gb/s is achieved through PAM-4 with FFE modulation for the receiver with a scaled dummy side. It means that the proposed design with an IRN current reduction of 0.04 uA_{rms} can bring 1.67x bit efficiency. Besides, when the target data rate is lower than 3.6 Gb/s at a distance of 1.5 m, NRZ is verified as a better choice for a lower BER.

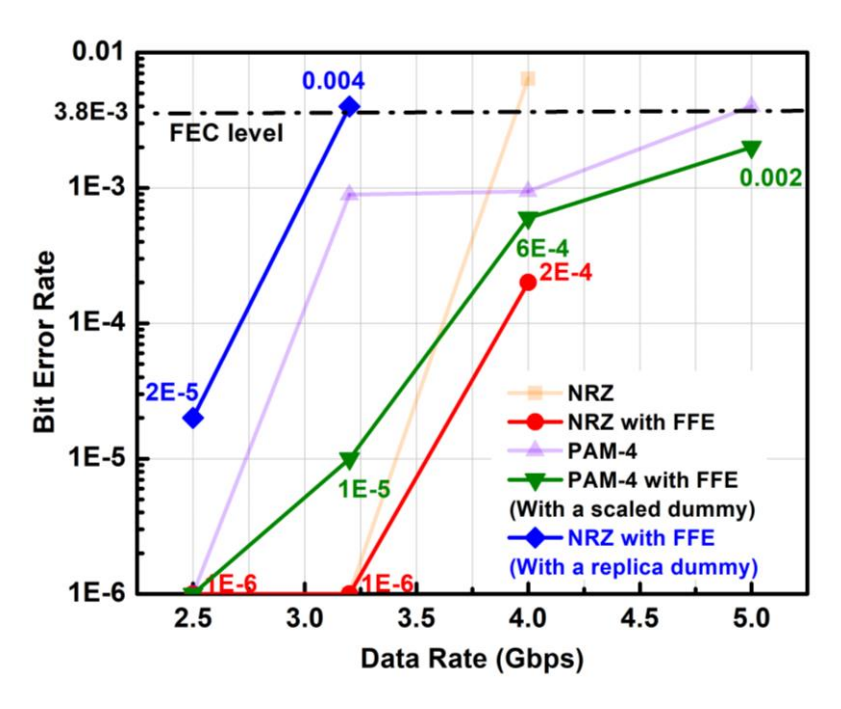


Fig. 66 Simulated BER versus data rate at a fixed distance of 1.5 meters with a lens used before the photodiode.

It must be clarified that the resolution for data rate simulation is limited because the data exported from the cadence must have finite decimals. The ISEE [19] developed is open source and provides a joint optimization of baseband and front-end circuits for system performance.

4.4 VLC Transceiver Performance Comparison

Since the VLC transceiver performance is greatly determined by the optoelectronic devices used in the channel, the figure of merit (FoM) includes not only the performance values like distance, data rate, and BER, but also the parameters of the lighting source, the optical lens, and the receiving PD. The equation is shown as Eq. 4.3 [10]:

$$FoM = \frac{Data_Rate[Mb/s] \times Log(BER)}{RX_pw_con[W] \times \frac{TX_pwr[lm] \times cos(0.5 \times TX_angle)}{Distance^2[m^2]} \times T/RX_lens_area[cm^2]}. (4.3)$$

where RX_pw_con represents the receiver power consumption, and TX_pwr represents the luminous flux of the LEDs, and TX_angle represents the half power angle of the LED, which is one of the important parameters of the LED, and T/RX_lens_area is the product of the lens areas of the lens used at transmitter and receiver.

With the system performance evaluation results attained from the ISEE, the performance summary and comparison of the designed VLC transceiver is shown in Table 4.1.

Table 4.1. VLC transceiver performance comparison.

	[10]	[22]	[26]	This work
Technology	0.18 um	Discrete	Discrete	45 nm
Transmitter Source	White LED	Micro-LED	Micro-LED	Micro-LED
Transmitter Half Power Angle	120°	60°	60°	60°
Transmitter Power (W)	1	1	0.0045	10
Luminous Efficacy (lm/W)	107	60 (estimated)	60 (estimated)	60
T/RX Lens Area (cm ²)	20.3	10 (estimated)	8 (estimated)	12.56
Modulation Scheme	OOK	PAM4	DCO-OFDM	NRZ/ PAM4 / DCO-OFDM
Data Rate (b/s) @BER & Distance (m)	24M@1E-9 & 1.6m	1.6G@1E-12 & 0.6m	5.3G@3E-3 & 0.05m	5G@2E-3 & 1.5m
Equalization	CTLE	2-tap FFE	BEA	1-tap FFE+CTLE
RX Power Consumption (mW)	2.2	900 (datasheet)	7500 (Commercial)	18.2
-3dB Bandwidth (MHz) @C _{PD}	20 @10pF	650 @2.8pF	1000 @/	1450 @1.8pF
FoM	231	14.8	2.4	256

CHAPTER 5. CONCLUSION AND FUTURE WORK

5.1 Conclusion

A cross-domain integrated system evaluation engine (ISEE) based on Matlab, ADS, and Cadence is introduced. The visible light communication (VLC) link model and baseband design including pulse amplitude modulation (PAM) with feed-forward equalization (FFE) for bandwidth compensation and direct-current offset orthogonal frequency division multiplexing (DCO-OFDM) with bit-and-energy allocation (BEA) for maximum bit efficiency are developed in the ISEE for communication system evaluation and comparison of different modulation schemes.

In addition, a low noise cascode trans-impedance amplifier (TIA) with cross-coupled pairs for bandwidth improvement and a scaled dummy side for noise, power, and area reduction is proposed. A VLC transceiver with the receiver designed in a 40 nm CMOS process is presented. A pre- passive LC equalizer and a FFE at the transmitter side and post- two-stage continuous time linear equalizer (CTLE) at the receiver side are employed for bandwidth compensation.

Finally, the joint optimization of the baseband and front-end design for the VLC transceiver is achieved by using ISEE. Then the system performance metrics like data rate, distance, and bit error rate (BER), are evaluated through the ISEE. Simulation results are concluded for system comparison of the VLC transceiver versus the signal-to-noise ratio with modulation schemes of NRZ with FFE, PAM-4 with FFE, and DCO-OFDM with BEA.

Assuming that the transmitter power is 10 W and the communication distance is 1.5 m, the maximum data rate of 4 Gb/s with BER over 3.8E-3 of FEC level is achieved through NRZ with FFE, the maximum data rate of 5 Gb/s is achieved through PAM-4 with FFE, and the maximum data rate of 3.1 Gb/s is achieved through DCO-OFDM with BEA. The maximum data rate of 5 Gb/s is realized using the receiver with a scaled dummy side, while the maximum data rate is 3 Gb/s for the receiver with a replica dummy side. The evaluation results of the transceiver show that the IRN current attenuation of 0.04 u A_{rms} brought by the scaled dummy side brings a 1.67x bit efficiency..

5.2 Future Work

Higher-order modulation schemes are more sensitive to the equalizer. Thus, future work should focus on the cooperation of the FFE and multiple peaking CTLE for wide bandwidth compensation regarding the stabilities, and automatic adaption methods could be proposed.

Other state-of-the-art modulation schemes investigated for improving bit efficiency could also be added to the ISEE for comparison of VLC system performance. In addition to the evaluation of the system, the power consumption estimation and difficulties of the circuit design, especially the baseband design, should be considered for realistic comparisons of system customization.

Finally, the integration level of the VLC transceiver is needed to reduce manufacturing costs and increase energy efficiency to further develop VLC technology.

5.3 List of Publications

- [1] <u>T. Min</u>, J. Abdekhoda, and C. P. Yue, "A Low Noise Cascode Trans-Impedance Amplifier for High-Speed Visible Light Communication", *IEEE Trans. Circuits Syst. II, Express Brief.* (Under Review)
- [2] <u>T. Min</u>, J. Kang, B. Xu, W. Shi, and C. P. Yue, "Design and Verification of a 334-Mb/s DCO-OFDM Li-Fi Transceiver Using Integrated System Evaluation Engine," 2021 IEEE 14th International Conference on ASIC (ASICON 2021).
- [3] F. Chen, C, Zhang, <u>T. Min</u>, B. Xu, Q. Pan, and C. P. Yue, "Design and Co-Simulation of QPSK and NRZ/PAM-4/PAM-8 VCSEL-Based Optical Links Utilizing an Integrated System Evaluation Engine," 2021 IEEE 14th International Conference on ASIC (ASICON 2021).
- [4] B. Xu, B. Hussain, X. Liu, <u>T. Min</u>, H. Cheng, and C. P. Yue, "Smart-Home Control System Using VLC-Enabled High-Power LED Lightbulb," 2021 IEEE 10th Global Conference on Consumer Electronics (GCCE 2021).
- [5] B. Xu, <u>T. Min</u>, and C. P. Yue, "Design of PAM-8 VLC Transceiver System Employing Neural Network-based FFE and Post-Equalization", *IEEE Photonics Journal*. (Under Review)

REFERENCES

- [1] S. Naser *et al.*, "Optical rate-splitting multiple access for visible light communications," *arXiv Preprint arXiv:2002.07583*, 2020.
- [2] M. Abualhoul, Visible Light and Radio Communication for Cooperative Autonomous Driving: Applied to Vehicle Convoy, 2016.
- [3] M. T. Rahman, A. S. M. Bakibillah, R. Parthiban, and M. Bakaul, "Review of advanced techniques for multi-gigabit visible light communication," *IET Optoelectronics*, vol. 14, no. 6, pp. 359-373, 2020.
- [4] [Online] Available: https://www.statista.com/statistics/753939/global-led-luminaire-market-size/
- [5] M. Kashef, *et al.*, "Energy efficient resource allocation for mixed RF/VLC heterogeneous wireless networks," *IEEE Journal on Selected Areas in Communications*, vol. 34, no. 4, pp. 883-893, Apr. 2016.
- [6] Dushyantha A. Basnayaka, H. Haas, "Design and analysis of a hybrid radio frequency and visible light communication system," *IEEE Transactions on Communications*, no. 99, pp. 1-1, 2017.
- [7] X. Li *et al.*, "Cooperative load balancing in hybrid visible light communications and WiFi," *IEEE Transactions on Communications*, vol. 63, no. 4, pp. 1319-1329, Apr. 2015.
- [8] Y. Wang and H. Haas, "Dynamic load balancing with handover in hybrid Li-Fi and 7 Wi-Fi networks," *IEEE Journal of Lightwave Technology*, vol. 33, no. 22, pp. 4671-4682, Nov. 2015.
- [9] Y. Gao *et al.*, "22.8 An AC-input inductorless LED driver for visible-light-communication applications with 8Mb/s data-rate and 6.4% low-frequency flicker," *2017 IEEE International Solid-State Circuits Conference (ISSCC)*, pp. 384-385.
- [10] X. Li, B. Hussain, L. Wang, J. Jiang and C. P. Yue, "Design of a 2.2-mW 24-Mb/s CMOS VLC receiver SoC with ambient light rejection and post-equalization for Li-Fi applications," *IEEE Journal of Lightwave Technology*, vol. 36, pp. 2366-2375, June 2018.
- [11] Y. Huang *et al.*, "Influence of current density and capacitance on the bandwidth of VLC LED," *IEEE Photonics Technology Letters*, vol. 30, no. 9, pp. 773-776, May 2018.
- [12] T. Min *et al.*, "Design and verification of a 334-Mb/s DCO-OFDM Li-Fi transceiver using integrated system evaluation engine," in *IEEE 14th International Conference on ASIC (ASICON)*, Oct. 2021.

- [13] [Online] Available: https://github.com/OWL-Integrated-System-Evaluati on-Engine.
- [14] W. Shi *et al.*, "An integrated system evaluation engine for cross-domain simulation and design optimization of high-speed 5G millimeter-wave wireless SoCs," in *IEEE 14th International Conference on ASIC (ASICON)*, Oct. 2021.
- [15] F. Chen *et al.*, "Design and co-simulation of QPSK and NRZ/PAM-4/PAM-8 VCSEL-based optical links utilizing an integrated system evaluation engine," in *IEEE 14th International Conference on ASIC (ASICON)*, Oct. 2021.
- [16] B. Hussain *et al.*, "Visible light communication system design and link budget analysis," *IEEE Journal of Lightwave Technology*, vol. 33, pp. 5201-5209, Dec. 2015.
- [17] Z. Wang, Q. Wang, W. Huang, and Z. Xu, *Visible Light Communications: Modulation and Signal Processing*. John Wiley & Sons, 2017.
- [18] A H. Azhar *et al.*, "Experimental comparisons of optical OFDM approaches in visible light communications", *IEEE Globecom Workshop*, 2013, pp 1076–80
- [19] N. Fujimoto and H. Mochizuki, "614 Mbit/s OOK-based transmission by the duobinary technique using a single commercially available visible LED for high-speed visible light communications," in 2012 38th European Conference and Exhibition on Optical Communications, 2012: IEEE, pp. 1-3.
- [20] C. Lee *et al.*, "4 Gbps direct modulation of 450 nm GaN laser for high-speed visible light communication," *Optics Express*, vol. 23, no. 12, pp. 16232-16237, 2015.
- [21] G. Stepniak, L. Maksymiuk, and J. Siuzdak, "1.1 GBIT/S white lighting LED-based visible light link with pulse amplitude modulation and Volterra DFE equalization," *Microwave and Optical Technology Letters*, vol. 57, no. 7, pp. 1620-1622, 2015.
- [22] X. Li *et al.*, "Wireless visible light Communications employing feed-forward pre equalization and PAM-4 modulation," *IEEE Journal of Lightwave Technology*, vol. 34, no. 8, pp. 2049-2055, Jan. 2016.
- [23] N. Chi, Y. Zhao, M. Shi, P. Zou, and X. Lu, "Gaussian kernel-aided deep neural network equalizer utilized in underwater PAM8 visible light communication system," *Optics Express*, vol. 26, no. 20, pp. 26700-26712, 2018.
- [24] G. Cossu, A. Wajahat, R. Corsini, and E. Ciaramella, "5.6 Gbit/s downlink and 1.5 Gbit/s uplink optical wireless transmission at indoor distances (≥ 1.5 m)," in 2014 The European Conference on Optical Communication (ECOC), 2014: IEEE, pp. 1-3.

- [25] R.X. Ferreira *et al.*, "High bandwidth GaN-based micro-LEDs for multi-Gb/s visible light communications", *IEEE Photonics Technol. Lett.*, 2016, 28, pp. 2023–2026.
- [26] D. Tsonev *et al.*, "A 3-Gb/s single-LED OFDM based wireless VLC link using a gallium nitride µLED", *IEEE Photonics Technol. Lett.*, 2014, 26, pp. 637–640.
- [27] B. L. Kasper, "Equalization of multimode optical fiber systems," *The Bell System Technical Journal*, vol. 61, no. 7, pp. 1367–1388, Sep. 1982.
- [28] N. Chi, LED-based Visible Light Communications, Springer, 2018.
- [29] R. A. Shafik, M. S. Rahman, and A. R. Islam, "On the extended relationships among EVM, BER and SNR as performance metrics" in *2006 International Conference on Electrical and Computer Engineering*.
- [30] R. F. Fischer and J. B. Huber, "A new loading algorithm for discrete multitone transmission" in 1996 IEEE Global Telecommunications Conference.
- [31] [Online] Available: http://hyperphysics.phy-astr.gsu.edu/hbase/phyopt/reflco.html.
- [32] J. G. Proakis and M. Salehi, *Digital Communications*, McGraw-Hill (Inc., New York). 1995.
- [33] Y. Zhou, J. Zhao, M. Zhang, J. Shi, and N. Chi, "2.32 Gbit/s phosphorescent white LED visible light communication aided by two-staged linear software equalizer," in 2016 10th International Symposium on Communication Systems, Networks and Digital Signal Processing (CSNDSP), 2016: IEEE, pp. 1-4.
- [34] J. Kosman *et al.*, "29.7 A 500Mb/s -46.1dBm CMOS SPAD receiver for laser diode visible-light communications," in 2019 IEEE International Solid- State Circuits Conference (ISSCC), 2019, pp. 468-470, ISSCC.2019.
- [35] T. Jukic, B. Steindl and H. Zimmermann, "400μm diameter APD OEIC in 0.35μm BiCMOS," *IEEE Photon. Tech. Lett.*, vol. 28, no. 18, pp. 2004-2007, Sept. 2016.
- [36] B. Fahs, et al., "A 12m 2.5Gb/s lighting compatible integrated receiver for OOK visible light communication," *Journal of Lightwave Tech.*, vol. 34, no. 16, pp. 3768-3775, Aug. 2016.
- [37] X. Li and C. P. Yue, "3 GHz, 1 mW inverter-based TIA with capacitive feedback for enhanced gain and sensitivity in VLC applications", *Electron. Lett.*, 2019.
- [38] G. A. Mostafa *et al.*, "A 12 Gb/s -16.8 dBm OMA sensitivity 23 mW optical receiver in 65 nm CMOS", *J. Solid-State Circuits*, 2018, 53, (2), pp. 445-457, doi: 10.1109/JSSC.2017.2757008

- [39] J. Wang *et al.*, "A fully-integrated 25 Gb/s low-noise TIA+CDR optical receiver designed in 40-nm CMOS", *Trans. Circuits Syst. II, Express Briefs*, 2019, 66, (10), pp. 1698-1702, doi: 10.1109/TCSII.2019.2925363
- [40] M. Enrico *et al.*, "Analysis and design of a power-scalable continuous-time FIR equalizer for 10 Gb/s to 25 Gb/s multi-mode fiber EDC in 28 nm LP CMOS", *J. Solid-State Circuits*, 49, (12), pp. 3130-3140.
- [41] Q. Pan, Y. Wang, Y. Lu, and C. P. Yue, "An 18 Gb/s fully integrated optical receiver with adaptive cascaded equalizer", *J. Sel. Top. Quant. Electron.*, 2016, 22, (6), pp. 361-369.
- [42] R. G. Smith and S. D. Personick, "Receiver design for optical fiber communication systems", *Semiconductor Devices for Optical Communication*, H. Kressel, Ed., 2nd ed. New York, NY, USA: Springer-Verlag, 1982.
- [43] F. Aznar, S. C. Pueyo, and B. C. Lopez, "Transimpedance Amplifier," in *CMOS Receiver Front-Ends for Gigabit Short-Range Optical Communications*. New York, NY, USA: Springer-Verlag, 2013, pp. 53–56.
- [44] J. E. Proesel *et al.*, "A 32 Gb/s, 4.7 pJ/bit optical link with –11.7 dBm sensitivity in 14 nm FinFET CMOS", *J. Solid-State Circuits*, 2017, 53, (4), pp. 1214-1226, doi: 10.1109/JSSC.2017.2778280